Two-Phase Bubble Flow Modelling for Restoration of Eutrophic Lakes

Azita Najafi Nejad Nasser

A Thesis

In

The Department

Of

Building, Civil, and Environmental Engineering

Presented in Partial Fulfillment of the Requirements

For the Degree of Doctor of Philosophy (Civil Engineering)

at Concordia University

Montreal, Quebec, Canada

July 2016

CONCORDIA UNIVERSITY
SCHOOL OF GRADUATE STUDIES

This is to certify that the thesis prepared

By: Azita Najafi Nejad Nasser

Entitled: Two-Phase Bubble Flow Modellinmg for Restoration of Eutrophic Lakes

and submitted in partial fulfillment of the requirements for the degree of
Doctor of Philosophy (Civil Engineering)

complies with the regulations of the University and meets the accepted standards with respect to originality and quality.

Signed by the final examining committee:

Dr. P. Valizadeh Chair

Dr. M. Mohammadian External Examiner

Dr. M. Paraschivoiu External to Program

Dr. Z. Chen Examiner

Dr. S. Rahaman Examiner

Dr. S. S. Li, Dr. C. N. Mulligan Thesis Supervisor

Approved by

Dr. F. Haghighat
Chair of Department or Graduate Program Director

Dr. A. Asif
Dean of Faculty of Engineering and Computer Science

ABSTRACT

Two-Phase Bubble Flow Modelling for Restoration of Eutrophic Lakes

AZITA NAJAFI NEJAD NASSER

Concordia University, 2016

For the remediation of eutrophic, anoxic lakes, this thesis considers artificial circulation as a technique by introducing air bubbles into the lake water, which has the advantage that no chemical substances will be added to the lake water. This study aims to improve the understanding of the hydrodynamic behaviour of water elements and air bubbles in a water body subject to aeration, and to investigate optimal aeration schemes for prevention of sedentary conditions and improvement of the anoxic conditions in eutrophic lakes.

A computational fluid dynamics (CFD) analysis of two-phase flow was performed using two different types of model domains: a cylindrical bubble column; and lakes. Predictions of the flow field are obtained from numerically solving the Reynolds-averaged continuity and momentum equations, using the Eulerian-Eulerian multiphase method. The CFD results are validated through a comparison of the predictions with available experimental measurements of the quantities made from a laboratory water tank.

Subsequently, the response of water and bubble motions to a selection of bubble size, air flow rate, and spatial configurations of injection was investigated. Using the results from these simulations, the beneficial effects of aeration on the enhancement of oxygen concentrations in the water column are analysed.

The results show that a proper solution for bubble columns is crucially dependent on the correct modelling of interphase forces and turbulence models. The consideration of the effect of interfacial forces has improved the results, especially at larger distances from the centreline of the model domain.

Oxygen is shown to transfer to water across bubble interfaces as the bubbles rise to the water surface. Oxygen transfer also occurs across the air-water interface at the free surface as a result of turbulence induced by bubble motions and water circulation.

Many independent variables have influence on the bubble flow field. The first set of variables was related to air injection, including bubble size, initial velocity, and air flow rate. The second set of variables is diffuser variables, including the number of ports, port diameter or diffusion area, spacing between adjacent ports, port angle with the horizontal, and elevation of ports above the bottom.

It has been demonstrated that a properly installed aeration system in a lake can possibly halt and eventually reverse anoxic condition. De-oxygenated bottom water is exchanged with highly oxygenated surface water. The opening of ports should be mounted at a certain height from the bottom. Specifically, the optimal height is shown to be 0.3 m for shallow lakes with a maximum depth of 2 m. Port spacing should be approximately equal to the maximum depth. This installation prevents re-suspension of bottom sediments while it creates full circulations around the injector. It reduces dead zones between two adjacent injectors and produces stronger downward flows. The installation induces the dispersion of air and increases oxygen transfer rate in water. The oxygen concentration is continuously increased with time and reaches a steady state. Thus, an aeration system can possibly halt and eventually reverse anoxic condition. This thesis has demonstrated

that computer modelling of aeration has the potential to improve our understanding of complex bubbly flow processes through systematic simulations.

Acknowledgements

First and foremost, I would like to express my immense appreciation and gratitude to my supervisors, Dr. Samuel Li and Dr. Catherine Mulligan for their support, understanding, and motivation. This work would not have been possible without their constant support and invaluable advice.

I wish to thank all my Ph.D committee members for their time; their useful comments and good advice during proposal session.

Finally and most importantly, I would like to thank my parents, without them I could not make it this far. I would also like to thank my dearest sister, and brother for their continuous inspiration and support.

Contents

List of Tables

List of Figures

List of Symbols

a	Interfacial area, (m^{-1})
A_{cs}	Cross-sectional tank area, (m^2)
C	Concentration of oxygen in the water column, (mg/L)
C_f	Concentration of oxygen in the water column at time $t = t_f$, (mg/L)
C^*	Concentration of the water in equilibrium with the bubble (mg/L)
C_s	Concentration of water exposed to the atmosphere (mg/L)
C_μ	k-ε turbulence model constant, (= 0.09, dimensionless)
C_D	Drag coefficient
C_l	Lift coefficient
C_{vm}	Virtual mass coefficient
C_{wl}	Wall lubrication coefficient
C_{wD}	Damping coefficient
C_{wc}	Cut-off coefficient
C_{td}	Turbulent dispersion coefficient
D	Diffusion coefficient of gas in water, (m^2/s)
D_s	Surface diameter of the lake, (m)
d_b	Diameter of air bubbles, (m)
d_p	Diameter of the circular pipe or inlet opening, (m)
D_j	Turbulent diffusivity in the x_j-direction, (m^2/s)
Δt	Time step, (s)
Δx	Grid spacing in the x_1-direction, (m)
Δy	Grid spacing in the x_2-direction, (m)

Eo'	Modified Eotvos number
Eo	Eotvos number
F_{awi}	The x_i-direction component of interfacial forces, (N)
f_d	Drag force, (N)
f_l	Lift force, (N)
f_v	Virtual mass force, (N)
f_w	Wall lubrication force, (N)
f_t	Turbulence dispersion force, (N)
g_i	Component of the gravity vector in the x_i-direction, (m/s^2)
G_w	Turbulent production due to viscous forces, ($kg.m/ s^3$)
H	Depth of the water in the lake (simulation), (m)
h_d	port elevation, (m)
h	Thickness of a layer of air, (m)
k	Turbulent kinetic energy, (m^2/s^2)
f_{pw}	Fraction of the particulate, (dimensionless)
G_ω	Production of ω, [$kg/(m^3.s^2)$]
k_d	The interphase momentum exchange coefficient (kg/m^3s)
K_L	Liquid-side mass transfer coefficient, (m/s)
K_La	Volumetric mass transfer coefficient, (s^{-1})
K_La_b	Volumetric mass transfer coefficient for oxygen at the bubble surface, (s^{-1})
$K_{Ls}a_s$	Volumetric mass transfer coefficient for oxygen at water surface, (s^{-1})
K_{LS}	Liquid film coefficient of the water exposed to the atmosphere, (m/s)
l	Turbulence length scale, (m)

L	Horizontal distance between two adjacent ports, (m)
N	Number of time step, (dimensionless)
N_p	Number of ports
$\vec{n}_w$	Unit normal pointing away from the wall
P	Phosphorus
p	Reynolds-averaged pressure, (Pa)
P_w	Turbulence production term, (kg.m/ s^3)
q	Air flow rate, (m^3/s)
S_{ji}	Mean flow strain-rate tensor, (s^{-1})
r	Radial distance from the centreline, (m)
R	Radius of the cylindrical tank, (m)
S	Magnitude of the strain rate, (1/s)
$S_{k,w}$	User-defined source term in Equation, (3.38)
$S_{\omega,w}$	User-defined source term in Equation, (3.39)
T	Time period of a numerical simulation, (s)
T_i	Initial time, (s)
t	Time, (s)
u^+	Dimensionless velocity
u_j	Component of the water velocity vector in the x_j-direction, (m/s)
u_{dr}	Drift velocity, (m/s)
$\vec{u}_{wa}$	Relative velocity, (m/s)
(u_1, u_2, u_3)	Components of the Reynolds-averaged water velocity, (m/s)
$(\tilde{u}_1, \tilde{u}_2, \tilde{u}_3)$	Components of the instantaneous water velocity, (m/s)

$\vec{u}_w$ Reynolds-averaged velocity vector for the liquid phase, (m/s)

(u_1', u_2', u_3') Fluctuating velocity component for the liquid phase, (m/s) (u_1', u_2', u_3')

v Component of the air velocity vector in the x_j-direction, (m/s)

v_o Entering velocity of air bubbles, (m/s)

v_s Superficial gas velocity (m/s)

$\vec{v}_a$ Reynolds-averaged velocity vector for the gas phase, (m/s)

V Volume of the lake, (m^3)

(x_1, x_2, x_3) Cartesian coordinates, (m)

y^+ Dimensionless wall distance

Y_k Dissipation for k, [$kg/(m.s^3)$]

Y_ω Dissipation for ω, [$kg/(m^3.s^2)$]

y_w Distance to the nearest wall, (m)

z Vertical distance from the bottom of the model domain, (m)

Acronyms

CFD Computational fluid dynamics

DO Dissolved oxygen

Fr Froude number

RANS Reynolds-averaged Navier-Stokes

RSM Reynolds shear stress model

Re Reynolds number

Sc Schmidt number

Sh Sherwood number

Sh_s Sherwood number for surface transfer

We Weber number

Subscripts

a Gas phase, referring to air bubbles

i Tensor index, referring to coordinate direction

j Tensor index, referring to coordinate direction

w Liquid phase, referring to lake water

Greek letters

α_a Volume fraction of air in a computational cell, (in percentage)

α_w Volume fraction of water in a computational cell, (in percentage)

δ_{ij} Kronecker delta ($\delta_{ij} = 1$, if $i = j$; $\delta_{ij} = 0$, if $i \neq j$)

ε Viscous dissipation rate of turbulent kinetic energy, (m^2/s^3)

T Water temperature (degree Celsius)

$\mu_{eff,w}$ Effective eddy viscosity ($N \cdot s/m^2$)

μ_{ta} Turbulence induced viscosity, ($N \cdot s/m^2$)

μ_{tw} Turbulent dynamic viscosity, ($N \cdot s/m^2$)

μ_w Molecular viscosity of water (liquid phase), ($N \cdot s/m^2$)

Π_{kw} Influence of dispersed phase on continuous phase in Equation (3.22), (m^2/s^2)

$\Pi_{\varepsilon w}$ Influence of dispersed phase on continuous phase in Equation (3.23), (m^2/s^3)

ρ_a Density of air, (kg/m^3)

ρ_w Density of water, (kg/m^3)

σ_k Turbulent Prandtl number for k, (dimensionless)

σ_ω Turbulent Prandtl number for ω, (dimensionless)

τ_p Particulate relaxation time, (s)

τ_w Wall shear stress, (N/m^2)

τ_w^* Dimensionless shear stress, (N/m^2)

τ_c Critical shear stress, (N/m^2)

τ_c^* Dimensionless critical shear stress

τ_{ji} Specific Reynolds shear stress, (N/m^2)

ω Specific dissipation rate, a parameter in the k-ω turbulence model, (s^{-1})

ω_k Angular velocity

σ Surface tension (N/m)

$\overline{\Omega}_{ij}$ Mean rate-of-rotation tensor

η Dimensionless strain rate coefficient

φ Port angel, (in degree)

δv_a Percentage errors for air velocity

δu_w Percentage errors for water velocity

$\delta \alpha_a$ Percentage errors for air volume fraction

1 Introduction

1.1 Background

Water is used in day to day activities such as drinking, bathing, washing, recreation, irrigation, and fishing, as well as for industrial purposes. Lakes are a critical source of water for domestic consumption, agriculture, fisheries, and industrial uses (Dodds et al., 2009) Ansari et al. (2011) suggested that water is the most valuable natural resources for the sustenance of life on the earth. The global demand for surface waters for many purposes is growing rapidly (Ryding and Rast, 1989). Any degradation in water quality, sedimentation, and loss of biodiversity is a major concern since it will affect water quality and water quantity (Ansari et al., 2011, p.1).

In Quebec, there are a large number of lakes. They are of importance as environmental, social and economic resources (Cloutier and Sanchez, 2007). According to Priskin (2008), eutrophication in Quebec lakes has been a water-quality problem. Possible causes are agricultural activities, human sewage, deforestation, industrial discharges, and urban run-off.

Eutrophication refers to a specific nutrient-enrichment scenario where an excess amount of natural or cultural (man-made) nutrients enters an aquatic ecosystem. Eutrophication causes a drastic increase in the production of algae, and dissolved oxygen (DO) depletion in bottom water. The algae blooms in the upper water column (or upper layer of water) and anoxic condition of lower water column (or lower layers of water) can cause significant degradation in water quality. This includes green colour, odour and taste (Environment Canada, 2004; Kim et al., 2010; Mukherjee, 2010; Schladow, 1993; Shaikh et al., 2013; Zic et. al., 1992). Eutrophication as a pollution problem was recognized in the mid-twentieth century in European and North American lakes. According

to field surveys (Ansari et al., 2011, p.146; Colin et al., 2007), 54% of the lakes in Asia, 53 % in Europe, 48% in North America, 41% in South America, and 28% in Africa, have shown eutrophication problems. As reported in Matsui (1995), the corporative studies of the International Lake Environment Committee Foundation (a *United Nations Environment Programme* commencing in 1986) collected environmental data from over 217 important lakes of world, and identified eutrophication as one of the six major environmental problems with negative impacts on water quality. The issue of eutrophication in lakes has attracted extensive attention from researchers (Ahlgren et al., 1988). They made efforts to develop strategies for controlling trophic state or lake productivity related to nutrient loading.

Shallow lakes tend to accumulate terrestrial organic matter and nutrients. Due to relative small volume, the loading of nutrients per unit volume can be high (Wetzel, 2001). Also, nutrients in shallow lakes can significantly increase due to sediment resuspension. This makes the eutrophication process more rapid and drastic (Schallenberg and Burns 2004).

With regard to nutrient loading, phosphorus is a key element in phytoplankton growth and dynamics. Phosphorus is the limiting nutrient in fresh water systems. Therefore, most remediation strategies have focused on the reduction of phosphorus load (Schauser and Chorus, 2007; Dai and Pan, 2014). Phosphorus is a chemical element with symbol P and atomic mass 30.97376. It is an essential nutrient of life. It is highly reactive, multivalent, non-metal of the nitrogen group and can never be found free in the nature (Canadian Council of Ministers of the Environment, 2004). In lakes and estuaries, phosphorus can be released into the overlying water under certain environmental conditions. Phosphorus is usually partitioned into three forms: (1) particular matter; (2) organic matter and sediment; and (3) dissolved fractions in aquatic system. Particulate phosphorus may enter runoffs primarily through riparian litter fall, soil erosion, and sediment

transport. They can exit in solution, as particles, loose fragments, or in bodies of aquatic organisms. Orthophosphate ions (PO_4^{3-}) is the most significant form of inorganic phosphorous required by aquatic plants and it's the only form of soluble inorganic phosphorus can utilized directly by aquatic biota (Environment Canada, 2004; Mulligan et al., 2010).

The main sources of phosphorous entering freshwater systems are (CCME 2005):

(1) Atmospheric input due to atmospheric activities such as precipitation, wind, weathering, and dust.
(2) Point sources, including sewage treatment plants and industrial effluents.
(3) Non-point sources or diffuse sources such as stormwater, and runoff due to agricultural and land cleaning activities.
(4) Non-point sources from within a water system, including washout from riverbanks and re-suspension from sediments (internal loading).

The loading rate of phosphorus depends on patterns of land use, geology, morphology of the drainage basin, human activities, pollution, soil productivity, on other factors. The response of an aquatic system with low productivity is a rapid increase in algal productivity as a result of the addition of phosphorus (Environment Canada, 2004).

Sediments are materials accumulated in water by deposition. Sediments consist of organic matter, mineral grains, rock fragments, carbonates and other precipitates including oxides of iron, magnesium, and aluminium. Wetzel (2001, p.251-253) stated that lake sediments contain much higher concentrations of phosphorus than in the water. The exchange equilibria under aerobic conditions are largely unidirectional toward the sediments while under anaerobic conditions, inorganic exchange at the sediment-water interface is strongly influenced by redox conditions.

Inorganic and organic particles are continuously stored in the bottom sediments in lakes. The retention capacity of the sediments is high. Due to biological (e.g. biological immobilization and mobilization), physiochemical (e.g. desorption and dissolution), and physical processes (e.g. diffusion), phosphorus can be released into water. This is known as internal loading (Madura and Goldyn, 2009; Pettersson, 1998). In the surficial sediments, the potential phosphorus source is very large in comparison to the water column. In other words, even a very small amount of phosphorus release would significantly affect the phosphorus concentration in water (Pettersson, 1998). Phosphorus release occurs in two forms: dissolved state or particulate state. Dissolved phosphorus is mainly phosphate. Through a chemical, physical or biological process, it can be mobilized and transported to the lake water. Particulate phosphorus can be transported to the water column either by the migration of resting stages of phytoplankton or by re-suspended sediment particles (Pettersson 1998). Researchers have reported occurrences of significant internal loading in lakes around the world, including Lake Taihu in China (Dai and Pan, 2014), Lake Okaro in New Zealand (Ozkundakci et al., 2014), Lake Simcoe in Ontario, Canada (Nurnberg et al., 2013), and Swarzdzkie Lake in Western Poland (Madura and Goldyn, 2009).

1.2 Consequences of eutrophication in lakes

Eutrophication in lakes has consequences as summarized below. An excessive amount of nutrients in lakes will cause undesirable over growth of phytoplankton and macrophytes. Excessive growth of aquatic plants and their subsequent death result in the formation of a thin greenish layer over the water body. This prevents light from penetrating deep in the lake and limits re-oxygenation of water through air circulation (Ansari et al., 2011, p.18). Dead algae would become food for bacteria, using oxygen to eat the dead algae. As a result, the dissolved oxygen level would drop, which can lead to fish kills (Ansari et al., 2011, p.18). There is scientific evidence that

eutrophication has caused hypoxia condition and fish kill in Lake Erie (Sondgrass, 1987) and Lake Peipsi in Russia (Kangur et al., 2013).

Eutrophication in lakes results in an increase in turbidity. In lakes that experience eutrophication, bottom sediments are visible at a depth of a few feet, while in water bodies with high clarity, this depth is 20 feet or more (Ansari et al., 2011). Turbidity is a water quality indicator. Another consequence of eutrophication is the enrichment stage (Gray, 1992). The sedimentation of these organic materials will change the benthic biomass since there would be more food available for benthic organisms as well as fish (Jorgensen et al., 1996). Eutrophication inevitably reduces the recreational value of lakes, causing an odour problem (Lee and Lee, 2005), and limiting activities such as swimming, boating and fishing.

Toxicity is another issue associated with eutrophication in lakes. Toxins produced by certain algal blooms especially blue green algae, are harmful to plants and animals. This can cause a reduction of biodiversity. Toxicity of these blooms would have an adverse impact on drinking water quality. A severe eutrophication problem due to algal blooms was observed in Missisquoi Bay located in southern Quebec. Swimming and other activities involving direct contact with water at public beaches of the bay were banned in summer 2001, 2002, 2003, and 2004 by the Regional Health and Social Services Board of Quebec (Potamis et al., 2004). Heavy eutrophication in two lakes, Lake Tegel and Lake Schlachtense in Berlin, Germany, caused massive blooms of cyanobacteria, which posed a threat to the recreational use of both lakes, and affected drinking water quality (taste, odour, and bacterial regrowth), as reported in Schauser and Chorus (2007). Unacceptable taste or odour problems caused by eutrophication were also reported in Ansari et al. (2011, p.225) and Ruhl (1994).

Potential damages caused by eutrophication are significant. Dodds et al. (2009) investigated economic damages due to human-induced eutrophication. Their investigation took into account the annual value losses in recreational water usage, waterfront property values, spending on recovery of threatened and endangered species recovery efforts, and spending on drinking water treatment. Their results showed that the approximate combined annual costs as a result of eutrophication in U.S. fresh waters has reached $2.2 billion. Therefore, eutrophication is costly.

1.3 Dissolved oxygen

Dissolved oxygen (DO) is oxygen gas molecules (O_2) present in water bodies. The dissolved oxygen concentration is an important index of water quality (CCME, 1999). It influences a number of biogeochemical processes that affect the well-being of organisms (Brown and Power, 2011; Moore et al., 2009). Therefore, DO depletion in water bodies has become one of the most serious environmental problems worldwide (Chen et al., 2007: Iriarte et al., 2014). Generally, the dissolved oxygen in a water body originates from the atmosphere through diffusion with surrounding air and also photosynthesis from aquatic plants (CCME, 1999; Moore et al., 2009). DO is consumed during respiration and other biogeochemical processes (Moore et al., 2009).

Levels of dissolved oxygen vary, depending on factors including atmospheric and hydrostatic pressure, turbulence, temperature, salinity, currents, upwellings, ice cover, and biological processes. The solubility of oxygen increases considerably in cold water (Wetzel, 2001, p.151-152).

Since the mid-twentieth century, eutrophication and global climate change have been the two major environmental changes that have adversely affected DO levels in aquatic ecosystems. An excess amount of nutrients would increase primary production. As a result, it increases organic

matter in the ecosystem. As organic production increases, it promotes microbial growth and respiration, which produces a greater demand for oxygen (Diaz and Rosenberg, 2008; Diaz, 2001; Iriarte et al., 2015). Low dissolved levels in the bottom water are created as planktonic algae die, which increases organic matter, fueling microbial respiration (Diaz and Rosenberg, 2008). If there is an excess of decaying organic material (from dying algae and other organisms) in a water body, the oxygen in the lower water column will be used up quickly. This organic material comes from dead algae and other organisms that sank to the bottom (Diaz and Rosenberg, 2008).

Deep, eutrophic water bodies can have low dissolved oxygen (DO) concentrations during thermally stratified and ice covered periods. Since there is no atmospheric contact, aeration or photosynthesis restore DO levels in the hypolimnion, the dissolved oxygen used in decomposition is not replaced (Prepas and Burke, 1997).

Hypoxia (DO levels below 2 mg l^{-1}) can result from natural eutrophication processes as well as cultural eutrophication. When oxygen consumption exceeds oxygen delivery to the bottom water, hypoxia will result (Richardson and Jorgensen, 1996). If hypoxia persists for years and organic matter and nutrients accumulate in the sediments, during which the hypoxic zone expands and the concentration of DO continues to fall, anoxia will be established (Diaz and Rosenberg, 2008).

In shallower waters, the bulk of oxygen loss that is attributable to oxidation occurs at the sediment–water interface, where bacterial activity and organic matter are concentrated. A considerable amount of oxygen is also lost in the water column by bacterial, plant, and animal respiration, particularly in deep lakes. Oxygen depletion also occurs by direct chemical oxidation of dissolved organic matter (CCME, 1999).

Excessive phosphorus loading in lakes and reservoirs increases the content of organic matter, which increases oxygen demand through decomposition (McGinnis et al., 2004). Decomposing organic matter can be a major sink for oxygen in aquatic ecosystems (Hamilton et al. 1997).

Thousands of natural, shallow lakes are formed in the midwestern region of Canada and the northern United States. For several months each winter, water is exposed to freezing air temperatures. Thus, ice and snow cover the lakes' surfaces (McCord et al., 2000; Ellis and Stefan, 1991). Ice blocks exchange oxygen with the atmosphere, and the water beneath cannot be mixed by the winds. In ice and snow covered lakes, light is insufficient for photosynthesis (Chin, 2006, p.212; Wetzel, 2001, p.156). In these lakes, oxygen comes mostly from photosynthesis of submerged aquatic plants. Thus, if photosynthesis is inhibited by low light intensities, oxygen is depleted by respiration and decay of organic materials (Fast, 1968). Due to oxygen depletion below the ice, winterkill (the death of fish) which is a significant fisheries management problem for shallow lakes, will occur (Ellis and Stefan, 1991; Fast, 1968).

A dissolved oxygen level that is too high or too low can harm aquatic life and affect water quality (Wetzel, 2001.). Even small changes in oxygen availability can give rise to physiological changes in the organisms found in the aquatic system. When oxygen consumption exceeds oxygen delivery to the bottom water, hypoxia will result. Hypoxia can result from natural eutrophication processes as well as cultural eutrophication. Hypoxia itself has been shown to be an endocrine disruptor, which can disrupt fish reproduction (Wu et al., 2003).

In summary, the two principal factors that lead to the development of hypoxia, sometimes leading to anoxia, are water column stratification, which isolates the bottom water from exchange with oxygen-rich surface water (Chen et al., 2007; Rabalais et al., 2001; Diaz, 2001), and decomposition

of organic matter in the bottom water, which reduces oxygen levels (Chen et al., 2007; Diaz, 2001; Wetzel, 2001, p. 164-165).

1.4 Objectives

The focus of this thesis is on the development of plausible techniques for the remediation of eutrophic lakes to prevent anoxic condition in the lake. The work will include numerical predictions of the response of eutrophic lake water quality to artificial aeration and a comparison of the predictions with experimental data. The work will also include application of the aeration as a remediation technique to Lake Caron (Figure 1.1), located at (74˚8'4.577"W, 45˚50'30.155"N), about 75 km north of downtown Montreal, Quebec.

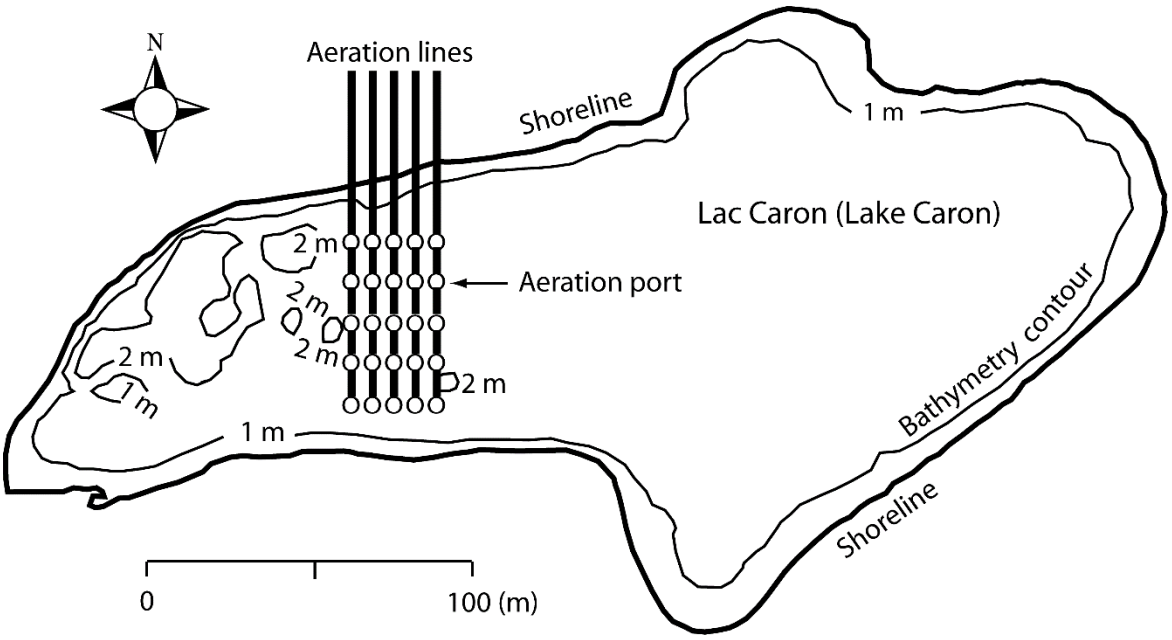

Figure 1.1 A map of Lac Caron (74°08'50"W, 45°50'28"N) in Saint-Anne-des-Lacs, Quebec, Canada. The thick lines show schematically a set of parallel aeration lines, laid along the lake bottom and close to each other. Each of them has one or multiple ports (the open circle markers) distributed along its length. Aeration operations can be such that all the ports simultaneously discharge air bubbles into the lake water.

This thesis considers lakes that have a free water surface exposed to the atmosphere that have eutrophication problems due to bottom sediments as a nutrient source. Submerged aeration systems will be to the lakes at their bottom. Relevant processes of aeration will be simulated as multi-phase flow using methods of computational fluid dynamics (CFD).

The objectives of this thesis are:

1) To investigate how the size of air bubbles d_b, air flow rate (air flow velocity v times the air inlet cross-sectional area A), bubble plume spacing (separation distance L between adjacent air inlets), and number of injectors affect water circulation and turbulent mixing in anoxic lakes.
2) To examine how aeration affects re-suspension of the bottom sediments to the water and attempt to prevent the re-suspension.
3) To investigate the beneficial effects of aeration on the improvement to anoxic conditions in eutrophic lakes. In connection with this objective, this thesis will consider the case where the lake water is under anoxic condition.
4) To determine the optimum horizontal distance between two adjacent injectors and number of the ports, in order to obtain maximum fluid circulation and mixing in the lake.
5) To investigate the suitability of several turbulence closure models for computation of bubbly flow with various modes of motions (jet flow, eddy circulation) in a model lake subject to aeration.

1.5 Scope of the work

To achieve the objectives outlined above, this thesis is divided into six chapters.

Chapter 1 gives an introduction of the context and description of the problem as well as the objectives of the thesis.

Chapter 2 is a review of the literature pertinent to eutrophication in lakes, with an emphasis on outstanding issues related to various remediation techniques for the restoration of eutrophic lakes.

This review covers previous experimental work of bubble flows, field investigations of eutrophic lakes, and numerical modelling studies of water-quality problems due to eutrophication in natural water bodies. This chapter also summarizes previous studies on the oxygen mass transfer coefficient in the bubble column.

In Chapter 3, the modelling methodologies used in this study are described. The details of the numerical setup used in ANSYS Fluent, the governing equations and the numerical methodology are presented. This chapter provides the theoretical background and fundamental concepts of CFD modelling of dispersed bubble flow. The five turbulence closure models are explained in detail. The models include four two-equation eddy viscosity models (the standard k-ε model, the RNG k-ε model, the realizable k-ε model, and the SST k-ω model) and one stress-transport model (RSM). Also, a summary of interfacial forces with their equations are provided.

Chapter 4 is devoted to presentation of the numerical results for a cylindrical bubble column. The predictions of distributed water velocity, bubble velocity and air volume fraction are validated through a comparison of the predictions with available experimental measurements of the quantities made from a laboratory water tank (Anagbo and Brimacombe, 1990). Predictions of the flow field are obtained from numerically solving the Reynolds-averaged continuity and momentum equations, using the Eulerian multiphase method. The theoretical formulations are presented in Chapter 3. Turbulent motions are characterised using turbulent kinetic energy. Its

temporal and spatial variations are predicted using several two-equation turbulence closure models and a shear stress model. A systematic analysis has been carried out to reveal the independence of numerical results on mesh configurations used and the suitability of domain treatment, and also to compare the performance of the turbulence closure models. Moreover, calculation of the total change in DO concentration caused by injection of air bubbles to the water is provided.

Chapter 5, numerical simulations of two-phase bubbly flow in a model lake are carried out. A total of nine model runs were simulated using the Eulerian approach. These runs used the k-ε model for turbulence closure. The optimal height for the opening of aerators has been determined through a sensitivity test. The spacing between adjacent air inlets is also investigated. The variation of the oxygen concentration with time is calculated.

Finally, Chapter 6 provides conclusions and summaries, which are followed by the recommendations for future work. For easier tracking, the thesis layout is given below (Figure 1.2).

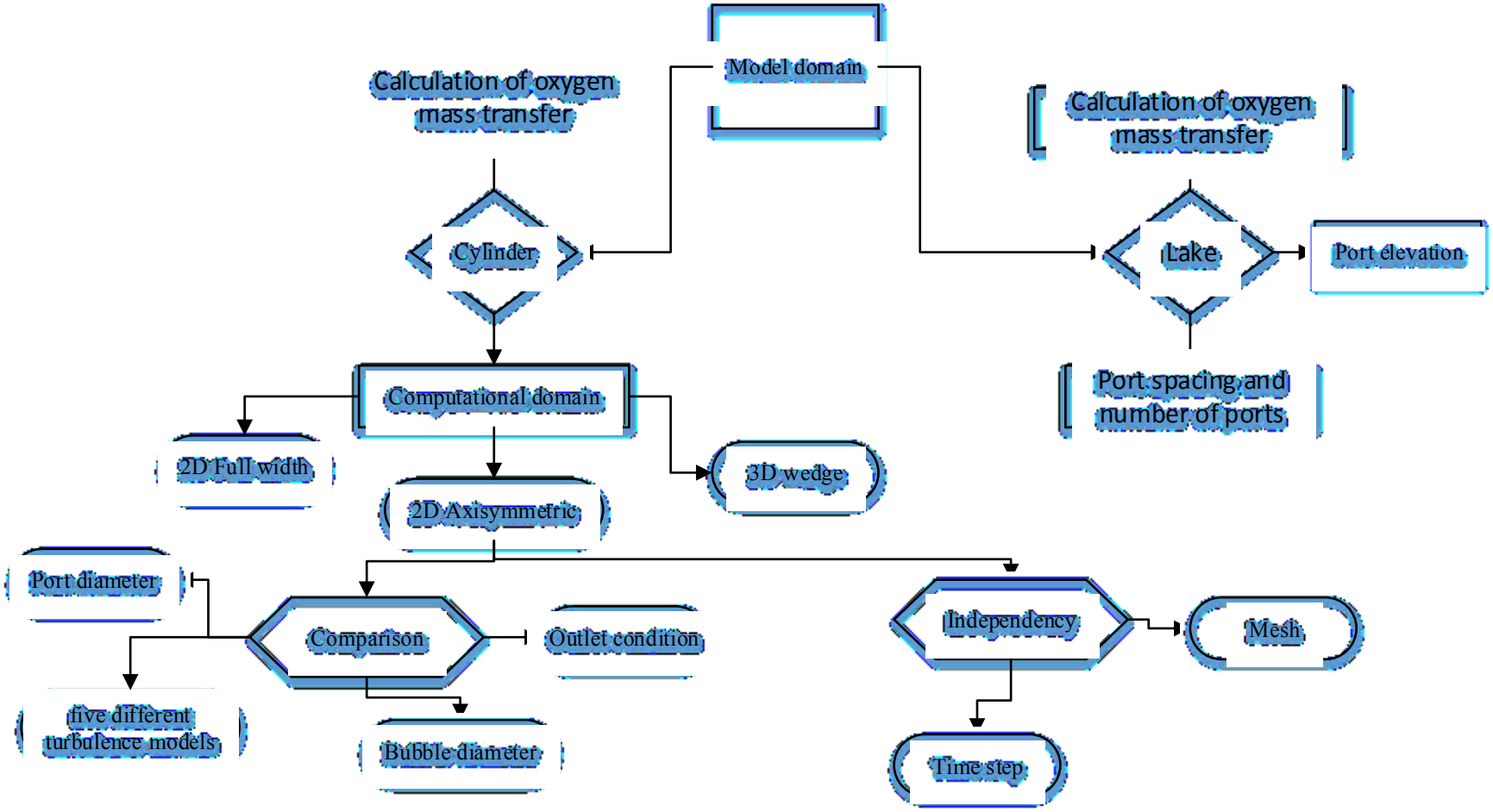

Figure 1.2 Summary of thesis layout.

1.6 Main contributions from this thesis

- An extensive examination on the hydrodynamics of bubble column and identification of the optimal conditions of aeration operations for a given eutrophic lake.
- Detailed investigation on the impact of computational domain on bubble behaviour and different hydrodynamic characteristics of bubble column cylinder.
- The development of prediction techniques for the following quantities: (1) the mass transport between the liquid phase (water) and the gas phase (air/oxygen); (2) variation in the concentration of dissolved oxygen with time
- An extension of experimental and field results, which are difficult and expensive to obtain.
- An exploration of the influence of port elevation on the re-suspension of the bottom sediments. This would leads to measures for preventing re-suspension of the bottom sediments.
- An extensive examination of the optimal port spacing and optimal number of ports required in a lake to obtain maximum fluid circulations and mixing.

2 Review of the Literature

2.1 Water quality

In order to improve the water quality, many countries have tried to reduce the external point and non-point sources of nutrients loading to lakes. For example, they made improvements in wastewater treatment to reduce phosphorus content of detergents and fertilizers and in increasing catchment retention capacity (Phillips et al., 1999; Van der Molen and Boers, 1999; Jensen et al., 2006). However, in the 1970s, limnologists (Qunhe et al., 2007; Marsden, 1989; Sondergaard et al., 2003) showed that internal loading from bottom sediment phosphorus could continue. This condition delayed the recovery of a eutrophic lake significantly even after controlling the external phosphorus loading (Reddy et al., 1999). Penn et al. (2000) estimated that under specific conditions, internal loading can contribute up to 80 % of total phosphorus in lakes. Sharpley (1994) reported that the magnitude of internal loading in Lake Ockeechobe in Florida was in the same order as external sources.

With regard to the external phosphorus load to a lake or reservoir, it is important to identify the major sources of phosphorous in the drainage basin as well as the way in which phosphorus enters the aquatic system (Ryding and Rast, 1989). Provided below is a brief summary of how to control external phosphorus load in an aquatic system. A direct reduction of phosphorus at the source is possible through three different ways: (1) phosphate inactivation during the sewage treatment process; (2) restriction of detergent phosphates; and (3) land use controls. One may consider treatment of tributary influent waters, canalization/diversion of wastewaters (or diverting effluents away from the water body and to municipal waste water treatment plant). Lake Washington is an example of water-quality improvement using diversion sewage (U.S. EPA, 1990).

2.2 In-lake remediation techniques

These techniques are used to treat in-lake symptoms of eutrophication. Although these methods might not be as effective as external nutrients control methods over the long term and might need to apply them repeatedly, they have some benefits. In situations where it is unfeasible to build a municipal wastewater plant or is too costly, these in-lake methods are effective. Also, when a primary control program is not sufficient to achieve a required goal, these methods would offer supplementary control measures (Ryding and Rast, 1989). Below is a brief description of some major in-lake control methods.

2.2.1 Chemical treatment

Chemical treatment of phosphorus is one of the in-lake techniques used in order to reduce internal loading in lakes after dealing with all the phosphorus loading from external sources. In this application, aluminium sulfate (alum), iron and calcium are used to bind phosphorus and preventing phosphorus diffusion from bottom sediments (Cooke et al., 1993; Welch et al., 1982, Klapper, 1991). These chemicals would immobilize the phosphorus (Ryding and Rast, 1989).

Based on Cooke et al.'s (1993) study, chemical treatment is done in two stages: Firstly, phosphorus is removed from the water column through precipitation by forming insoluble compounds that settle at the bottom of the lake. Secondly, further chemical reactions are conducted to inactivate the phosphorus in order to prevent its release from the sediment. Alum or hydrated aluminium sulphate is the most commonly used chemical treatment (Cooke et al., 2005; Reitzel et al., 2005). Welch and Cooke (1999) investigated the effectiveness and longevity of alum treatment in 21 lakes or lake basins across the United States. Welch et al. (1982) conducted a field study by collecting samples from four stations along Long Lake and analysed the samples in the lab according to

APHA (1975). Their goal was to find out if the alum floc remained well distributed in the lake during winter and decreased phosphorus release from sediments during summer. The mean depth of this shallow lake was 2 m.

In a field and laboratory study of Spring Lake located in western Michigan, Steinman and Ogdahl (2012) observed the change of macroinvertebrate community and internal phosphorus loading over time. Their objective was to explore the efficiency of alum treatment. They compared the results after five years of alum treatment with those before the treatment and with those after one year of alum treatment. The efficiency of the alum treatment declined slightly over the time period of five years. At the end of the treatment period, phosphorus remained in the lake sediments and there was a reduction of phosphorus in the water column, but the total phosphorus concentrations were still high. They considered alum treatment as a short term solution application.

Alum treatment has limitations. Sediment dwelling organisms can mix the floc layer with underlying sediment layers when the floc consists of a thin layer of insoluble aluminium hydroxide. Dissolved organic phosphorus can continue to cycle in the water column, since it cannot be removed effectively. Furthermore, the added chemicals have possible toxic effects on biota (Ryding and Rast, 1989).

2.2.2 Physical treatment – dredging

In this technique, nutrient-rich sediments are removed from the bottom of lakes. It requires knowledge of the sediment structure to ensure that an adequate depth of high-nutrient sediment is removed. This procedure has been used in many lakes. However, this technique is costly and disposal of sediments may contain toxic substances (Ryding and Rast, 1989). Not all the cases of using dredging to control internal nutrient cycling are successful. Failures or marginal successes

are for a variety of reasons: (1) an inaccurate pre-dredging assessment or an inadequate amount of sediment removed (Brashier et al., 1973; Ryding, 1982); (2) poor dredging techniques (Gibbons and Funk, 1983); and (3) a lack of proper watershed control measures (Garrison and Ihm, 1991). Besides, this method is expensive. Peterson (1981) reported costs in the range of $0.40 to $23.35 (in U.S. dollars) per cubic yard for 64 projects. The costs depended on site conditions, access, the nature of sludge and other factors. Serious negative impacts of dredging on the surrounding area and lakes are very high (U.S. EPA, 1990).

2.2.3 Physical treatment - hypolimnetic removal

Nutrient-enriched hypolimnetic waters can be removed through siphoning, pumping or selective discharge. This method is effective for improving hypolimnetic oxygen content, reducing surface phosphorus concentrations, and accelerating phosphorus export (Cooke et al., 2005, p.74). Several cases of using the hypolimnetic removal technique showed improvements in water quality. Researchers reported some successful cases of hypolimnetic withdrawal from lakes, including Mauensee in Switzerland (Gachter, 1976), two basins of Lake Wononscopomu in the U.S. (Kortmann et al., 1983), and Chain Lake in British Columbia, Canada (McDonald et al., 2004). However, this technique has some adverse effects. Nurnberg et al. (1987) emphasized that discharges of hypolimnetic contaminated water may cause a water quality problem downstream. If the outflow water is to be used for water supply, fishery or recreational activities, special precautions must be taken to minimize adverse effects. This technique incurs relatively low costs and low annual maintenance. Examples of costs for installing three systems in U.S. lakes (Cooke et al., 2005, p.173) are listed in Table 2.1.

Table 2.1 Costs for the installation of hypolimnetic removal systems (Cooke et al., 2005, p.173).

Lake	Area (ha)	Flow rate (m^3/min)	Costs (U.S. dollars)
Lake Waramuag	287	6.3	$62,000
Lake Ballinger	41	3.4	$42,000
Devil's Lake	151	9.1	$310,000

2.2.4 Hypolimnetic aeration

This technique is designed to increase oxygen content of hypolimnion without warming or de-stratifying the lake water and hence to reduce sediment phosphorus release at the sediment-water interface (Cooke et al., 2005, p.75). In Fast and Lorenzen (1976), 21 designs of hypolimnetic aeration were grouped into three categories: (1) mechanical agitation, which involves removal treatment and return of the hypolimnetic water; (2) injection of pure oxygen; and (3) injection of air. The costs of this technique depend on the amount of oxygen needed, distance from the compressor to the discharge site, and the depth of unit (Cooke et al., 2005, p.470). Cooke and Carlson (1989) demonstrated that this technique may not operate satisfactorily in shallow water bodies, if the maximum depth is less than 12 to 15 m or where hypolimnetic volume is quite small.

2.2.5 Biological control and other remediation methods

Biological control or bio-manipulation is a technique for controlling the growth of algae or other components of the food web. Specific organisms are used in the technique. For example, fish are used to control macrophytes, zooplankton are used to control phytoplankton, and manatee are used

to control water hyacinths (Cooke et al., 1986; Ryding and Rast, 1989). The bio-manipulation technique is reportedly effective only for an initial period of a few years. Five to ten years later, the technique appears to be ineffective. For example, for Round Lake in Minnesota, the results of biological control were satisfactory for the first two years. During the third year, the lake began to digress to its previous state (Width and Wright, 1984).

Using small polyvinyl pots, Ansari and Khan (2009) conducted experiments of the growth response of *Spirodela polyrrhiza* at different temperatures and pH levels as a measure of eutrophic water remediation. The main conclusion was that under controlled conditions (acidic pH and water temperature of 25° and 30°C), harvesting duckweed regularly was useful for removing high nutrient levels in eutrophic water.

2.3 Artificial circulation

2.3.1 Models of phosphorus loading

Empirical and theoretical models of phosphorus loading have been used by several researchers to study the restoration of eutrophication in lakes. Ahgren et al. (1988) discussed some aspects of modelling lake trophic state as a function of phosphorus loading. Suh et al. (2004) used a three-dimensional finite volume model (CE-QUAL-ICM) coupled with a finite element hydrodynamic model (TIDE3D) to simulate long term water quality of Lake Shiwhaho in Korea. They showed seasonal changes in water quality, and pointed out difficulties in meeting water quality standards without active circulation in the lake.

Water circulation in a lake can be generated by aeration. Air bubbles rise in the lake water at velocity as a function of distance from the lake bottom following their release. Levich (1962, p.

433-451) presented experimental results of rising velocity. These experimental results are useful for comparison with numerical predictions.

James and Pollman (2011) developed a model (ILPM) as an extension to earlier models for improvements in water quality of a shallow lake, Lake Okeechobee in Florida, United States. Some of the earlier models did not allow for the capacity of sediments to retain phosphorus. The other assumed the capacity to be constant and/or low. According to James and Pollman (2011), the internal flux of phosphorus was 2.6 times greater than the external input. As a result, the internal load caused inefficiency in load reduction for improvements in the lake water quality.

2.3.2 Aeration systems

Aeration (or artificial circulation) systems (Cook et al., 1993) have been used to prevent impacts of anoxic conditions and to reduce internal load of phosphorus. In order to stimulate circulation and mixing in liquid, submerged aeration systems were used (Kim et al., 2010, Demoyer et al., 2003). Their efficiency has been investigated by a number of researchers (Yum et al., 2005, Dixit et al., 2007, Hanson and Austin, 2012). Dixit et al. (2007) collected samples before, during and after the functioning of an aeration system on the bottom and surface layers of a lake. Their analyses indicated that artificial aeration was effective in improving water quality through a decrease in algae and an increase in dissolved oxygen levels in water, especially in the bottom layers. Hanson and Austin (2012) studied the effects of de-stratification on water quality and internal loading of phosphorus in an urban, temperate climate, eutrophic lake. They suggested that de-stratification by an aeration system was effective in lowering the lake total phosphorus mass. Gafsi and Kettab (2012) analysed the effects of hypolimnetic aeration and de-stratification on a eutrophic lake in Switzerland. Their system operated in de-stratification mode in the winter, using

big air bubbles, and in hypolimnetic aeration mode in the summer, using small bubbles of air/oxygen. Both techniques appear to result in re-oxygenation and de-phosphorization in the deep layer of the lake water, and thus improved water quality. Barbiero et al. (1996) observed negative impacts of artificial aeration on water quality of a lake. Gawronska et al. (2003) suggested that artificial aeration was effective in decreasing the internal loading rate. Tomasko et al. (2013) discussed the idea of pumping deeper water to the lake surface to create artificial circulation and reported a reduction in average phosphorus concentration, although there was no reduction in concentrations of nitrogen and chlorophyll-a. Thus, the responses of lakes to artificial aeration appear to be different. Some researchers observed an increase in the total algal biomass (Drury et al., 1975; Imteaz and Asaeda, 2000; Knoppert et al., 1970). Other researchers (Bernhardt, 1967; Imteaz and Asaeda, 2000; Malueg et al., 1971; Robinson et al., 1969) indicated a decrease in the total algal biomass.

2.3.3 Aeration using bubble plumes

Some researchers have conducted experimental and numerical studies of bubble plumes for improvements in water quality. These studies intended to identify relevant parameters (Demoyer et al., 2003; Imteaz and Asaeda, 1999; Kim et al., 2010; Rensen and Roig, 2001; Sato and Sato, 2001; Yum et al., 2008). Bubble plumes are produced when gases are injected in liquids. These systems occur in several engineering applications such as artificial aeration, oxygenation and mixing in tanks and water bodies, reservoir de-stratification (Lima Neto, 2012; Kim et al., 2010) analysed experimental data and proposed a model for predicting the effects of geometric parameters (bubble size and diffusing area) on de-stratification efficiency. They considered more field-based variables in their model than previous modelling researchers, providing guidelines for more advanced design and operation of an air diffuser. They emphasized the need for testing the

model under field conditions to facilitate practical application. They showed that de-stratification efficiency is proportional to the bubble diffusing area, and inversely proportional to the bubble diameter and overall tank area.

In their study of one-dimensional bubble plume modelling, Sahoo and Luktenia (2003) suggested that bubbles of close to 1 mm in radius gave a higher rate of oxygen transfer and mechanical efficiency than bubbles of larger sizes. Yum et al. (2008) simulated two-phase bubble plumes and calibrated/verified their model using experimental data. They showed the relationships between stratification efficiency, plume spacing, and de-stratification number. The data used for model calibration/verification were based on experiments conducted in a small tank under controlled environment. There are uncertainties in the suitability of the derived relationships for application to field conditions.

Rensen and Roig (2001) carried out an experimental study of two-dimensional bubble plumes in a confined tank to investigate non-stationary behaviour of the flow. Imteaz and Aseada (2000) concluded that the number of ports, air flow rate and bubbler starting time were important parameters for optimal bubbling operation. More modelling studies are needed to simulate the effects of bubbling operation before applications of the technique to real lakes.

The rate of mass transfer between gas and liquid is essential to the reactor performance.

2.4 Oxygen transfer rate

Submerged aeration systems in lakes are used to increase dissolved oxygen (DO) levels and stimulate water circulation. As the bubbles rise from the diffuser to the surface of water, oxygen will transfer to the water across the bubble interfaces. Moreover, at the free surface due to

turbulence induced by bubble plume motion and water circulation, oxygen transfer will also occur across the air-water interface (DeMoyer et al., 2003). Bubbles are often placed into the water due to their high surface area and tendency to generate their own turbulence (Gulliver, 2007).

It is important to know the gas-liquid mass transfer rate to evaluate the performance of the reactor (Huang at al., 2010, Wongsuchoto et al., 2003). In chemical engineering, the global mass transfer efficiency of an aerator system is usually expressed by a volumetric mass transfer coefficient, (Huang et al., 2010). The most important factors that affect the mass transfer between the gas-liquid phases are gas hold up, bubble size, slip velocity, and turbulent energy dissipation (Gao et al., 2015; Garcia-Ochoa and Gomez, 2004). In aeration systems, a better estimate of the K_La value will help to optimize the installations both in terms of cost and effectiveness. Numerous empirical and theoretical correlations have been developed for gas-liquid mass transfer in bubble columns and airlift reactors. The volumetric mass transfer coefficient can be predicted using experimentally determined correlations, empirical models and predictive models.

Huang et al. (2010) performed steady state simulation in an axisymmetric internal lift loop reactor. They reviewed various models of mass transfer between bubbles and liquid, and compared the results with experimental data by Jurascik et al. (2006). They found huge differences in predicted mass transfer coefficient using different models. They suggested that predictions from three models agree well with experimental data and are ideal for the estimation of mass transfer (Equation 29-30, 34). They recommended that the time model (Equation 30), has a better performance than others and it can be used for a wide range of bubbly flow compared with other models.

Wongsuchoto et al. (2003) illustrated the influence of different design and operating parameters on bubble size distribution in the airlift contactors (ALC). They also determined K_L and a were evaluated individually. They found that K_L does not change much with superficial gas velocity while the specific interfacial area does. They concluded that the specific interfacial area played a more significant role in controlling the rate of mass transfer in the system, rather than the K_L.

Kirshna and Van Baten (2003) developed a CFD model to examine the hydrodynamics and mass transfer in a bubble column operating in both homogenous and heterogeneous regime. They found an increase in both volumetric mass transfer (K_La) and gas hold up by increasing the superficial gas velocity.

Huang et al. (2009) applied a CFD model to simulate the flow of oxygen transport in high-speed surface aeration tanks. The simulated DO concentration of the CFD model was compared to the experimental results at two positions of the aeration tanks in different times. The predicted results of DO time variance showed good agreement with experimental results. They recommended their model as a new tool to study the oxygen transportation characteristics, scale up, and to optimize high-speed surface tanks.

Ferreira et al. (2013) conducted experiments in a laboratory scale bubble column, in order to analyze the influence of pH on the individual parameters of volumetric liquid side mass transfer coefficient, K_La, to achieve a better control of biological process. The change in pH level was achieved by addition of hydrochloric acid (HCl), phosphoric acid (H_3PO_4), and potassium hydroxide (KPH) to the system. They adopted Higbie's and Frossling's equations. They found that aqueous systems which contain HCl, H_3PO_4, or KOH present lower K_La values than pure systems

(distilled water). While, the specific interfacial area, *a*, values were lower in distilled water. They suggested that more studies need to be done on surface contamination in bubble column swarms.

DeMoyer et al. (2003) estimated the relative amount of surface and bubble oxygen transfer in an aerated water body. They modified the McWhirter and Hutter (1989) oxygen mass transfer model to consider both oxygen and nitrogen mass transfer as the bubbles rise through the water column. They determined the surface transfer coefficient $k_{Ls}a_s$ and bubble transfer coefficient K_La_b, separately. To obtain the best fit values for unknown parameters, K_La_b and $K_{Ls}A_s$, a nonlinear regression is performed on the unsteady oxygen mass transfer equation. They used experimental conditions to setup their model. The cylindrical tank was 9.6 m deep. They concluded that both surface and bubble water transfer contribute significantly to the total oxygen transfer in similar types of diffused aeration systems. However, the bubble water transfer is the primary mode of oxygen transfer at the selected flow rate for their system. They suggested that the results are valid for the aerated systems at similar depths or deeper water systems.

2.5 Turbulence closure models

Numerical simulations of bubble plumes in lakes using the Reynolds-averaged Navier-Stokes equations require the use of models for turbulence closure. Many turbulence closure models have been proposed in the literature. Their suitability for accurate predictions of fluid flows was investigated by a number of researchers (Hjarne et al., 2007; Schuler et al., 2011; Wang et al., 2008; Wei at al., 2013).

Wang et al. (2008) compared the performance of three turbulence models, namely the *k*-*ε* realizable model, the RNG (which stands for Renormalise Group) k-*ε* model, and the RSM (which stands for Reynolds stress model) linear model, in predictions of airflow in an enclosure. They

verified the results using experimental data. Among the three turbulence models, the RSM model showed flow patterns in the closest similarity to the experimental results, but none of the models captured adequately the experimental patterns of turbulence characteristics.

Hjarne et al. (2007) used three turbulence models, well referenced in the field of turbomachinary, in their investigation of the performance of an outlet guide vane. They predicted secondary flow, and conducted experiments for verification of the numerical predictions. The turbulence models used were the k-ε realizable, shear stress transport (SST) k-ω, and the RSM turbulence models. They concluded that the RSM model predicted secondary flow structures as well as losses of pressure with the best accuracy.

Schuler et al. (2011) combined experiments with computations to investigate the influence of turning vane arrangement on pressure loss and heat transfer in a two-pass channel with a 180 degree sharp turn. They suggested that the k-ε and SST k-ω models were quite accurate in predictions of pressure loss and heat transfer, whereas the SST k-ω and v^2-f turbulence models were capable of reproducing the locally increased heat transfer enhancement as observed in the experiments.

Wei et al. (2013) used three different turbulence models in their simulations of the three component force coefficient of a Sutong bridge girder section. They recommended the use of the standard k-ε model as it met accuracy requirements for simulating aerodynamics coefficient, instead of the use of the Reynolds stress model and Spalart-Allmaras model.

3 Methodology

Turbulent flows contain random fluctuations in velocity and pressure, which must be treated with statistical methods. Reynolds decomposition is used to modify the original unsteady Navier-Stokes equations. The idea behind this technique is to separate the average and fluctuating parts of a quantity to produce the Reynolds-averaged Navier-Stokes equations (or RANS equations). As statistical averaging procedures are employed to obtain these computations, the RANS equations are known as statistical turbulence models. Simulations using the RANS equations greatly reduce computational efforts compared to direct numerical simulations, but the procedures introduce additional terms called Reynolds stresses. Reynolds stresses contain products of the fluctuating quantities that must be modelled to close RANS equations.

A multiphase system consists of multiple phases. This research focuses on disperse multiphase systems, where one phase is considered as a continuum and the other phase is dispersed in the continuous one (Marchisio and Fox, 2007). When a phase has a non-continuous shape, such as a bubble, it is called dispersed. Air is dispersed in water as bubbles with a uniform diameter. To resolve a multiphase flow, the Eulerian approach is used and the pertinent equations are provided in Section 3.3.

It is possible to use three methods (mixture turbulence model, dispersed turbulence model, and turbulence model for each phase) for modelling turbulence in Eulerian multiphase flows within the k - ε model (ANSYS, 2013, p. 549). In this research, the dispersed turbulence model is utilized in the context of different turbulent closure models, where air bubbles are dispersed into a continuous phase - water.

3.1 Euler-Euler approach

In the Euler-Euler approach, the different phases are treated mathematically as interpenetrating continua. The concept of phasic volume fraction is introduced, since the volume of a phase cannot be occupied by the other phases. These volume fractions are assumed to be continuous functions of space and time and their sum is equal to one (ANSYS, 2013, p. 468). Individual solutions of the mass and momentum balances are needed and the phases interact through the interphase transfer terms (Diaz et al., 2008; Mudde and Simonin, 1999).

Multiphase flow CFD simulations typically employ Eulerian–Eulerian models (Diaz et al., 2008; Kadic and Heindel, 2014, p. 58; Pan et al., 2000; Yum et al., 2008).The Eulerian–Eulerian method is more popular since memory storage requirements and computer power demand depends on the number of computational cells considered instead of the number of particles (Kadic and Heindel, 2014, p. 59).

3.2 Dispersed turbulence model

A dispersed turbulence model is appropriate when the concentrations of the secondary phases are dilute. In this case, inter-particle collisions are negligible and the dominant process in the random motion of the secondary phases is the influence of the primary-phase turbulence. Fluctuating quantities of the secondary phases can therefore be given in terms of the mean characteristics of the primary phase, and the ratio of the particle relaxation time to eddy-particle interaction time. The model is applicable when there is clearly one primary continuous phase, and the rest are dispersed dilute secondary phases (ANSYS, 2013, p. 550).

3.3 Multi-phase (water and air bubbles) flows - the Eulerian approach

Model equations for computation of the velocity and pressure fields are described in this section. Let $(\widetilde{u}_1, \widetilde{u}_2, \widetilde{u}_3)$ denote the orthogonal components of the instantaneous velocity field in the Cartesian coordinates (x_1, x_2, x_3), respectively. Through Reynolds decomposition, the instantaneous velocity components are decomposed into time-averaged part (u_1, u_2, u_3) and fluctuating part (u_1', u_2', u_3'). The Reynolds decomposition can be expressed as:

$$\widetilde{u}_{wj} = u_{wj} + u'_{wj} \tag{3.1}$$

$$\widetilde{v}_{aj} = v_{aj} + v'_{aj} \tag{3.2}$$

where the subscripts w and a refer to water and air, respectively; α is the volume fraction; u_{wj} and u_{aj} is the x_j-direction components of the Reynolds-averaged velocity (in m/s) for water and air bubbles, respectively; the index j (equal to 1, 2 or 3) refers to directions.

3.3.1 Continuity equations

The Eulerian method is applied to the mass conservation for lake water and air bubbles. The continuity equations (in tensor form) are expressed as:

For water $$\frac{\partial}{\partial t}(\rho_w \alpha_w) + \frac{\partial}{\partial x_j}(\rho_w u_{wj} \alpha_w) = 0 \tag{3.3}$$

For air $$\frac{\partial}{\partial t}(\rho_a \alpha_a) + \frac{\partial}{\partial x_j}(\rho_a v_{aj} \alpha_a) = 0 \tag{3.4}$$

where α_w is the volume fraction of water in the computational cell in question; α_a is the volume fraction of air in the computational cell; ρ_w is the density of water (in kg/m^3); ρ_a is the density of air (in kg/m^3); t is time (in s). For any computational cell, the sum of α_w and α_a is one.

3.3.2 Momentum equations

The momentum equations in the x_j-direction can be written as:

For water

$$\alpha_w\left[\rho_w\left(\frac{\partial u_{wi}}{\partial t}+u_{wj}\frac{\partial u_{wi}}{\partial x_j}\right)\right]=\alpha_w\left[\frac{\partial p}{\partial x_i}+\left(\frac{\partial \tau_{wji}}{\partial x_j}\right)+\rho_w g_i\right]+F_{awi} \tag{3.5}$$

For air

$$\alpha_a\left[\rho_a\left(\frac{\partial u_{ai}}{\partial t}+u_{aj}\frac{\partial u_{ai}}{\partial x_j}\right)\right]=\alpha_a\left[\frac{\partial p}{\partial x_i}+\left(\frac{\partial \tau_{aji}}{\partial x_j}\right)+\rho_a g_i\right]+F_{wai} \tag{3.6}$$

where τ_{wji} and τ_{aji} are the specific Reynolds shear stresses (in N/m^2); p is Reynolds-averaged pressure (in Pa) shared by the two phases; g_i is the gravity vector component (m/s^2) in the x_i-direction; F_{awi} is the x_i-direction component of interfacial forces $\vec{F}_{aw}$ acting on the liquid phase; and F_{wai} is the x_i-direction component of interfacial forces $\vec{F}_{wa}$ acting on the gas phase.

The first term on the left hand side of Equation (3.5) or (3.6) is a transient term that describes local rate of the change in velocity. The remaining terms on the left hand side of the equation are convection terms. The first term on the right hand side of the equation is the pressure gradient. In Equations (3.5) and (3.6), the Reynolds-average pressure field and Reynolds-average velocity

components are unknown variables. In additional to these unknown variables, the equations contain six other unknown Reynolds shear stresses.

3.3.3 Interaction forces

The two phases (water as the liquid phase and air bubbles as the gas phase) are related through a momentum exchange (or transfer) term [Equations (3.5) and (3.6)]. The interphase momentum transfer is due to interfacial forces acting and interactions between water and air bubbles (Azzopardi et al., 2011, p. 130). These forces have to be formulated separately and fed back to the momentum equations [Equations (3.5) and (3.6)]. They are considered as sources or sinks in the momentum equations. They include the force due to viscous drag as well as the effects of lateral lift, turbulent dispersion, wall lubrication and virtual mass. Within the flow volume, these interfacial force densities would strongly govern the distribution of gas and liquid phase (Yeoh and Tu, 2009, p. 361).

Evaluations of the forces use models and correlations obtained experimentally are discussed below. Equation (3.5) involves the sum of five interfacial forces, expressed as:

$$\vec{F}_{aw} = \vec{f}_d + \vec{f}_l + \vec{f}_v + \vec{f}_w + \vec{f}_t \tag{3.7}$$

The terms on the right hand side of the equation represent forces acting on the liquid phase due to drag, lift, virtual mass, wall lubrication and turbulence dispersion, respectively. In Equation (3.5), the sum of five interfacial forces acting in the gas phase is given by:

$$\vec{F}_{wa} = -\vec{f}_d - \vec{f}_l - \vec{f}_v - \vec{f}_w - \vec{f}_t \tag{3.8}$$

3.3.3.1 Drag force

The drag force exerted by air bubbles on the surrounding liquid is computed as:

$$\vec{f}_d = k_d\left(\vec{v} - \vec{u}\right) \tag{3.9}$$

where k_d is the interphase momentum exchange coefficient (in kg/m^{3}s); $\vec{v}$ and $\vec{u}$ are the water and air-bubble velocity vectors, respectively. The coefficient is defined as $k_d = \alpha_a \alpha_w \rho_w f / \tau_p$, where f is a friction function, and τ_p is the particulate relaxation time (in s). This function is given by $f = C_D \,\mathrm{Re}/24$, where Re is the Reynolds number, and C_D is the drag coefficient. Schiller and Naumann (1935) suggested that $C_D = 24\left(1 + 0.15\,\mathrm{Re}^{0.687}\right)\mathrm{Re}$ if $\mathrm{Re} \le 1000$, and $C_D = 0.44$ if $\mathrm{Re} > 1000$. Re is defined as $\mathrm{Re} = \rho_a d_b \left|\vec{v} - \vec{u}\right| / \mu_a$, where μ_a is the dynamic viscosity of air. The relaxation time is evaluated as $\tau_p = \rho_w d_b^2 / \left(18\mu_a\right)$.

The drag force exerted by water on air bubbles is of equal magnitude as $\vec{f}_d$ but of the opposite sign (Equation 2). As a bubble rises in water, it will accelerate due to the buoyancy. However, it will decelerate due to the friction between the surface of the bubble and the surrounding liquid. The drag force has the most significant effect on air bubbles compared to the other interfacial forces. It dominates the control of the rise velocity of bubbles through the liquid phase and determines the residence time of the gas phase (Brucato et al., 1998; Khopkar and Ranade 2006; Lane et al. 2005; Roghair et al., 2009).

3.3.3.2 Lift force

The lift force acting on an air bubble is expressed as:

$$-\vec{f}_l = C_l \rho_w \alpha_a \left(\vec{u} - \vec{v}\right) \times \left(\nabla \times \vec{u}\right) \tag{3.10}$$

where C_l is a coefficient. Tomiyama (1998) and Frank et al. (2004) suggested that

$$C_l = \begin{cases} \min\left[0.288\tanh\left(0.121\mathrm{Re}_a\right), f\left(\mathrm{Eo}'\right)\right] & \text{if} \quad \mathrm{Eo}' \le 4 \\ f\left(\mathrm{Eo}'\right) & \text{if} \quad 4 \prec \mathrm{Eo}' \le 10 \\ -0.27 & \text{if} \quad 10 \prec \mathrm{Eo}' \end{cases} \tag{3.11}$$

where Re_a is Reynolds number; f is an empirical function, given by $f = 0.001Eo'^3 - 0.0159Eo'^2 - 0.0204Eo' + 0.474$; Eo′ = modified Eotvos number based on the long axis of the deformable bubble d_h. This dimensional parameter is given by $Eo' = g\left(\rho_w - \rho_a\right)d_h^2/\sigma$, $d_h = d_b\left(1 + 0.163Eo^{0.757}\right)^{1/3}$. The Eotvos number is defined as $Eo = g\left(\rho_w - \rho_a\right)d_b^2/\sigma$, where σ is the surface tension.

The lift force acting on water elements is of equal magnitude but opposite sign (Equation 3.10). The lift force acting on bubbles is mostly due to velocity gradients in the water flow field. This force is more significant for larger bubbles (ANSYS, 2013, p. 528). Different sides of bubbles may experience different flow conditions. The lift force is developed in a direction perpendicular to the main flow direction (Azzopardi et al., 2011, p. 132). Bubbles rising in a liquid are subjected to lateral lift force Due to horizontal velocity gradient (Yeoh and Tu, 2009, p. 363). The lift force acing on bubbles usually causes the radial or transverse motion of bubbles (Kulkarni, 2008).

3.3.3.3 Virtual mass force

The virtual mass force (or added mass force) is an additional force that is required to push away surrounding water elements to accelerate a bubble (Azzopardi et al., 2011, p. 132-133). The virtual mass effect occurs when the gas phase accelerates relative to the liquid phase. The inertia of the liquid phase mass encountered by the accelerating bubbles exerts a “virtual mass force” on the bubbles.

The virtual mass force in Equation (3.7) is given by:

$$-\vec{f}_v = C_{vm}\alpha_a\rho_w\left(d\vec{u}/dt - d\vec{v}/dt\right) \tag{3.12}$$

where C_{vm} is the virtual mass coefficient, equal to 0.5 for inviscid flow around an isolated sphere (Yeoh and Tu, 2009, p. 365). The virtual mass effect is significant because the density of the gas phase is much smaller than the density of the liquid phase, as in a bubble column.

3.3.3.4 Wall lubrication force

The wall lubrication force acts to push the gas phase away from walls (ANSYS, 2013). In contrast to the lateral lift force, wall lubrication force creates another lateral force due to surface tension which is formed to prevent bubbles from attaching on the solid wall. This results in a low void fraction at the vicinity of the wall area (Yeoh and Tu, 2009, p. 363). In Equation (3.7), the effect of the wall lubrication force on bubbles is implemented as:

$$-\vec{f}_w = C_{wl}\rho_w\alpha_a\left|\vec{u}-\vec{v}\right|_t^2\vec{n}_w \tag{3.13}$$

where C_{wl} is the wall lubrication coefficient; $\left|\left(\vec{u}-\vec{v}\right)\right|_t$ represents the phase relative velocity component tangential to the wall surface; $\vec{n}_w$ is the unit normal pointing away from the wall. The wall lubrication models in ANSYS Fluent differ in how they compute the wall lubrication coefficient, C_{wl}, in Equation (3.13). Two formulations have been investigated in this study.

The Tomiyama model (Tomiyama, 1998) modifies the wall lubrication force formulation of Antal (Antal et al., 1991) based on the results of experiments with flow of air bubbles in glycerin in a pipe. It allows positive and negative lift coefficients based on the bubble size. It also accounts

for the effects of bubble deformation and asymmetric wake of the bubble. The expression for C_{wl} for the Tomiyama model is:

$$C_{wl} = C_w \frac{d_b}{2}\left[\frac{1}{y_w^2} - \frac{1}{\left(d_p - y_w\right)^2}\right] \tag{3.14}$$

where d_p is the pipe dimeter and C_w depends on the Eotvos number, Eo, and hence on the surface tension between the two phases [equation (3.16)]. C_w is defined as:

$$C_w = \begin{cases} 0.47 & Eo < 1 \\ e^{-0.933Eo+0.179} & 1 \le Eo \le 5 \\ 0.00599Eo - 0.0187 & 5 \le Eo \le 33 \end{cases} \tag{3.15}$$

where the Eotvos number is defined as:

$$Eo = \frac{g\left(\rho_w - \rho_a\right)d_b^2}{\sigma} \tag{3.16}$$

that σ is the surface tension coefficient.

Frank et al. (2004), noted that although the Tomiyama wall lubrication model has been found to be superior to Antal model (Antal et al., 1991), it is restricted to flows in pipe geometries due to the dependence on pipe diameter. Frank et al (2004 and 2008) modified this correlation slightly to ensure continuous dependence of the wall lubrication coefficient on Eotvos number. The Frank model removed the dependence on pipe diameters in the Tomiyama model (Tomiyama, 1998), [Equation (3.14)].The wall lubrication coefficient defined by Frank model is as below

$$C_{wl} = C_w \max\left[0, C_{wD}^{-1}\left(1 - y_w C_{wc}^{-1} d_b^{-1}\right) y_w^{-1}\left(y_w C_{wc}^{-1} d_b^{-1}\right)^{1-p}\right] \tag{3.17}$$

where C_w(Eo) is dependent on the Eotvos number; C_{wD} is the damping coefficient, determining the relative magnitude of the force; y_w is the distance to the nearest wall; C_{wc} is a cut-off coefficient, determining the distance relative to the particle diameter over which the force is active; p is the power law constant, making the force fall off with a variable potential law relationship between $\vec{f}_{wl}$ and $1/y_w{}^p$. The model constants are $C_{wc}=10$, $C_{wD}=6.8$, and $p=1.7$.

3.3.3.5 Turbulence dispersion

The turbulence dispersion force acting on water elements [Equation (3.7)] is expressed as (Lopez-de-Bertodano, 1990):

$$\vec{f}_t = C_{td}\rho_w k \nabla \alpha_a \tag{3.18}$$

where k is the turbulent kinetic energy in the continuous phase, where C_{td} is a user-modified constant.Proper values for this constant are reportedly in the range of 0.1 to 0.5 for bubbly flow with bubble diameters in the order of a few millimeters. In this study, we take $C_{td}=0.3$.

The turbulence dispersion force acting on air bubbles [Equation (3.15)] is of equal magnitude but opposite sign. This force acts as a turbulent diffusion in dispersed flows of air bubbles.

3.3.4 Eddy viscosity

In Equations (3.5)–(3.6), τ_{wji} and τ_{aji} are extra unknown variables in addition to α_w, α_a, p, u_j and u_j. The RANS equations contain additional Reynolds stress terms which mean the equations are not fully closed, there are more unknowns than equations. Thus, a turbulence closure model is required to provide these extra equations (Menter, 2011). To close the system, we use the

Boussinesq approximation that relates the Reynolds shear stresses to the mean strain rate through an effective eddy viscosity. For phase *k* (air or water), the stress tensor is given by:

$$\tau_k = -\mu_{eff,k}\left(\nabla u_k + (\nabla u_k)^T\right) - \frac{2}{3} I(\nabla u_k) \tag{3.19}$$

For water, the effective eddy viscosity (in m^2/s) is given by $\mu_{eff,w} = \mu_w + \mu_{tw} + \mu_{ta}$, where μ_w is the molecular viscosity of water, μ_{tw} is the eddy viscosity due to the turbulence induced by water motions, and μ_{ta} is the eddy viscosity due to the turbulence induced by multi-bubbles motions inside water. According to Jakobsen et al. (1997), gas phase (air) effective viscosity is defined as:

$$\mu_{eff,a} = \left(\frac{\rho_a}{\rho_w}\right)\mu_{eff,w} \tag{3.20}$$

Sato and Sekoguchi (1975) suggested that $\mu_{ta} = \rho_w C_{\mu a} \alpha_a d_a \left|\vec{u} - \vec{v}\right|$ and, where $C_{\mu a}$ is a closure constant (equal to 0.6); d_b is the air bubble diameter; $\vec{v}$ is the air-bubble velocity vector; $\vec{u}$ is the water velocity vector.

The dispersed turbulence model is used when the dispersed phases are dilute, and in that case the continuous-phase (water) turbulence is regarded as the dominant process. Consequently, transport equations for turbulence quantities are only solved for the continuous phase, while the predictions of turbulence quantities for dispersed phases are obtained using the well-known Tchen theory (Hinze, 1975, p. 353). The transport equations for the primary phase in the case of the dispersed model are described below.

3.3.5 The standard *k-ε* model

The standard k-ε model is based on two transport equations: one written for the kinetic energy of turbulent fluctuations per unit mass k (in m^2/s^2), and the other for the dissipation rate of turbulent energy per unit mass ε (in m^2/s^3). Following Cokljat et al. (2006), we obtain μ_{tw} for the liquid phase (water) from:

$$\mu_{tw} = C_\mu \rho_w \left(\frac{k_w^2}{\varepsilon_w} \right) \tag{3.21}$$

The standard k-ε model was proposed by Launder and Spalding (1974). The equations are given by

$$\frac{\partial(\alpha_w \rho_w k_w)}{\partial t} + \frac{\partial(\alpha_w \rho_w u_{i,w} k_w)}{\partial x_i} = \frac{\partial}{\partial x_j}\left[\alpha_w \left(\mu_w + \frac{\mu_{tw}}{\sigma_k} \right) \frac{\partial k_w}{\partial x_j} \right] + \alpha_w G_{k,w} - \alpha_w \rho_w \varepsilon_w + \alpha_w \rho_w \Pi_{k,w} \tag{3.22}$$

$$\frac{\partial(\alpha_w \rho_w \varepsilon_w)}{\partial t} + \frac{\partial(\alpha_w \rho_w u_{i,w} \varepsilon_w)}{\partial x_i} = \frac{\partial}{\partial x_j}\left[\alpha_w \left(\mu_w + \frac{\mu_{tw}}{\sigma_\varepsilon} \right) \frac{\partial \varepsilon}{\partial x_j} \right] + \frac{\alpha_w \varepsilon_w}{k_w}\left(c_{1\varepsilon} G_{k,w} - c_{2\varepsilon} \rho_w \varepsilon_w \right) + \alpha_w \rho_w \Pi_{\varepsilon,w} \tag{3.23}$$

where μ_t is the turbulent dynamic eddy viscosity ($\mu_t = \rho \nu_t$). There are five empirical coefficients: $C_{\varepsilon 1}$= 1.44; $C_{\varepsilon 2}$ = 1.92; C_μ=0.09; σ_k =1.0; σ_ε = 1.3. Solving Equations (3.22) and (3.23) yields k and ε. $G_{k,w}$ is a source term for the production of turbulent kinetic energy and is defined as:

$$G_{k,w} = \mu_{tw} S_w^2 \tag{3.24}$$

where S is the modulus of the mean strain rate tensor

$$S_w = \sqrt{S_{w,ij} S_{w,ij}} \tag{3.25}$$

The term Π_{kw} can be derived from the instantaneous equation of the continuous phase and depends on volume fractions and densities, relative Reynolds number, bubble diameter, dynamic viscosity of water, the covariance of the velocities of the continuous phase w and dispersed phase a, the relative or slip velocity, and the drift (or dispersion) velocity (ANSYS, 2013; Mudde and Simonin, 1999).

$$\Pi_{kw} = \sum_{a=1}^{M} \frac{k_{wa}}{\alpha_w \rho_w} \left(k_{wa} - 2k_w + \vec{u}_{wa} . \vec{u}_{dr} \right) \tag{3.26}$$

where k_{wa} is the covariance of the velocities of the continuous phase (w) and the dispersed phase (a) ; $\vec{u}_{wa}$ is the relative velocity in m/s, and $\vec{u}_{dr}$ is the drift velocity in m/s.

$\Pi_{\varepsilon w}$ is modeled according to Elgobashi and Abou-Arab (1983):

$$\Pi_{\varepsilon w} = C_{3\varepsilon} \frac{\varepsilon_w}{k_w} \Pi_{kw} \tag{3.27}$$

where $C_3\varepsilon = 1.2$.

3.3.6 Realizable k-ε model

The realizable k-ε model differs from the standard k-ε model in two important ways:

(1) The realizable k-ε model contains an alternative formulation for the turbulent viscosity.

(2) A modified transport equation for the dissipation rate, ε, has been derived from an exact equation for the transport of the mean-square vorticity fluctuation.

The term "realizable" means that the model satisfies certain mathematical constraints on the Reynolds stresses, consistent with the physics of turbulent flows. Neither the standard *k-ε* model nor the *RNG k-ε* model is realizable.

$$\frac{\partial(\alpha_w\rho_w k_w)}{\partial t}+\frac{\partial(\alpha_w\rho_w u_{i,w}k_w)}{\partial x_i}=\frac{\partial}{\partial x_j}\left[\alpha_w\left(\mu_w+\frac{\mu_{tw}}{\sigma_k}\right)\frac{\partial k_w}{\partial x_j}\right] \tag{3.28}$$
$$+\alpha_w G_{k,w}-\alpha_w\rho_w\varepsilon_w+\alpha_w\rho_w\Pi_{k,w}$$

$$\frac{\partial}{\partial t}(\alpha_w\rho_w\varepsilon_w)+\frac{\partial}{\partial x_j}(\alpha_w\rho_w\varepsilon_w u_{w,i})=\frac{\partial}{\partial x_j}\left[\alpha_w\left(\mu_w+\frac{\mu_{w,t}}{\sigma_\varepsilon}\right)\frac{\partial\varepsilon_w}{\partial x_j}\right] \tag{3.29}$$
$$+\alpha_w\rho_w C_1 S\varepsilon_w+\alpha_w\rho_w C_2\frac{\varepsilon^2}{k+\sqrt{\upsilon\varepsilon}}+\alpha_w\rho_w\Pi_{\varepsilon,w}$$

In these equations, G_k represents the generation of turbulence kinetic energy due to the mean velocity gradients, calculated as in the *k-ε* Model; C_1 and C_2 are constants; σ_k and σ_ε are the turbulent Prandtl numbers for *k* and *ε*, respectively. The model constants are equal to: $C_1=\max\left[0.43,\frac{\eta}{\eta+5}\right]$; $\eta=S\frac{k}{\varepsilon}$; $S=\sqrt{2S_{ij}S_{ij}}$; $\sigma_k=1.0$; $\sigma_\varepsilon=1.2$; $C_2=1.9$.

As in other *k-ε* models, the eddy viscosity is computed from Equation (3.21). In contrast to the standard and RNG *k-ε* models, in the realizable *k-ε* model C_μ is no longer constant. Shih et al. (1995) proposed a modified eddy viscosity formulation where C_μ is variable.

$$C_\mu = \frac{1}{A_o + A_S \frac{ku^*}{\varepsilon}} \tag{3.30}$$

where u^* is

$$u^* = \sqrt{S_{ij}S_{ij} + \widetilde{\Omega}_{ij}\widetilde{\Omega}_{ij}} \tag{3.31}$$

The parameter $\widetilde{\Omega}_{ij}$ is defined as

$$\widetilde{\Omega}_{ij} = \Omega_{ij} - 2\varepsilon_{ijk}\omega_k \tag{3.32}$$

$$\Omega_{ij} = \overline{\Omega}_{ij} - \varepsilon_{ijk}\omega_k \tag{3.33}$$

where $\overline{\Omega}_{ij}$ is the mean rate-of-rotation tensor viewed in a moving reference frame with the angular velocity ω_k.

$$\overline{\Omega}_{ij} = \frac{1}{2}\left(\frac{\partial u_i}{\partial x_j} - \frac{\partial u_j}{\partial x_i}\right) \tag{3.34}$$

The model constants A_o and A_S are given by : $A_o = 4.04$; $A_s = \sqrt{6}\cos\phi$. Where $\phi = \frac{1}{3}\cos^{-1}\left(\sqrt{6}W\right)$; $W = \frac{S_{ij}S_{jk}S_{ki}}{\widetilde{S}^3}$; $\widetilde{S} = \sqrt{S_{ij}S_{ij}}$; $S_{ij} = \frac{1}{2}\left(\frac{\partial u_j}{\partial x_i} + \frac{\partial u_i}{\partial x_j}\right)$.

It can be seen that Cμ is a function of the mean strain and rotation rates, the angular velocity of the system rotation, and the turbulence fields k and ε.

3.3.7 RNG k-ε model

The RNG k-ε model was derived using a statistical technique called renormalization group theory. It is similar in form to the standard k-ε model, but includes the following refinements:

(1) The *RNG* model has an additional term in its ε equation that improves the accuracy for rapidly strained flows.

(2) The effect of swirl on turbulence is included in the RNG model, enhancing accuracy for swirling flows.

(3) The RNG theory provides an analytical formula for turbulent Prandtl numbers, while the standard k-ε model uses user-specified constant values.

(4) While the standard k-ε model is a high-Reynolds number model, the *RNG* theory provides an analytically-derived differential formula for effective viscosity that accounts for low-Reynolds number effects. Effective use of this feature does, however, depend on an appropriate treatment of the near-wall region.

These features make the RNG k-ε model more accurate and reliable for a wider class of flows than the standard k-ε model.

$$\frac{\partial}{\partial t}\left(\alpha_w \rho_w k_w\right)+\frac{\partial}{\partial x_i}\left(\alpha_w \rho_w k_w u_{w,i}\right)=\frac{\partial}{\partial x_j}\left[\alpha_w\left(\mu_w+\frac{\mu_{w,t}}{\sigma_k}\right)\frac{\partial k_w}{\partial x_j}\right] + \alpha_w\left(G_{k,w}-\rho_w \varepsilon_w\right)+\alpha_w \rho_w \Pi_{k,w} \tag{3.35}$$

$$\frac{\partial}{\partial t}\left(\alpha_w \rho_w \varepsilon_w\right)+\frac{\partial}{\partial x_i}\left(\alpha_w \rho_w \varepsilon_w u_{w,i}\right)=\frac{\partial}{\partial x_j}\left[\alpha_w\left(\mu_w+\frac{\mu_{w,t}}{\sigma_\varepsilon}\right)\frac{\partial \varepsilon_w}{\partial x_j}\right] + \alpha_w\left(C_{1\varepsilon}\frac{\varepsilon_w}{k}p_k - C_{2\varepsilon}^{*}\rho_w\frac{\varepsilon^2}{k}\right)+\alpha_w \rho_w \Pi_{\varepsilon,w} \tag{3.36}$$

where the coefficients are equal to : $C_{\varepsilon 1}$= 1.42; $C_{\varepsilon 2}$ = 1.68; C_{μ}=0.0845; σ_k =0.7194; σ_{ε} = 0.7194.

$C_{2\varepsilon}^{*}$ is defined as:

$$C_{2\varepsilon}^{*} = C_{2\varepsilon} + \frac{C_{\mu}\eta^{3}\left(1-\eta/\eta_{o}\right)}{1+\beta\eta^{3}} \tag{3.37}$$

where $\eta = Sk/\varepsilon$ and $\eta_o = 4.38$; S is defined by equation (3.25). The terms on the left-hand side of Equations (3.35) and (3.36) denote the rate of change of k or ε and transport of k or ε by convection, respectively. While the terms on the right-hand side mean the transport of k or ε by diffusion, rate of production of k or ε, and rate of destruction of k or ε, respectively.

3.3.8 The shear stress k-ω model

The shear-stress transport (SST) model was developed by Menter (1994) to effectively blend the robust and accurate formulation of the model in the near-wall region with the freestream independence of the model in the far field.

$$\frac{\partial}{\partial t}\left(\alpha_w k_w \rho_w\right) + \nabla.\left(\alpha_w \rho_w k_w u_w\right) = \nabla.\left(\alpha_w\left[\mu_w + \frac{\mu_{tw}}{\sigma_{k3}}\right]\nabla k_w\right) + \alpha_w\left(P_w + G_w - \rho_w \beta' k_w \omega_w\right) + S_{k,w}^{\text{int}} \tag{3.38}$$

$$\frac{\partial}{\partial t}\left(\alpha_w \rho_w \omega_w\right) + \nabla.\left(\alpha_w \rho_w \omega_w u_w\right) = \nabla.\left(\alpha_w\left[\mu_w + \frac{\mu_{tw}}{\sigma_{\omega 3}}\right]\nabla \omega_w\right) + 2\alpha_w \rho_w\left(1-F_1\right)\frac{1}{\sigma_{\omega 2}\omega_w}\nabla k_w \nabla \omega_w + \alpha_w \alpha_3 \frac{\omega_w}{k_w}\left(P_w + C_3\left\|G_w\right\|\right) - \alpha_w \rho_w \beta_3 \left(\omega_w\right)^2 + S_{\omega,w}^{\text{int}} \tag{3.39}$$

where P_w and G_w are the exact production terms derived in equations (3.24) and (3.25), while $S_{k,w}^{\text{int}}$ and $S_{\omega,w}^{\text{int}}$ are source or sink terms that are added to the system of equations to account for the production and dissipation of turbulence due to the interaction between the continuous and disperse phases. For example, large particles are known to enhance turbulence due to the production of a turbulent wake behind the particles or of bubbles in a liquid in most physical encounters. On the other hand, small particles or bubbles are known to suppress the turbulence in the flowing fluid (Yeoh and Tu, 2009, p. 61). The shear production P_w is:

$$P_w = \mu_{tw}\nabla u_w.\left(\nabla u_w + \left(\nabla u_w\right)^t\right) - \frac{2}{3}\nabla .u_w\left(\mu_{tw}\nabla .u_w - \rho_w u_w\right) \tag{3.40}$$

The production due to the gravity can be written as

$$G_w = -\frac{\mu_{tw}}{\rho_w \sigma_{\rho_w}} g.\nabla \rho_w \tag{3.41}$$

3.3.9 Reynolds stress modelling (RSM) turbulence model

In the RSM model, individual Reynolds stresses (τ_{ji}) are computed by differential equations. The transport equation for the continuous phase Reynolds stresses in the case of the dispersed model can be written as:

$$\begin{aligned}
&\frac{\partial}{\partial t}\left(\alpha\rho\tau_{ij}\right) + \frac{\partial}{\partial x_k}\left(\alpha\rho u_j \tau_{ij}\right) = -\alpha\rho\left(\tau_{ik}\frac{\partial u_j}{\partial x_k} + \tau_{jk}\frac{\partial u_i}{\partial x_k}\right) + \frac{\partial}{\partial x_k}\left[\alpha\mu\frac{\partial}{\partial x_k}\left(\tau_{ij}\right)\right] \\
&-\frac{\partial}{\partial x_k}\left[\alpha\rho\overline{u_i' u_j' u_k'} + \alpha p\left(\delta_{jk}u_i' + \delta_{ik}u_j'\right)\right] + \alpha p\left(\overline{\frac{\partial u_i'}{\partial x_j} + \frac{\partial u_j'}{\partial x_i}}\right) - \alpha\rho\varepsilon_{ij} \\
&-2\alpha\rho\Omega_k\left(\tau_{jm}\varepsilon_{ikm} + \tau_{im}\varepsilon_{jkm}\right) + \Pi_{R,ij}
\end{aligned} \tag{3.42}$$

where the second term on the left-hand side is the convection term. The terms on the right-hand side of the equation represent the stress production, molecular diffusion, turbulent diffusion, pressure strain, dissipation, and production by system rotation, respectively. The last term, $\Pi_{R,ij}$,takes into account the interaction between the continuous and the dispersed phase turbulence. A general model for this term can be of the form:

$$\Pi_{R,ij} = K_{dc} C_{1,dc} \left(R_{dc,ij} - R_{c,ij} \right) + K_{dc} C_{2,dc} a_{dc,i} b_{dc,j} \tag{3.43}$$

where C_1 and C_2 are unknown coefficients, $a_{dc,i}$ is the relative velocity, $b_{dc,j}$ represents the drift or the relative velocity, and $R_{dc,ij}$ is the unknown particulate-fluid velocity correlation. The following assumption has been made, to simplify this unknown term:

$$\Pi_{R,ij} = \frac{2}{3} \delta_{ij} \Pi_k \tag{3.44}$$

where δ_{ij} is the Kronecker delta, and Π_k represents the modified version of the original Simonin model (Simonin and Viollet, 1990).

$$\Pi_{kc} = K_{dc} \left(\widetilde{k}_{dc} - 2\widetilde{k}_c + \widetilde{V}_{rel} . \widetilde{V}_{drift} \right) \tag{3.45}$$

where $\widetilde{k}_c$ is the turbulent kinetic energy of the continuous phase (water), $\widetilde{k}_{dc}$ represents the continuous-dispersed phase velocity covariance and finally, $\widetilde{V}_{rel}$ and $\widetilde{V}_{drift}$ are the relative and drift velocities, respectively.

3.3.10 Numerical method - the Eulerian approach

In this proposed research, the pressure-based coupled algorithm is used to numerically solve the model equations [Equations (3.3) – (3.6)] for the velocity and pressure fields. This algorithm is an extension of the Semi-Implicit Method for Pressure Linked Equations (SIMPLE) algorithm (Chung, 2002, p. 108) to multiphase flow problems. The SIMPLE algorithm has been extensively used to numerically solve the Navier-Stokes equations for applications to different kinds of fluid flow and heat transfer problems. In the SIMPLE solution procedure, a pressure correction equation is derived by manipulating the continuity and momentum equations [e.g. Equations (3.3) and (3.5) or Equations (3.4) and (3.6)].

In the pressure-based coupled algorithm, the velocity components (u_1, u_2, u_3) of water and air bubble motions are solved in a segregated fashion and coupled by the liquid and gas phases. The solution procedures involve a sequence of steps. The first step is to update the density field, turbulent eddy viscosity and diffusivity based on the current time step solution.

The second step is to use the block algebraic multigrid scheme to solve a vector equation formed by the velocity components of all phases [Equations (3.5) and (3.6)] simultaneously. The velocity components (u_1, u_2, u_3) are solved sequentially from Equations (3.5) and (3.6), using the recently updated values of pressure and face mass fluxes. Note that the equations contain non-linear terms and the velocity components are coupled. Thus, it is necessary to obtain the solution by iterations in order to achieve a converged numerical solution.

The third step is to build a pressure correction equation from total volume continuity rather than mass continuity. This equation is solved for the pressure correction, using the recently obtained velocity field and the mass-flux. Corrections are made to face mass fluxes, pressure, and the velocity field using the pressure correction.

The fourth step is to update the source terms arising from the interactions between water and air bubbles. This is followed by a check for the convergence of the equations. The steps listed above are continued until the convergence criteria are met.

The above-mentioned numerical solution method differs from the density-based solution method. The latter method has been used mainly for high-speed compressible flows, by which the density field is obtained from the continuity equation, and the pressure field is determined from the equation of state.

3.3.11 Heat transfer theory, the energy equation

The energy equation is expressed in the following form (ANSYS, 2013, p. 133-134):

$$\frac{\partial}{\partial t}(\rho E)+\nabla.(\vec{v}(\rho E+p))=\nabla.\left[k_{eff}\nabla T-\sum_{j}h_{j}\vec{J}_{j}+\left(\bar{\bar{\tau}}_{eff}.\vec{v}\right)\right]+S_{h} \qquad (3.43)$$

where k_{eff} is the effective conductivity, which is the sum of the fluid thermal conductivity (k) and turbulent conductivity (k_t); E is the total energy. The first three terms on the right-hand side of the equation (3.43) represents energy transfer due to conduction, species diffusion, and viscous dissipation, respectively. S_h is for volumetric heat transfer. The total internal energy of the fluid is:

$$E=h-\frac{p}{\rho}+\frac{v^{2}}{2} \qquad (3.44)$$

where h is the sensible enthalpy and is defined as

$$h = \sum_j Y_j h_j \tag{3.45}$$

where Y_j is the mass fraction of species j and

$$h_j = \int_{T_{ref}}^{T} c_{p,j} dT \tag{3.46}$$

The value for T_{ref} in the sensible enthalpy calculation depends on the solver and models in use.

For pressure-based solver T_{ref} is 298.15 K.

4 Results of Aeration-induced Artificial Flow in a Cylinder

Eutrophication has been a worldwide lake pollution problem, with serious consequences. It arises from the presence of excessive nutrients in lakes and resultant algal blooms. Nutrients can come from an external or internal source. The release of phosphorus from resuspended sediments from the lake bottom represents a significant internal source. This chapter addresses the issue of how to effectively control anoxic and sedentary condition in eutrophic lakes. We considered using artificial-circulation technique, and carried out CFD modelling of artificial circulation triggered by air-bubble injection into the lake water at the bottom. The simulations are based on the Reynolds-average Navier-Stokes equations written for two phases (water and air bubble, equations are given in Chapter Three). They are solved using the Eulerian methods. We predict distributed water and air-bubble velocities, as well as air volume fraction, which can be used to determine dissolved oxygen concentration (Sections 4.4 and 4.7). The predictions compare reasonably well with experimental data [Figure 4.6 (a)-(o)]. We show that turbulent eddy motions cause oxygenated surface water to flow downward and effectively mix with the bottom water, and injected air bubbles directly enhance the dissolved oxygen level (Section 4.6, Figure 4.15) . This application demonstrates that using proper methods for interphasal forces and turbulence closure is the key to success.

4.1 Introduction

The objective of this chapter is to investigate the use of computational fluid dynamics (CFD) methods as applied to the flow of a mixture of water and air bubbles in a reservoir. Air bubbles are continually released at the bottom of the water column, rise toward the water surface, and cause water flow in the reservoir. The flow field of aerated water is quite intricate, and reliable

computation can be difficult to obtain with any CFD code. This research uses the CFD software package Fluent (version 15, ANSYS 2013) to compute the flow field, and examines the accuracy of computation by comparing computational results to laboratory data.

The finite volume method is employed to numerically integrate the momentum and continuity equations, which govern the flow field, over time on a discrete mesh. An important question that arises is whether the numerical solutions are independent of mesh configuration and whether they converge in time. Other important questions arise about: 1) the appropriateness of individual turbulence models provided as options in Fluent; 2) the suitability of using symmetry formulation or a wedge domain to enhance computing efficiency. All these questions need to be answered quantitatively, for example by determining numerical error associated with numerical solutions.

The computational domain used in this paper was a water holding tank of cylindrical shape (Figure 4.1). It had a radius of R = 25 cm, and contained water of 40 cm in height. Air bubbles of size d_b = 3 mm entered the water column through a vertical circular port of diameter d_p = 6 cm located at the center of the base of the tank. The air flow rate was q = 200 cm^3/s. The bubbles rose to the free water surface, crossed it and entered the standard atmosphere, where the pressure was p = 101.325 kPa. Anagbo and Brimacombe (1990) conducted laboratory experiments of resultant bubbly flow in the tank. They reported an initial upward velocity of v_o = 8.5 cm/s at which bubbles entered the water column. This velocity is somewhat higher than the value of 7.78 cm/s as calculated from the flow rate and the cross-sectional area of the port. The total volume of bubbles entering the water over a time period of 327 *s* would be equal to the total volume of water held in the tank. The laboratory experiments produced data of air-bubble velocity, water velocity and air volume fraction at a series of positions inside the tank [Figure 4.1(b), the symbols '+']. These laboratory data will be used to validate the CFD predictions in this paper.

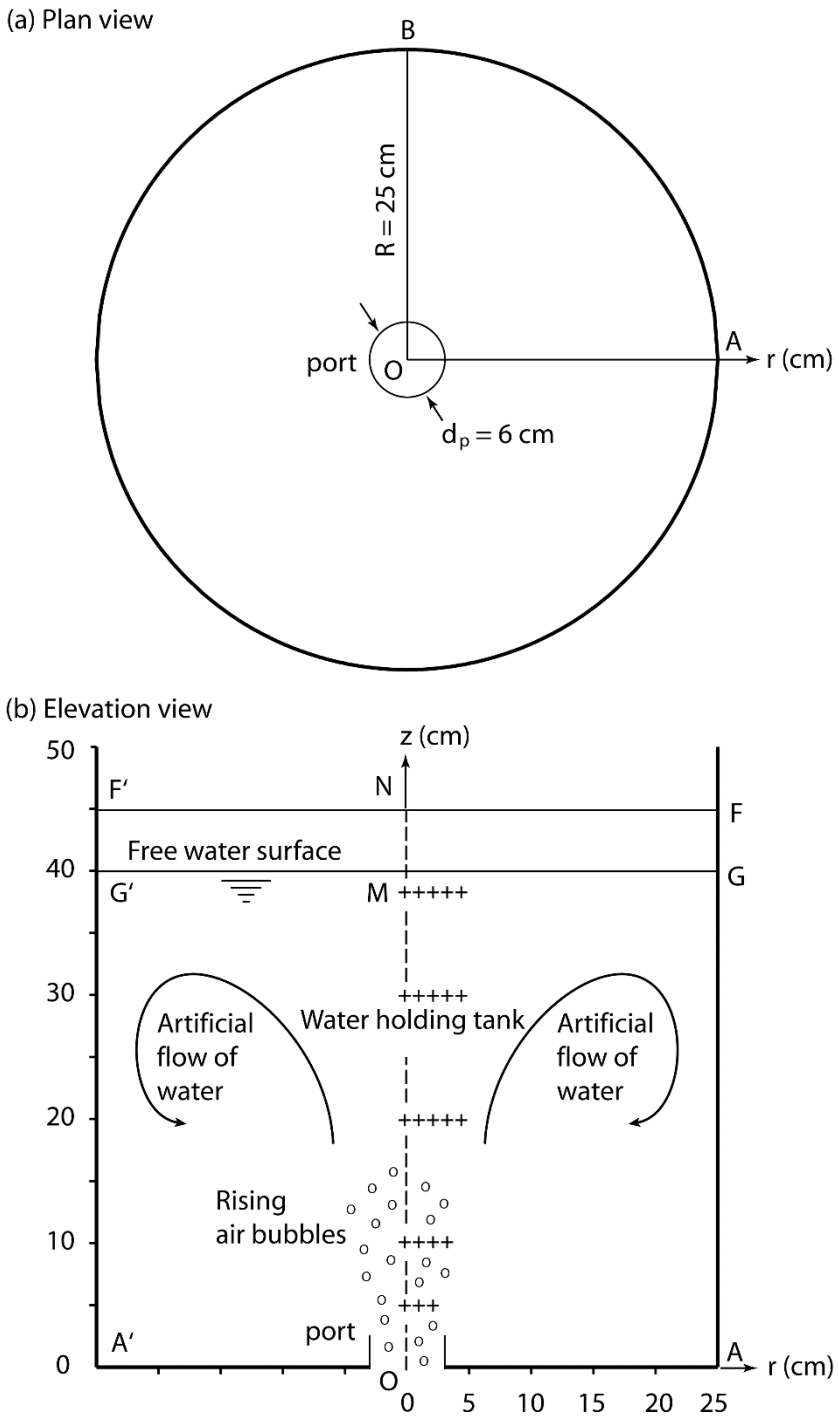

Figure 4.1 Water holding tank of cylindrical shape, used for measurements of water velocity, air bubble velocity, and air volume fraction: (a) plan view; and (b) elevation view. The plus markers indicate the positions of the measurements.

4.2 Background

The water quality of lakes deteriorates due to eutrophication, as has been widely observed (Ansari et al. 2011, p. 17; Bates and DeWreede 2007; Matsui et al. 1995). The problem of eutrophication occurs when excessive amounts of nutrients are present in the lake water and substantially increase algae yields. Nutrients can come from an external source or an internal source or both. The former includes such examples as discharges of domestic and industrial waste effluents into lakes and agricultural fertilizers that are washed into lakes by rainwater. The latter refers to the release of nutrients (most importantly phosphorus) from re-suspended lake-bottom sediment particles. With regard to the consequences of eutrophication, the growth of algae typically forms a thin greenish layer in the lake water, and thus reduces light penetration into the lower water column. As algae die, bacteria feed on them. This process uses oxygen and inevitably lowers the dissolved oxygen level of the lake water, which leads to fish kills, as reported in Ansari et al. (2011, p. 18).

Aeration is a plausible field technique for the remediation of lake eutrophication. The main beneficial effects of the technique are outlined below: First, air bubbles injected to the bottom of a lake can directly raise dissolved oxygen levels in the lower water column. The condition created will help block the internal source of nutrients (Cook et al. 1993). Penn et al. (2010) and Sharpley et al. (1994) suggested that under specific conditions, it is more important to control the internal source than external sources. Second, as bubbles rise under the influences of initial momentum and buoyance forcing, they interact with surrounding water elements in the lake, and result in artificial circulation and turbulent motions of fluids (Figure 4.1). The possible down-welling of more oxygenated surface water to the bottom allows an efficient renewal of the bottom water. Also, the artificial flow work against lake stratification, which often occurs in lakes when water temperature decreases with increasing depth from the lake surface, and which prohibits upwelling

of the bottom water. Thus, lake de-stratification achieved by the aeration technique is desirable. Third, this technique requires no chemical substances, which certainly is an advantage over other remediation techniques.

The design of aeration systems should be such that they produce efficient circulation and vigorous turbulent mixing in the entire lake of interest. Many independent variables have influence on the flow field. The first set of variables are variables related to air injection, including bubble size (d_b), initial velocity (v_o), and air flow rate (q). The second set of variables are diffuser variables, including the number of ports, port diameter or diffusion area (d_p), spacing between adjacent ports, port angle with the horizontal (ϕ), and elevation of ports above the lake bottom. The third set of variables are variables related to reservoir conditions, including the depth of water, horizontal dimensions (R), and distributions of the density of water or water temperature.

Given the extensive list of independent variables, it will be very costly and time-consuming to perform comprehensive field or laboratory testing. The computational approach is comparatively efficient and practical. It is quite feasible to systematically obtain CFD predictions of circulation and turbulence characteristics for given values of the variables, and to use the predictions to develop a suitable test matrix, limiting test cases.

The knowledge about the influence of the independent variables on the flow field is far from complete, although some of them have been identified from previous investigations of the problem of artificial flow. According to an experimental study (Kim et al., 2010), the efficiency of de-stratification was proportional to the diffusion area, and inversely proportional to the bubble size (d_b) and the aeration tank dimensions (Figure 4.1). Laboratory measurements of bubble plumes (Rensen and Roig 2001) made from a confined tank showed two-dimensional behaviour of bubble

plumes. The flow was non-stationary, as revealed by optical fibre probe and video camera measurements. The water depth did not affect plume structures. Imteaz and Aseada (2000) attempted to optimize bubbling operations in the laboratory by changing the number of ports, air flow rate, and bubble starting time. According to a computational study (Sahoo and Luktenia, 2003), bubbles with $d_b \approx 1$ mm produced oxygen transfer with a higher rate and mechanical work with a higher efficiency than bubbles of larger sizes. Based on computational results, Yum et al. (2008) related stratification efficiency to plume spacing and de-stratification number. It is worth noting that existing laboratory measurements were made mostly from small tanks under controlled environment. How reliable the findings based on such measurements are under field conditions is a question worthy of further investigation.

4.3 Methods

4.3.1 Continuity and momentum principles

The water and air-bubble flow velocities (u_j and v_j) as well as distributed air volume fraction are computed using the Reynolds-averaged continuity and momentum equations [Equations (3.3)–(3.6) in Chapter 3]. We use the Eulerian approach and the pressure-based coupled algorithm for numerical solutions of the velocity and pressure fields. This algorithm is an extension of the Semi-Implicit Method for Pressure Linked Equations (SIMPLE) algorithm (Chung 2002, p. 108) to multiphase flow problems. In the SIMPLE solution procedure, a pressure correction equation is derived by manipulating the continuity and momentum equations. In the pressure-based coupled algorithm, u_j and v_j are solved in a segregated fashion and coupled by the liquid and gas phases.

Using the Eulerian approach and the pressure-based coupled algorithm, the model equations (3.3)–(3.6) are solved numerically for velocity and pressure fields. The algorithm is an extension of the

Semi-Implicit Method for Pressure Linked Equations (SIMPLE) algorithm (Chung 2002, p. 108) to multiphase flow problems. In the SIMPLE solution procedure, a pressure correction equation is derived by manipulating Equations (3.3)–(3.6). In the pressure-based coupled algorithm, the flow velocities (u_j and v_j) are solved in a segregated fashion and coupled by the liquid and gas phases. The solution procedures are outlined below:

- Update the density field, turbulent eddy viscosity and diffusivity based on the current time step solution;
- Use the block algebraic multi-grid scheme to solve a vector equation formed by u_j and v_j simultaneously; solve the velocity components in a phase-coupled manner, but in a segregated fashion, using the recently updated values of pressure and face mass fluxes; obtain the solution by iterations in order to achieve a converged solution;
- Build a pressure correction equation from total volume continuity rather than mass continuity; solve the equation for the pressure correction, using the recently obtained velocity field and the mass-flux; correct face mass fluxes, pressure, and the velocity field using the pressure correction;
- Update the source terms arising from the interactions between water and air bubbles; check for the convergence.

The previously mentioned steps are continued until the convergence criteria (10^{-6}) are met.

4.3.2 Turbulence closure

For turbulence closure, a wide range of flow applications have used the standard k-ε model, RNG k-ε model, realizable k-ε model, shear stress transport (SST) k-ω model and second-order Reynolds stress model (RSM). However, there is no consensus about which of these models is the most

reliable. To the best of our knowledge, no assessment of their performance as applied to bubble flow has been reported in the literature. This chapter will provide a performance comparison.

The standard k-ε model [Equations (3.21)–(3.23) in Chapter 3] computes the turbulence kinetic energy, *k*, and the turbulence length scale as $l = C_u^{3/4} k^{1.5} \varepsilon^{-1}$. It can be used to predict properties of bubbly flow with no prior knowledge of turbulence structure. The two-equations [(3.22) and (3.23)] model includes several empirical closure coefficients and auxiliary relations.

In the RNG k-ε model, the Navier-Stokes equations are renormalized to account for the effects of smaller scales of motion, in comparison to *l*. The result is a modified form of Equation (3.23) to account for the different scales of motion through changes to the production term (Yakhot et al. 1992).

In the Realizable k-ε model, the *k* equation has the same form as Equation (3.22) but different model constants, and the ε equation does not contain the same production term G_w as in Equation (3.24). The model uses a new ε equation, based on the dynamic equation of the mean-square vorticity fluctuation, in an attempt to improve prediction of the spreading rates of axisymmetric jets from the standard k-ε model and the RNG k-ε model. The coefficient C_μ in Equation (3.21) no longer has the standard constant value of 0.09. It is a function of the mean strain, rotation rates, *k* and ε. The model is intended to capture such flow features as strong streamline curvature, vortices, rotation, flow separation, and complex secondary flow.

SST k-ω model computes *k* and the turbulence length scale *l* as $l = C_\mu^{-1/4} k^{1/2} \omega^{-1}$, where ω is the specific dissipation rate. In this model, a *k*-ω formulation (ANSYS 2013, p. 58) is used for the inner region of a wall boundary layer down to the wall surface through the viscous sub-layer (a

low Reynolds number region), whereas a k-ε formulation (ANSYS 2013, p. 47) is used for the free-stream region. The k-ω formulation handles low Reynolds number conditions well, but it makes prediction excessively sensitive to inlet free-stream turbulence properties (k and ω). The switch from k-ω to k-ε formulation is intended to avoid the excessive sensitivity. The SST k-ω model captures flow behaviour in adverse pressure gradients and flow separation. However, it tends to over-predict turbulence levels in regions of large normal strain such as stagnation regions and regions with strong acceleration.

The RSM (Wilcox 2006, p. 322) computes the specific Reynolds-stress tensor from stress-transport equations, derived from the momentum principle. The model includes the effects of streamline curvature, sudden change in strain rate and secondary flow. Unlike the eddy-viscosity models mentioned above, RSM does not need to model the turbulence production terms. It incurs higher computing costs than the other models.

4.3.3 Interfacial forces

This section provides a brief description of different interfacial forces that are used in this study. A detailed description of models and their equations are given in the previous chapter, Chapter 3.

The two phases (water as the liquid phase and air bubbles as the gas phase) are related through a momentum exchange (or transfer) term [Equations (3.5) and (3.6)]. The interphase momentum transfer is due to interfacial forces acting and interactions between water and air bubbles (Azzopardi et al., 2011, p. 130). These forces have to be formulated separately and fed back to the momentum equations [Equations (3.5) and (3.6)]. They are considered as sources or sinks in the momentum equations. They include the force due to viscous drag as well as the effects of lateral lift, turbulent dispersion, wall lubrication and virtual mass. Within the flow volume, these

interfacial force densities would strongly govern the distribution of gas and liquid phase (Yeoh and Tu, 2009, p. 362). Equation (3.5) involves the sum of five interfacial forces. These are drag force (f_d), lift force (f_l), virtual mass force (f_v), turbulent dispersion force (f_t), and wall lubrication (f_w) force. In Equations (3.7) and (3.8), the sum of five interfacial forces acting the water and gas phase is given, respectively. Fluent provides a wide range of physical models for these forces. These interfacial models used in this study are described in Chapter 3 and are listed in Table 4.1.

4.4 Model results

A total of 19 model runs (Table 4.1) were carried out for numerical solutions to the Reynolds-averaged Navier-Stokes (RANS) equations on structured finite volume mesh, under the same conditions as the laboratory experiments reported in Anagbo and Brimacombe (1990). The RANS equations are given in Chapter 3. The model runs were designed to compare the performance of various computational methods / treatment, as outlined below:

- Comparison of turbulence closure models (Runs TC1 to TC5): a) the standard k-ε model (k-ε); b) the RNG k-ε model (RNG k-ε); c) the k-ε realizable model (Realizable k-ε) ; d) the shear stress transport k-ω model (SST k-ω); and e) the Reynolds stress model (RSM).
- Mesh validation (Runs MSH1, MSH2, MSH3, MSH4 and MSH5): The focus was on testing the effect of mesh refinement and grid structure on CFD results. The node count of the mesh used for computation is given in Table 4.3.
- Validation of domain treatment (Runs BC3 to DM1), serving a twofold purpose: First, the mesh used for the first 12 runs (Table 4.1) covered the 40 cm water column up to the free water surface [Figure 4.1(b)]. The mesh for BC3 was extended to cover an additional section of 5 cm high above the water surface [Figure 4.1(b)]. Although the extension gave

rise to an increase in computing node and hence in computing time, it served the purpose to test the effect of pressure outlet condition on possible outflow error at the top boundary.

- Second, the mesh used for DM2 (Table 4.1) was two-dimensional axis-symmetrical mesh. It covered half the width of the tank [Figures 4.1(a) and 4.1(b)]. The mesh used for DM1 covered the full width of the tank. Although the axis-symmetrical mesh is more efficient in computing than the full width mesh because the former has lower node count, and although the use of the former can be justified by the fact that the tank of cylindrical shape [or the physical domain, Figure 4.1(a)] is actually symmetrical about its axis, it is constructive to test the effect of the symmetry constraint applied on the flow field inside the physical domain. Comparing results between the two runs will show the effect. The mesh used for DM3 and DM4 was a three-dimensional 10° and 90° wedge, respectively. It was intended to show possible differences between two-dimensional and three-dimensional computing approaches.
- Time step convergence (Runs TA1 and TA2): These runs were intended to determine how small the time step needs to be to obtain accurate predictions.

Table 4.1 Summary of setup for CFD model runs. All runs use the Eulerian approach. The time step Δt is 0.001 *s* for all runs, except Run TA2 for which Δt is 0.1 *s*.

Run	Turbulence closure	Model domain	Mesh size (mm)	Inflation	Lift force	Turbulent dispersion	Wall lubrication	Turbulence interaction	Top boundary condition
TC1	Standard k-ε	A	5	yes	TM	LDB	Frank	Sato	de-gassing
TC2	SST k-ω	A	5	yes	TM	LDB	Frank	Sato	de-gassing
TC3	RNG k-ε	A	5	yes	TM	LDB	Frank	Sato	de-gassing
TC4	RSM	A	5	yes	TM	LDB	Frank	Sato	de-gassing
TC5	Realisable k-ε	A	5	yes	TM	LDB	Frank	Sato	de-gassing
BC1	SST k-ω	A	5	yes	TM	LDB	TM	-	atmospheric pressure
BC2	SST k-ω	A	5	yes	TM	LDB	TM	-	de-gassing
BC3	SST k-ω	2D-AS[b]	5	yes	TM	LDB	TM	-	atmospheric pressure
DM1	k-ε	A	5	yes	-	-	-	-	atmospheric pressure
DM2	k-ε	B	5	yes	-	-	-	-	atmospheric pressure
DM3	k-ε	C	5	yes	-	-	-	-	atmospheric pressure
DM4	k-ε	D	5	yes	-	-	-	-	atmospheric pressure
MSH1	k-ε	A	5	yes	-	-	-	-	atmospheric pressure
MSH2	k-ε	A	5	No	-	-	-	-	atmospheric pressure
MSH3	k-ε	A	3+C		-	-	-	-	atmospheric pressure
MSH4	k-ε	A	3+F		-	-	-	-	atmospheric pressure
MSH5	k-ε	A	1	No	-	-	-	-	atmospheric pressure
TA1	k-ε	A	5	yes	TM	LDB	Frank	Sato	de-gassing
TA2	k-ε	A	5	yes	TM	LDB	Frank	Sato	de-gassing

[a]2D-AS = two-dimensional axis-symmetrical mesh.

[b]E2D-AS = extended two-dimensional axis-symmetrical mesh.

LDB = Lopez-de-Bertodano; TM = Tomiyama;

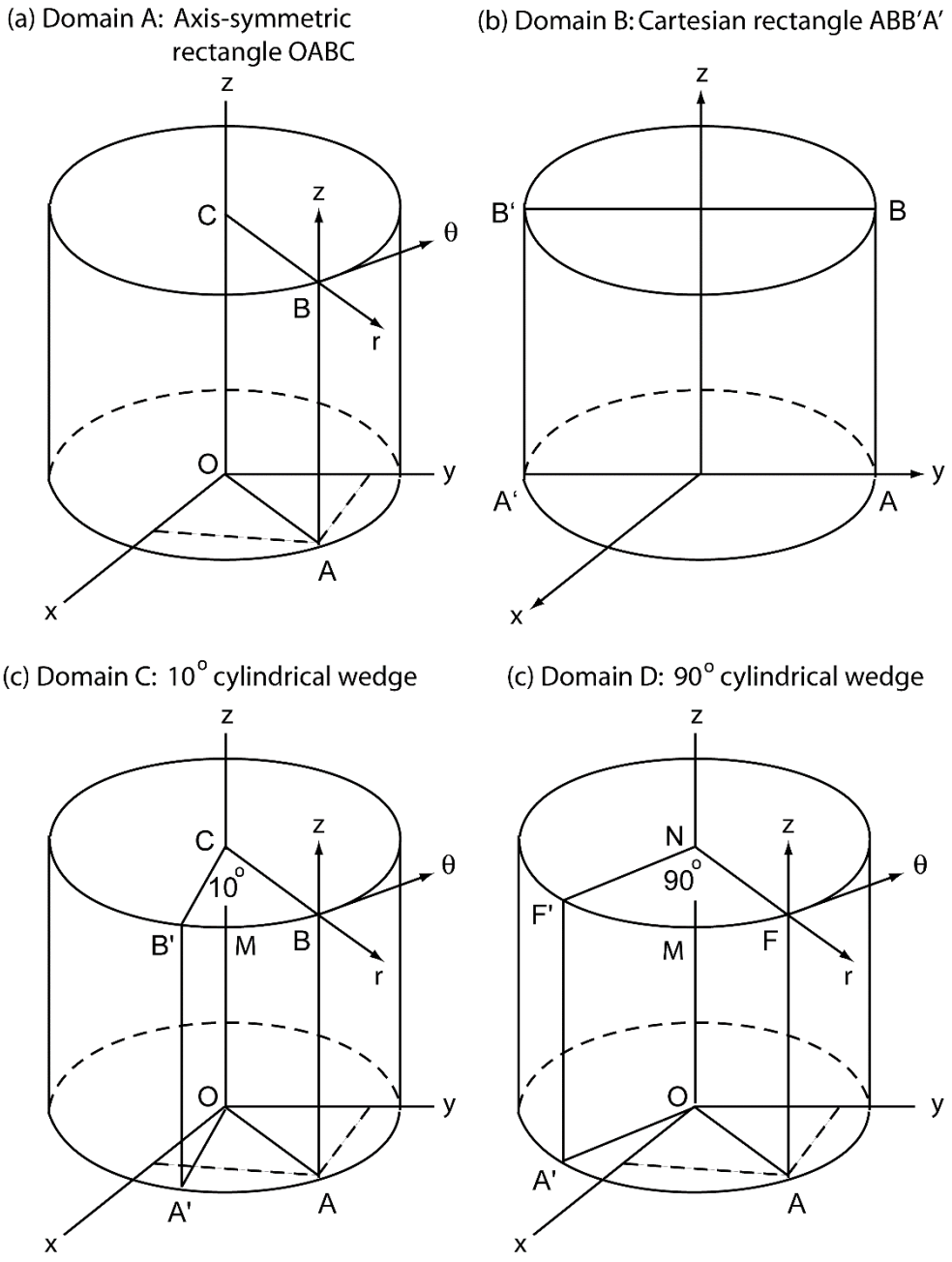

Figure 4.2 Model domains A, B, C and D, used for computer simulations of bubbly flow in the experimental tank (Figure 4.1): (a) a half-width, axis-symmetric (about the *z*-axis) plane (θ equal to a constant) in the cylindrical coordianate system (r,θ,z); (b) a full-width yz plane in the Cartesian coordinate system (x,y,z); (c) a cylindrical wedge of $\Delta\theta = 10^{\circ}$ [Figure 4.1(a)] bounded by rectangles OABC and OA′B′C in the cylindrical coordianate system; and (d) a cylindrical wedge of [Figure 4.1(a)] bounded by rectangles OABC and OA′B′C in the cylindrical coordianate system. The cylinders have the same dimensions as the tank shown in Figure 4.1.

4.4.1 Initial and boundary conditions

Initial conditions imposed at time $t = 0$ are as follows: The free water surface is located at the equilibrium position [Figure 4.1(b)]. The volume fraction of water α_w is equal to one below the free surface. The velocity components are zero in the entire model domain.

Kinematic and/or dynamic conditions are imposed at the following boundaries [Figure 4.1(b)]: a) the port (located at the bottom of the tank), through which air bubbles enter the water column; b) the outlet at the top of the model domain; c) solid sidewalls of the tank; d) the axis of the tank (for all the model runs listed in Table 1, except for Runs DM2, DM3 and DM4); e) Symmetry (for Runs DM3 and DM4).

At the port [Figure 4.1(b)], air bubbles of $d_b = 3mm$ enter the model domain continuously. The direction of their velocity is upward, and the magnitude is prescribed. The volume fraction of water α_w is zero.

At the outlet [Figure 4.1(b)], fluids are exposed to the standard atmosphere. Accordingly, the pressure relative to the atmospheric pressure is zero. The volume fraction of water α_w is set to zero.

At the solid sidewalls, a no-slip condition is applied. The wall distance (y^+) of the first cell from the walls is below unity. Thus, the no-slip condition is valid. This condition means that both the tangential and normal velocity components are zero.

4.4.2 Simulated bubbly flow field

Under given conditions, the model runs listed in Table 4.1, produce water velocities. As an example, water velocity vectors and contours at a state of equilibrium for run TA1 are plotted in

Figures 4.3 (a) and (b), respectively. Only one half of the axisymmetric flow field is shown in Figures 4.3 (a-b), [OAGM in Figure 4.1 (b)].

A strong jet is seen to occur in the center region [Figures 4.3 (a and b)], as a direct response to bubble injection. Water motions are visible in the entire domain. The jet flow entrains water from both sides in the lower water column and creates eddies [Figures 4.3(a and b)]. These eddies produce diverging flows from the center in the upper water column. Water flow converges to compensate the upward motion at the center. These flow features are realistic. Also, there are upward and downward motions on both the left and right sides of the water body. These flow patterns would enhance renewal of bottom water with oxygenated surface water.

Figures 4.3 (a and b) demonstrate strong upward flow in the central region above the air injector and downward flow near the column walls. The flow reverses from upward to downward at the distance of $r/(H) = 0.42$ beyond the centreline axis, approximately. For run TA1 [Figure 4.3 (b)], the maximum velocity has a magnitude of nearly six times of the initial velocity, v_o, of bubbles entering the water column.

The water velocity vectors [Figure 4.3(a)] show clockwise eddy motions on the right side of the centreline. These eddy motions penetrate the entire water depth, meaning that aeration is effective in producing exchange of water masses. The radius of significant influence is larger than four times the inlet diameter d_p. Water circulation occurs over virtually the whole width of the water body. In other words, artificial circulation can effectively be created by injecting air bubbles.

Because of its buoyancy, the dispersed phase (air bubble) moves away from the discharge source; likewise, the continuous phase (water) is set in motion in reaction to the drag force on each bubble.

The buoyant bubble plume so produced rises to the surface, spreading radially, and entrains liquid from the pool, inducing a large-scale recirculation.

Moreover, Figure 4.3 (a) shows that the water flow starts to bend when approaching the surface (for $z/H > 0.9$). The degassing condition at the outlet boundary allows modelling a free surface, where dispersed bubbles can escape from the domain, but not the liquid phase. As a result of this condition the entrained water cannot continue its upward motion when it reaches the surface in contrast to the air bubble which is released upwards into the atmosphere. Thus, the rising water is diverted into a radial flow outwards from the plume. A vortex ring distribution was observed below the free surface. The centres of the vortex near the top free surface is clearly evident (where $r/H = 0.375$ and $z/H = 0.75$).

Furthermore, near the water surface, the water flow in the horizontal direction for a radial distance of $r/H < 0.42$ from the centreline axis. Figure 4.3 (a) shows that the maximum velocity in the horizontal direction is observed to be near the free surface. This means that the horizontal velocity is fastest on the free surface since there is no shear stress acting on the free surface.

In Figure 4.3 (b) the water velocity contour of $u_2 = 0$ depicts that the plume is narrow near the port exit. Above the port, it turns into a wider and diffusive plume about $2.5d_p$, where d_p (=0.06 m) is the port diameter. The descending flow region is located adjacent to the column wall. This region is characterized by downward liquid streams that is free of bubbles at low gas velocities. In the region close to the column wall, a descending liquid flow can always be found due to the lack of bubble motions. The axial and radial flow reversals clearly identify the convection flow pattern in the model domain.

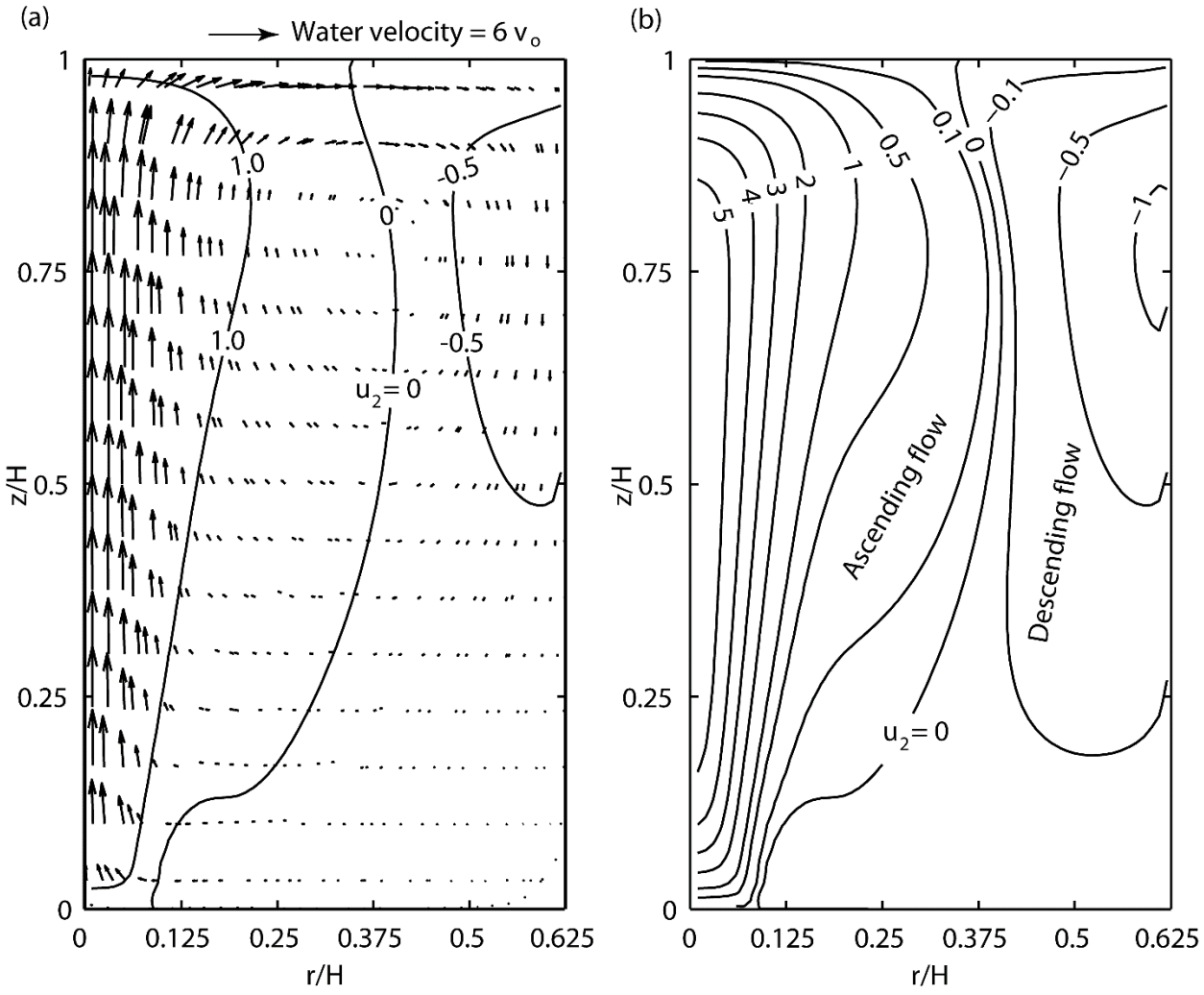

Figure 4.3 Predicted water flow in the model domain shown in Figure 4.2(a) for Run TA1 (Table 4.1): (a) vectors of water velocity normalized by the initial velocity (v_o) of air bubbles; and (b) contours of the z-direction component (u_2) of water velocity normalised by the initial velocity (v_o).

Figure 4.4 (a) depicts the air velocity vectors for the run TA1. Since the flow pattern inside the domain is axisymmetrical with regard to the central bubble column, only half of the domain is presented [OAGM in Figure 4.1 (b)]. Air velocity is higher in the centre column, in accordance to higher gas volume fractions. The maximum air velocity has a magnitude of $10v_o$ for run TA1. The

maximum vector length corresponds to the maximum velocity ($10v_o$). Air flow rises along the domain up to the water surface. Air velocity vectors going up and out of the columns represent the degasification condition at the outlet boundary, which allows gas to flow out of the domain, for a proper mass balance. This condition allows modelling a free surface, where dispersed bubbles can escape from the domain, but not the liquid phase.

Figure 4.4 (b) illustrates air velocity contours. As the air bubbles are emitted into the water through the port, the bubbles will ascend and expand producing bubble plume along the centreline. It is observed that the region with the highest velocity is in the middle of the domain. It can also be concluded from the air velocity contour that air velocity is zero in the regions where the existence of dispersed bubbles are very low. The transverse extent of the dispersed bubbles is increased with distance from the bottom of the domain.

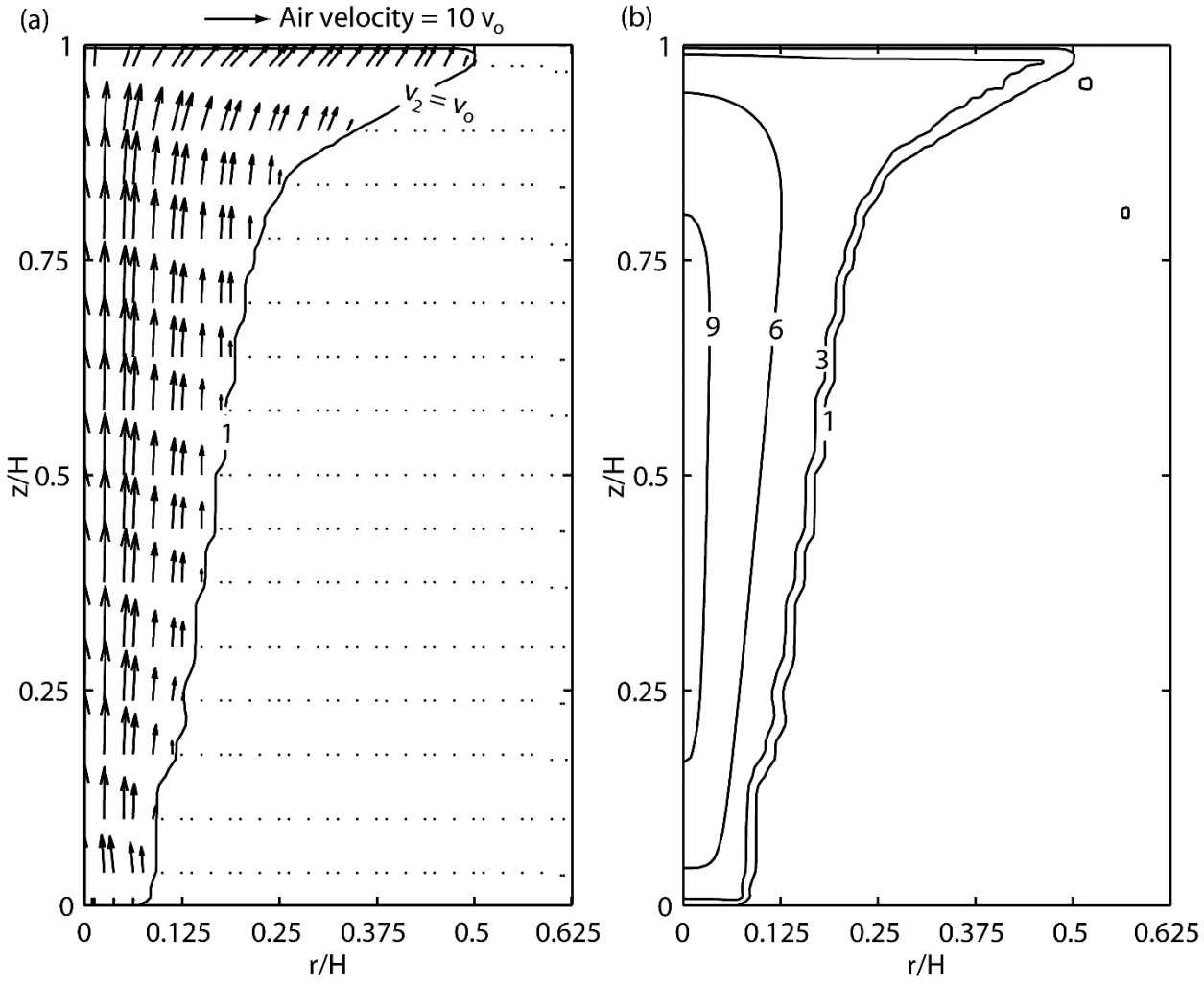

Figure 4.4 Predicted air bubble flow in the model domain shown in Figure 4.2(a) for run TA1 (Table 4.1): (a) vectors of air bubble velocity normalised by the initial velocity (v_o) of air bubbles; and (b) contours of the z-direction component (v_2) of air bubble velocity normalised by the initial velocity (v_o).

Figure 4.5 presents air volume fraction in the bubble column. Only one half of the axisymmetric model domain is shown (The right hand-side of Figure 4.1 (b), OAGM). A bubble plume is formed at the centre of the column. In the near-wall regions, gas fraction is zero and maximum near the port (Figure 4.5). The profile of air volume fraction tends to broaden towards the surface of the domain. The air volume fraction contours show that the higher volume fraction region is close to

the port, where the bubble inlet is located, reaching a maximum of α_a = 20%. The air volume fraction drops slowly as it goes up through the columns and reaches the top of the column due to the degasification condition at the outlet boundary. This condition allows modelling a free surface, where dispersed bubbles can escape from the domain, but the liquid phase cannot.

It can be seen that at the bottom of the domain, where the bubble inlet is located, the profile has a high concentration of gas near the centre line of the column, while the profile tends to broaden towards the top of the domain.

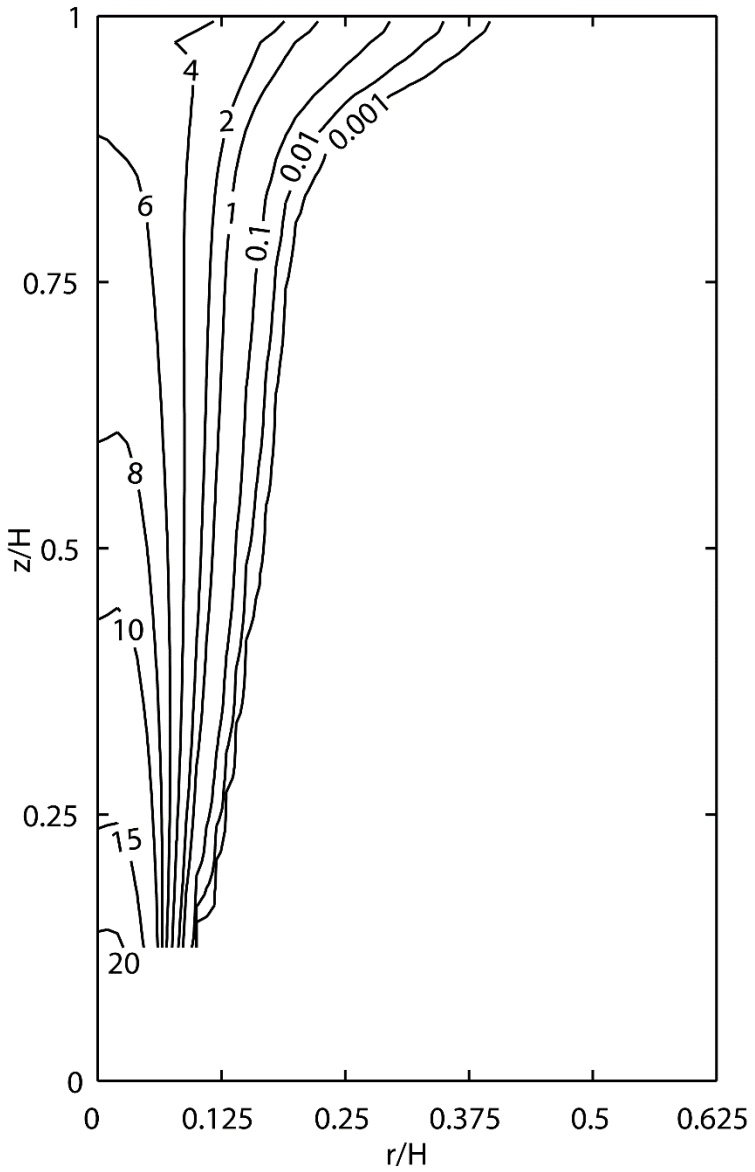

Figure 4.5 Contours of air volume fraction (α_a in per cent) in the model domain shown in Figure 4.2(a) for Run TA1 (Table 4.1).

The vertical component of predicted water velocities at five selected heights (z/H = 0.0625, 0.125 0.25, 0.75, and 0.95, where H = 0.4 m) above the bottom, varying with radial distance, r/ d_p, from the centre, are plotted In Figures 4.6 (a)-(e). Values are extracted from the model results for Run TA1 at model times of t = 20 s. The diameter of air bubbles injected is d_b = 3 mm. The velocity

component has peak values at the centre (or $r/d_p = 0$), and decreases rapidly with radial distance r/d_p. It drops to zero at $r/d_p \approx 2.75$ further away from the centreline, the flow reverses direction from upward to downward. This is true at all heights above the bottom. The predictions of water velocity are supported by experimental data (Anagbo and Brimacombe, 1990), which shows similar features. Water velocity intensifies with increasing height above the inlet, and weakens with increasing radial distance.

Variations in bubble rising velocity, u_a, with r are shown in Figures 4.6 (f)-(j). The air velocity values are extracted from the model results at model time of $t = 20$ s for the same heights as in Figures 4.6 (a)-(e). The rising velocities decrease from their peak values at the centre with increasing radial distance; the same feature was observed from experiments (Anagbo and Brimacombe, 1990). At larger height from the inlet, the model predictions are closer to experimental results.

Due to buoyancy, bubble rises faster than ambient water velocity. This difference is defined as bubble slip velocity. The following example illustrates such differences. Run TA1 produced air-bubble rising velocities in the range of 0.49 (at $z/H = 0.95$, Figure 4.6(f)) to 0.8 m/s [at $z/H = 0.75$, Figure 4.6(g)] along the centreline, compared to vertical velocities of water elements in the range of 0.21 [at $z/H = 0.95$, Figure 4.6(a)] to 0.49 m/s [at $z/H = 0.75$, Figure 4.6(b)]. The air-bubble velocities relative to those of water, bubble slip velocities, are as large as 0.31 m/s.

Distributions of predicted air volume fraction, α_a, with radial distance from the centreline are shown in Figures 4.6 (k)-(o). Values of α_a are extracted from the model results for Run TA1 at model time of $t = 20$ s for the same heights as in Figures 4.6 (a)−(e). The snapshots show that at a given height, air volume fraction decreases from peak values with increasing radial distance. The

peak values occur slightly off the centre. The predicted air volume fraction agreed well with the experimental data.

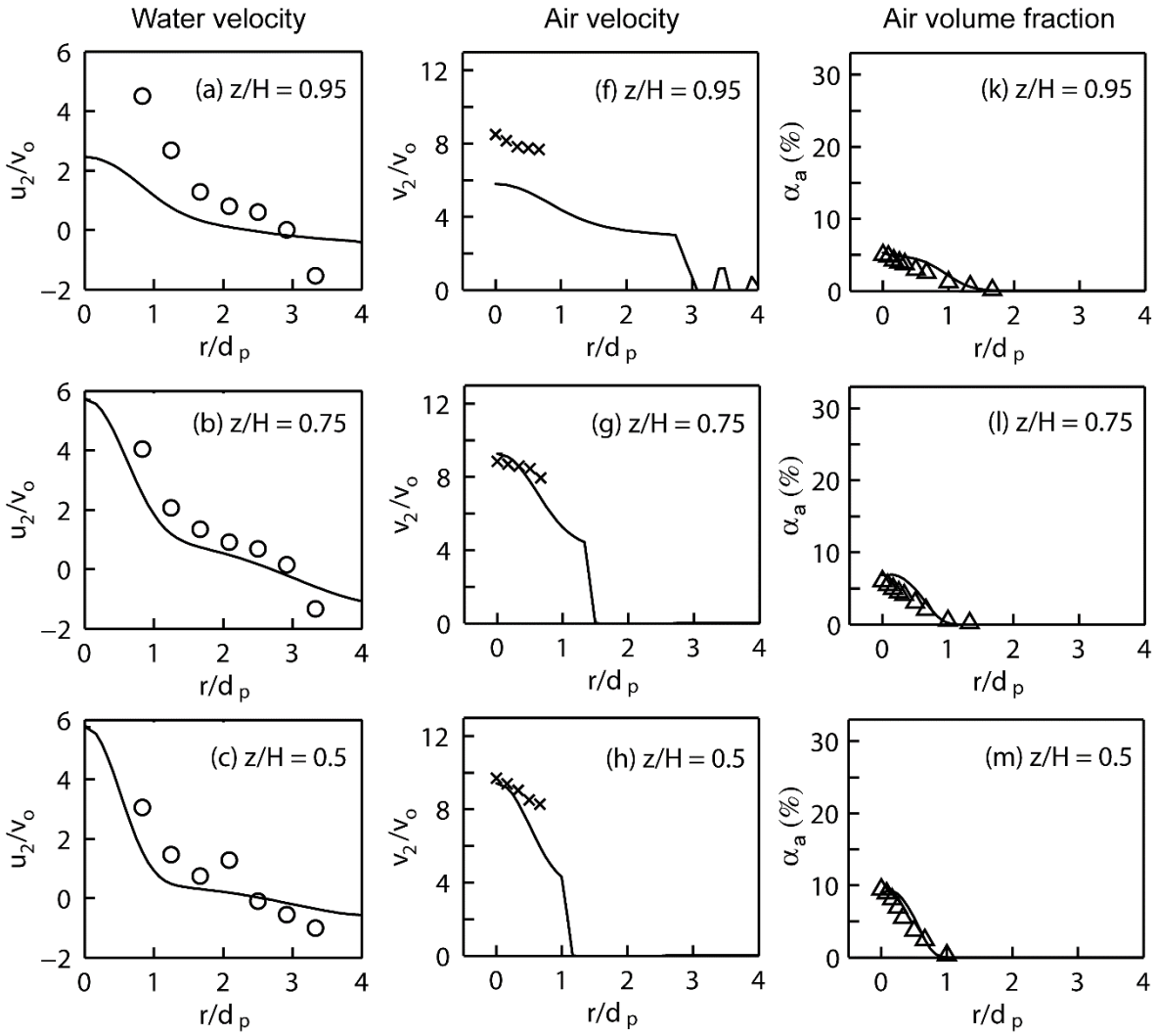

Figure 4.6 Profiles [the solid curves for Run TA1 (Table 4.1)], showing that the predicted *z*-direction water velocity [u_2 in Panels (a)–(e)], z-direction air bubble velocity [v_2 in Panels (f)–(j)], and air volume fraction [α_a in Panels (k)–(o)] decrease with radial distance *(r)* from the centreline $\overline{OC}$ of the model domain [Figure 4.2(a) and Figure 4.1(b)]. Measured z-direction water velocity (the open circle markers), *z*-direction air bubble velocity (the cross markers), and air volume fraction (the triangle markers) are shown for comparison.

Figure 4.6 (Continued).

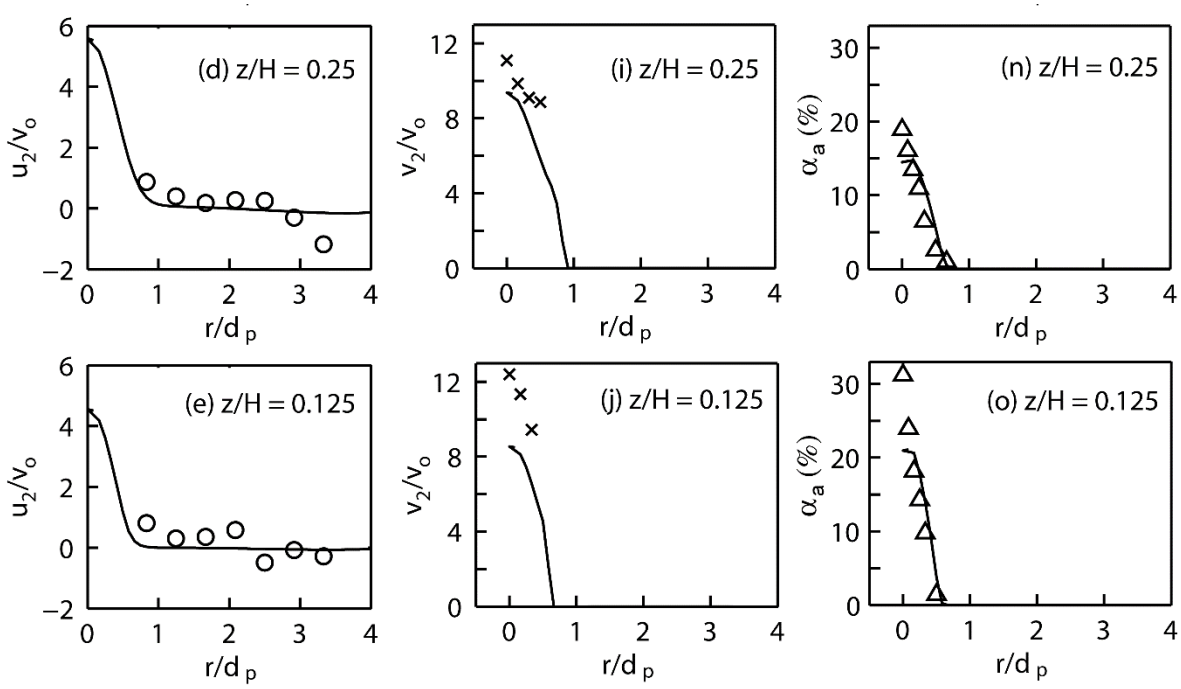

4.4.3 Quality of model domains

For the perspective of computation efficiency, domain A [Figure 4.2(a)] is the most desirable. This is simply because this domain has the lowest count of computing nodes of a given mesh size, among the four domains [Figures 4.2(a)-(d)]. The efficiency of computation using domain A is the highest. Domain D has the highest count of computing nodes, and thus the efficiency of computation is the lowest. A comparison of node count between the four domains is given in Table 4.2.

Table 4.2 Percentage errors in predicted air velocity (v_a), water velocity (v_w) and air volume fraction (α_a) for four simulations using different model domains. The mean value and standard deviation errors are determined using the data at z/H = 0.25, 0.50, and 0.75.

Simulation ID (Table 1)	Model domain [Figs. 2(a)-(d)]	Node count	Mean value ± standard deviation of percentage errors		
			δv_a	δu_w	$\delta \alpha_a$
DM2	A	6837	-21.4% ± 3.6%	-83.0% ± 9.7%	-0.5% ± 1.4%
DM1	B	13589	-33.1% ± 4.5%	-17.1% ± 178.2%	-0.2% ± 1.3%
DM3	C	33580	-1.6% ± 10.0%	-86.8% ± 11.4%	-0.5% ± 1.2%
DM4	D	223991	-5.4% ± 8.4%	-80.4% ± 9.9%	-0.4% ± 1.1%

We performed four simulations (Table 4.2, Table 4.1), each using a different domain [Figures 4.2(a)-4.2(d)] to represent the water tank [Figure 4.1(a)], and compared the predicted air velocity (v_a), water velocity (u_w) and air volume fraction (α_a) with measured values reported in Anagbo and Brimacombe (1990). These simulations used identical conditions as outlined below: (1) The time step was 0.001 s; (2) the turbulence closure model used was the standard k-ε; (3) the bubble size was 0.003 mm; (4) the initial air velocity was 0.085 m/s; (5) the mesh size was 5 mm with inflation; (6) at the outlet, pressure outlet was used as the boundary condition. In order to access the domains' suitability, percentage errors were analysed.

The percentage errors δv_a, δu_w, and $\delta \alpha_a$ for air velocity, water velocity and air volume fraction, respectively, are defined by

$$\delta v_a = \frac{v_a - v_{ao}}{v_{ao}} \times 100\%; \qquad \delta u_w = \frac{u_w - u_{wo}}{u_{wo}} \times 100\%; \qquad \delta \alpha_a = \frac{\alpha_a - \alpha_{ao}}{\alpha_{ao}} \times 100\% \qquad (4.1)$$

where v_{ao}, u_{wo} and α_{ao} are the measured air velocity, water velocity and air volume fraction, respectively. The individual percentage errors are expected to have different values for the different positions marked by the symbols '+' in Figure 4.1(b). The mean of these different values

and the standard deviation are calculated for each of the four simulations, and are listed in Table 4.3. Note that the total positions are 22, 35, and 40, for calculations of the mean and standard deviations of δv_a, δu_w and $\delta \alpha_a$, respectively.

From Table 4.2, a number of observations were made: (1) Using any of the model domains has produced acceptable errors in α_a; (2) using domain B has given the largest mean of δv_a and the largest standard deviation of δu_w among all the simulations, and thus it is less preferable, although the efficiency of computation is relatively high; (2) using domain C has substantially reduced the mean of δv_a and the standard deviation of δu_w from the corresponding values associated with using domain B; (3) using domain D has produced a mean value and standard deviation of δv_a close to those associated with using domain C, and has slightly improved δu_w; (4) using domain A has been seen to match the performance of domains C and D in terms of δu_w, although it has underperformed to some extent in terms of δv_a. Domain A is preferable because it gives a comparatively better performance and the highest efficiency of computation. This domain will be used for subsequent simulations.

4.4.4 Mesh convergence

Five simulations were carried out to understand the influence of mesh configurations on predictions. These simulations used different mesh systems to cover domain A [Figure 4.2(a)]. The first mesh has a cell size of 5 mm with inflation. The second mesh has a uniform cell size of 5 mm without inflation. The third mesh has a cell size of 3 mm with inflation and with refinement in the vicinity of the lines $\overline{OC}$ and $\overline{OA}$ [Figure 4.2(a)]. The fourth mesh has a cell size of 3 mm with inflation and with refinement in the vicinity of the line $\overline{OC}$ [Figure 4.2(a)]. The fifth mesh has a uniform cell size of 1 mm.

These simulations used the same conditions. The time step was 0.001 *s*. The turbulence closure model was the standard k-ε. At the outlet, pressure outlet was a boundary condition. The bubble size was 3 mm. The initial air velocity was 0.085 m/s. Results are extracted from the model predictions at model time of $t = 10.7$ *s*, and are compared in Table 4.3.

Table 4.3 Percentage errors in predicted air velocity, water velocity and air volume fraction for five simulations using different mesh configurations. The mean value and standard deviation errors are determined using the data at $z/H = 0.25$, 0.50, and 0.75.

Simulation ID	Mesh	Mean value ± standard deviation of percentage errors		
		δv_a	δu_w	$\delta \alpha_a$
MSH1	5-mm mesh with inflation	-22.5% ± 2.3%	-79.3% ± 15.0%	0.3% ± 0.4%
MSH2	5-mm mesh without inflation	-21.4% ± 3.6%	-83.0% ± 9.7%	0.4% ± 0.3%
MSH3	3-mm mesh with inflation and refined central and bottom areas	-19.5% ± 3.6%	-85.5% ± 10.6%	0.4% ± 0.4%
MSH4	3-mm mesh with inflation and a refined central area	-20.3% ± 3.5%	-85.0% ± 10.3%	0.4% ± 0.4%
MSH5	1-mm mesh without inflation	-27.9% ± 3.2%	-85.7% ± 10.8%	0.4% ± 0.4%

Predictions of v_a, u_w and α_a for the five runs are extracted from the model results at $t = 10.7$ *s*, and their percentage errors are summarized in Table 4.3. Clearly, the use of the mesh for MSH2 gives the largest standard deviation of δv_a among the five mesh configurations and larger mean of δu_w in comparison to MSH1. Thus, it is less preferable, although the efficiency is relatively high. The use of the mesh for MSH3 and MSH4 has substantially reduced the mean of δv_a and the standard deviation of δv_a from the corresponding values associated with the use of the mesh for MSH2. The use of the mesh for MSH5 has produced a mean value and standard deviation of δu_w close to those associated with the use of the mesh for MSH4, and has slightly improved the standard deviation of δv_a. The mesh used for MSH1 is preferable because it gives better performance and the highest efficiency of computation. This domain will be used for subsequent runs.

4.4.5 Influence of outlet condition on prediction accuracy

The water tank [Figure 4.1(b)] has a free water surface on the top. This top boundary is treated as an outlet of the model domain [Figure 4.2(a), the line $\overline{BC}$]. Three simulations were carried out where different kinds of conditions at the boundary were imposed. The three kinds of conditions are:

(1) Pressure outlet. This means that the pressure at the outlet is set to the standard atmospheric pressure. This is a physically realistic situation at a free surface. However, with this boundary condition, water can possibly leave the domain. For an incompressible flow, water should not leave the domain to ensure mass conservation.

(2) De-gassing. In degassing boundary condition, the dispersed fluid phase (or air bubbles) see this boundary as an outlet. The continuous phase (or water) sees this boundary as a free-slip wall. Thus, air bubbles are allowed to escape, but water does not leave the domain. There is no need to include a freeboard region in the model domain of interest.

(3) A layer of air above the water surface. The model domain includes a 5-cm freeboard region of air on top of liquid water. In this region, air motions were computed using another set of transport equations. At the top of the air layer, pressure outflow condition was imposed.

The setup and other conditions used for the three simulations were as follows: The model domain was domain A [Figure 4.2(a)]; the time step was 0.001 *s*; the turbulence closure model was the standard k-ε; the bubble size was 3 mm; the initial air velocity was 0.085 m/s; the mesh size was 5 mm with inflation.

The statistics of percentage errors [Equation (4.1)] for the three simulations are presented in Table 4.4. It appears that the inclusion of a layer of air above the water surface gives the lowest mean of

δv_a but the largest mean of δu_w among the three kinds of conditions. Moreover, the efficiency of computation is the lowest because another set of transport equations need to be solved for air motions. Using the pressure outlet condition improves δu_w from that associated with the inclusion of an air layer. The percentage errors δv_a have more or less the same mean value and standard deviation. Using the de-gassing condition produces δu_w with essentially the same mean and standard deviation as using the pressure outlet condition, but gives δv_a with somewhat a larger mean value. The percentage errors $\delta \alpha_a$ are at acceptable levels for any of the three boundary conditions. In summary, the de-gassing condition is preferable, as it realistically allows air bubbles to escape, but not water.

Table 4.4 Percentage errors in predicted air velocity, water velocity and air volume fraction for three simulations using different outlet conditions. The model time was t = 20 s. The mean value and standard deviation errors are determined using the data at z/H = 0.25, 0.50, and 0.75.

Simulation ID	Outlet condition	Mean value ± standard deviation of percentage errors		
		δv_a	δu_w	$\delta \alpha_a$
BC1	Pressure outlet	-12.1% ± 6.3%	-69.1% ± 8.5%	0.3% ± 0.2%
BC2	De-gassing	-12.7% ± 5.6%	-64.6% ± 8.4%	0.3% ± 0.2%
BC3	A layer of air above the water surface	-3.7% ± 8.8%	-75.7% ± 6.8%	0.0% ± 0.1%

4.4.6 The influence of time step on prediction accuracy

The choice of a proper time step should achieve both numerical stability and minimal truncation-error. For single phase flow, one may estimate the maximum allowable time step, Δt_{max}, using the Courant–Friedrichs–Lewy criterion $\left(\Delta t_{\max} \le \Delta x / \bar{v}\right)$ as a constraint due to advection, where Δx is the mesh size, and $\bar{v}$ is the velocity scale. If the velocity scale is taken as the initial velocity of air

bubbles and the mesh size used is $\Delta x = 5\,\text{mm}$, one will obtain $\Delta t_{\max} \le 0.6\,\text{s}$. Using time steps somewhat larger than this estimate, simulations of single phase flow can still be numerically stable.

However, it is uncertain to theoretically estimate Δt_{max} for two-phase flow, which is dealt with in this paper. As practical strategies, we carried out a series of simulations using increasingly smaller time steps and examined to what extent they improved predictions, when compared to measurements. These simulations used the same conditions as listed below: (1) The turbulence closure model used was the standard k-ε; (2) at the outlet, degassing was used as a boundary condition; (3) the bubble size was 3 mm; (4) the initial air velocity was 0.085 m/s; (5) the mesh size was 5 mm with inflation; (6) the model domain used as domain A [Figure 4.2(a)].

In Table 4.5, we show the percentage errors in predicted air velocity, water velocity and air volume fraction [Equation (4.1)], as an example, for two simulations using different time steps $\Delta t = 0.1\,s$ and $\Delta t = 0.001\,s$. There are no significant differences between the results. This indicates that a further refinement of time step from $\Delta t = 0.001\,s$ is not necessary. Accordingly, subsequent simulations will use $\Delta t = 0.001\,s$.

Table 4.5 Percentage errors in predicted air velocity (v_a), water velocity (u_w) and air volume fraction (α_a) for two simulations using different time steps. The mean value and standard deviation errors are determined using the data at z/H = 0.25, 0.50, and 0.75.

Simulation ID (Table 1)	Time step (s)	Mean value ± standard deviation of percentage errors		
		δv_a	δu_w	$\delta \alpha_a$
TA1	0.1	-10.9% ± 8.4%	-77.0% ± 11.8%	0.1% ± 0.1%
TA2	0.001	-11.0% ± 8.2%	-77.0% ± 12.6%	0.1% ± 0.1%

4.4.7 Choice of turbulence closure models

This section compares the statistics of percentage errors (Equation 4.1) between five simulations that use different models for turbulence closure. The models include four two-equation eddy viscosity models (the standard k-ε model, the RNG k-ε model, the realizable k-ε model, and the SST k-ω model) and one stress-transport model (RSM). Some details about these models have been given in Section 3.3, in Chapter 3.

The five simulations used same conditions and setup. The model domain used was domain A. The time step was 0.001 *s*. At the outlet, de-gassing condition was used. The bubble size was 0.003 mm. The initial air velocity was 0.085 m/s. The mesh size was 5 mm with inflation. The statistics of the percentage errors are presented in Table 4.6.

Table 4.6 Percentage errors in predicted air velocity, water velocity and air volume fraction for five simulations using different turbulence models. The mean value and standard deviation errors are determined using the data at z/H = 0.25, 0.50, and 0.75.

Model ID	Turbulence model	Mean value ± standard deviation of percentage errors		
		δv_a	δu_w	$\delta \alpha_a$
TC1	Standard k-ε	-11.0% ± 8.2%	-77.0% ± 12.6%	0.1% ± 0.1%
TC3	RNG k-ε	-8.9% ± 6.7%	-18.8% ± 48.2%	0.1% ± 0.1%
TC5	Realisable k-ε	-11.2% ± 6.7%	-87.4% ± 15.2%	0.2% ± 0.1%
TC2	SST k-ω	-7.8% ± 8.7%	-74.3% ± 12.3%	0.1% ± 0.1%
TC4	RSM	-5.6% ± 9.5%	-68.9% ± 7.2%	0.0% ± 0.1%

The standard k-ε model appears to perform better than the RNG k-ε model and the Realisable k-ε model. With the RNG k-ε model, the percentage errors in water velocity predictions have a high standard deviation. The SST k-ε model slightly improves air velocity predictions, in comparison to those from the standard k-ε model. RSM performs the best among all the models. It is worth

noting that relatively speaking, the standard *k-ε* model is conceptually less complicated and is seen to produce relevant results.

4.5 Influence of air bubble diameter

In this section, four different air-bubble diameters (d_b = 0.5, 1, 3, and 4 mm) are used to investigate the effect of bubble diameter on prediction of flow pattern, air volume fraction distribution, vertical water velocity, and vertical air velocity at model time t = 20 s. The model runs for air bubble diameter of 3, 4, 1, and 0.5 mm are denoted by B1, B2, B4, and B3, respectively. In these four runs, the initial air velocity is equal to 0.085 m/s. The time step was 0.001 s. The turbulence closure model was the standard k-ε. At the outlet, degassing was a boundary condition. The model domain used as domain A [Figure 4.2(a)].

Table 4.7 Summary of bubble diameter (d_b) used in four model runs.

Model run	Turbulence closure	Domain treatment	Solution method	Time step (s)	Bubble diameter (mm)
B1	k-ε	A	Eulerian	0.001	3
B2	k-ε	A	Eulerian	0.001	4
B3	k-ε	A	Eulerian	0.001	1
B4	k-ε	A	Eulerian	0.001	0.5

Figure 4.7 compares the air volume fraction for four different bubble diameters with initial air velocity of 0.085 m/s inside the column. The results are plotted at five selected heights (z/H = 0.0625, 0.125 0.25, 0.75, and 0.95, where H = 0.4 m) above the bottom, varying with radial distance, r/d_p, from the centre. The diameter of air bubbles injected is d_b = 0.5 mm for Run B4, d_b = 1 mm for Run B3, d_b = 3 mm for Run B1, d_b = 4 mm for Run B2 (Table 4.7). At the same gas

flow rate (=0.0002 m^3/s), the peak values are larger for smaller air bubbles (d_b = 0.5 mm) than larger air bubbles (d_b = 4 mm).

Distributions of the vertical water velocity with radial distance from the centreline for four different bubble diameters is illustrated in Figures 4.8 (a)-(e). The water velocity curves for 4-mm bubbles are plotted mostly below those for 1-mm bubbles in the vicinity of the lake centre [r/d_p < 0.5, Figures 4.8 (a)-(e)]. In other words, the injection of air bubbles of a smaller diameter (d_b = 0.5 mm) appears to generate stronger upward water flow than air bubbles of a larger diameter (d_b = 4 mm). The stronger upward flow causes stronger downward flow of water around r/d_p =1, which leads to large scale motions in the lake. This has implications for inlet spacing in the design of aeration systems.

Distributions of vertical air velocity for four different bubble diameters are presented in Figures 4.9 (a)-(e). The results show that the rising velocities are higher for air bubbles of larger diameter (d_b = 4 mm) than air bubbles of smaller diameter (d_b= 0.5 mm). This can be explained by the fact that larger air bubbles rise in the lake water under stronger buoyance force than smaller air bubbles. This means that the smaller air bubble would rise slower and remain longer in the water.

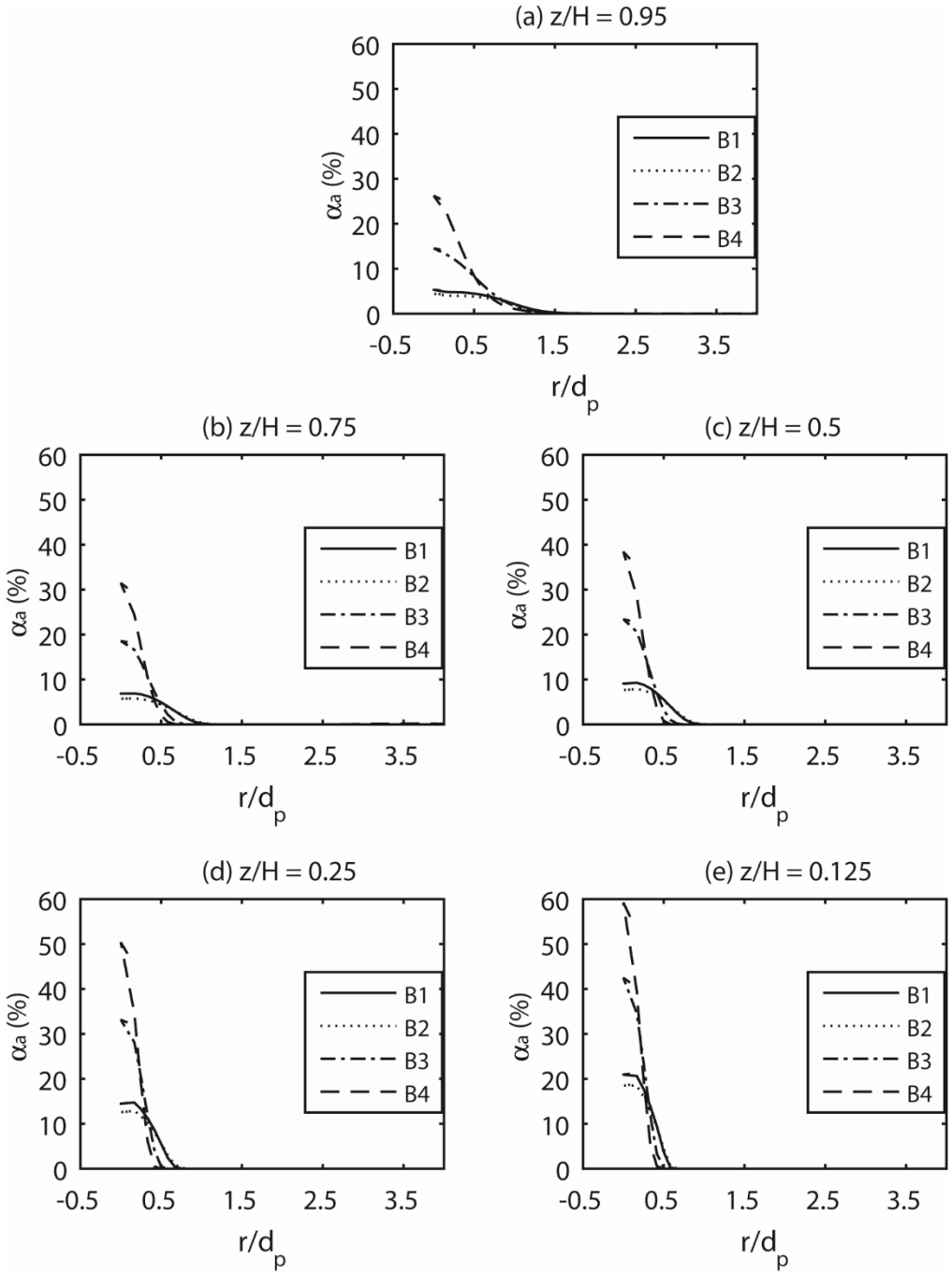

Figure 4.7 Distribution of air volume fraction, α_a, with radial distance, r/d_p, from the centre of the cylinder, using four different bubble diameters. The distance has been normalised by the pipe diameter, d_p (equal to 0.06 m) (see Table 4.7).

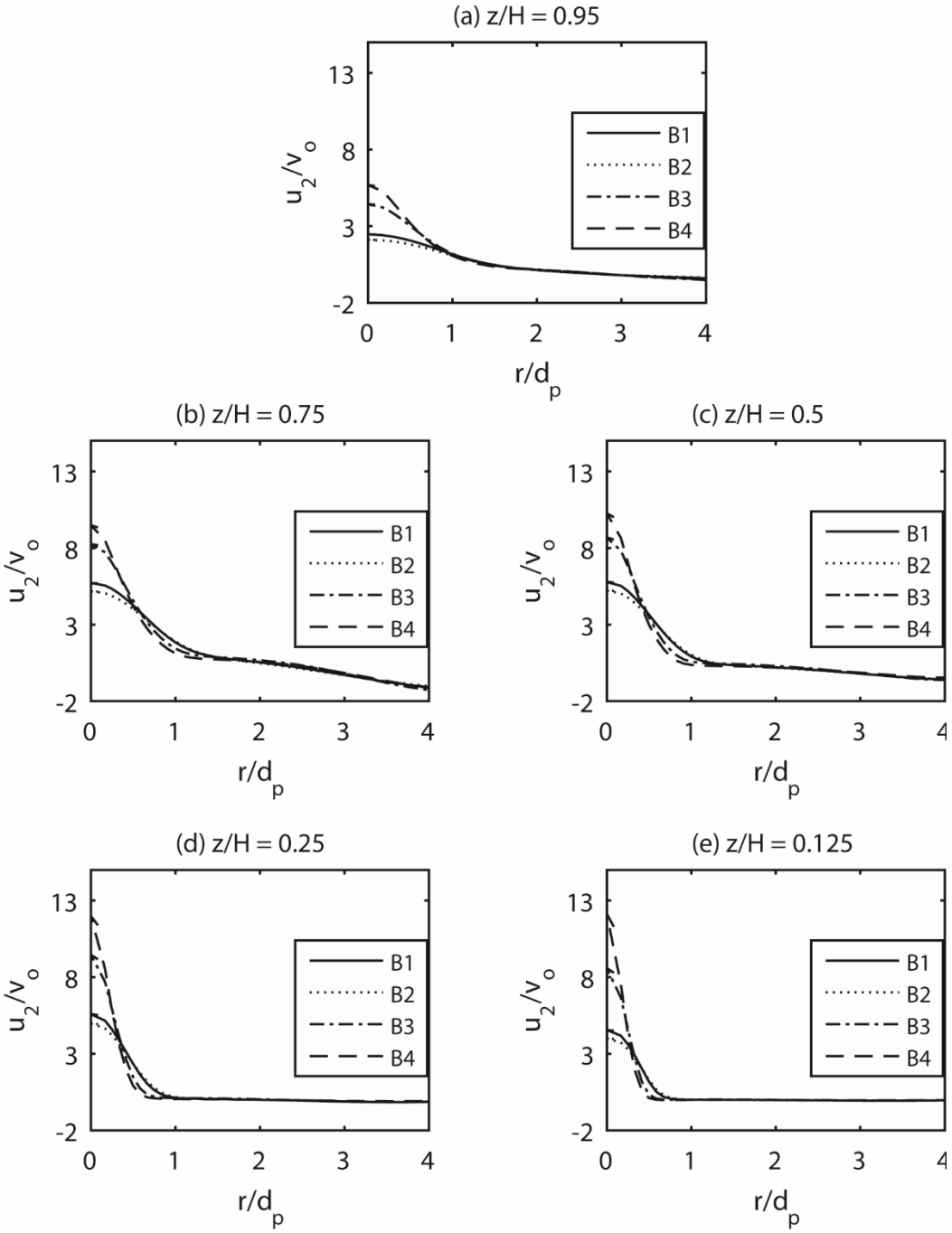

Figure 4.8 Distributions of vertical water velocity, u_2, with normalised radial distance, r/d_p, from the centre of the lake. The velocity component has been normalised by the initial velocity of air bubbles, v_o (equal to 0.085 m/s). The distance has been normalised by the initial velocity of air bubbles, v_o (= 0.085 m/s). The distance has been normalised by the pipe diameter, d_p (equal to 0.06 m) (see Table 4.7).

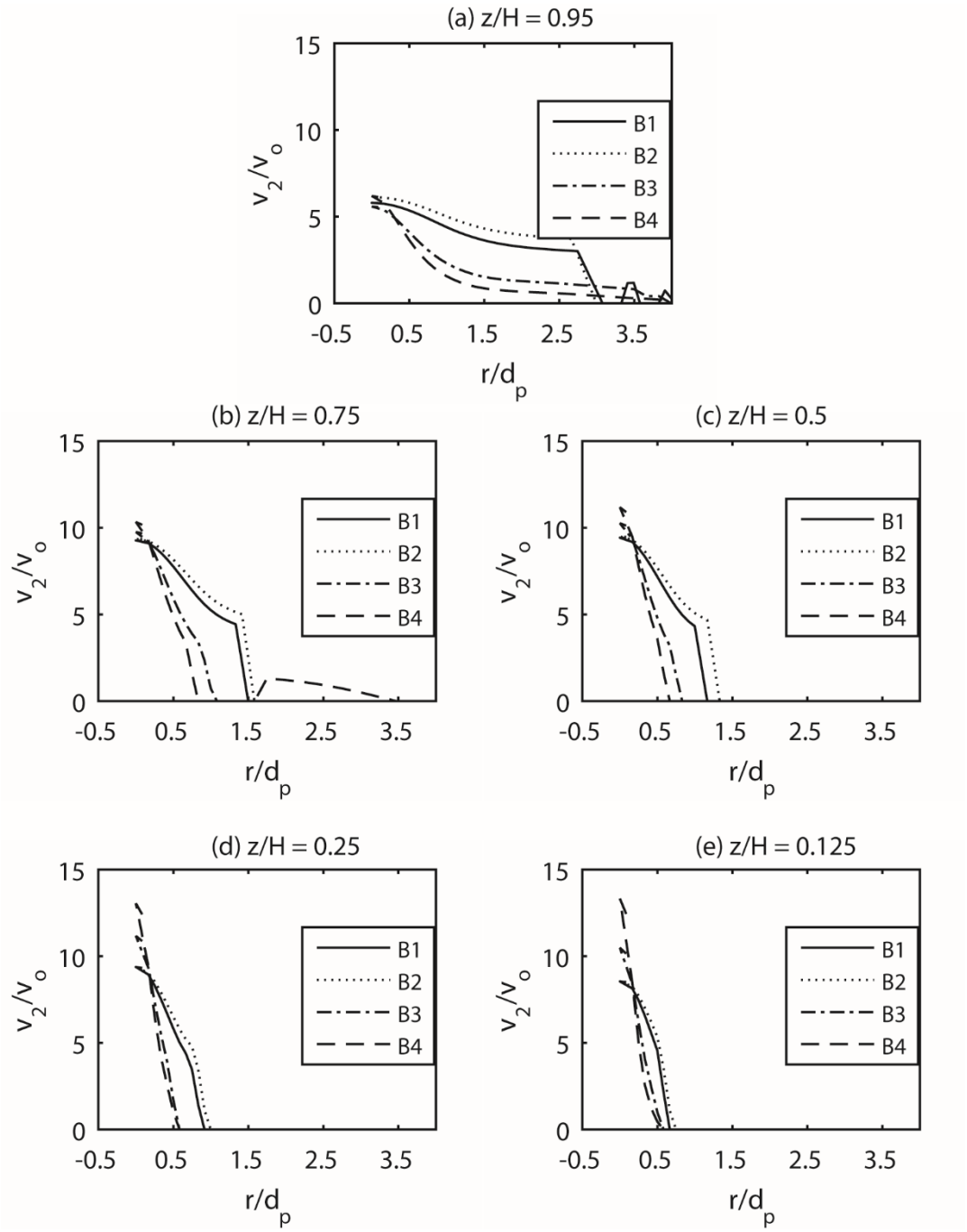

Figure 4.9 Vertical distribution of bubble rising velocity, v_2, with normalised radial distance, r/d_p, from the centre of the lake. The velocity component has been normalised by the initial velocity of air bubbles, v_o (equal to 0.085 m/s). The distance has been normalized by the pipe diameter, d_p (equal to 0.06 m) (see Table 4.7).

The effect of air-bubble diameter on the air volume fraction in model domain A is depicted in Figures 4.10 (a)-(d). In the four runs, the gas occupies approximately the same area and a bubble plume developed at the centre of the model domain in each run. In runs B1 and B2, bubbles tend to spread more to the wall regions while runs B3 and B4 show a higher amount of air along the centreline than the other two runs B1 and B2. This shows longer residence of the smaller air bubbles along the column.

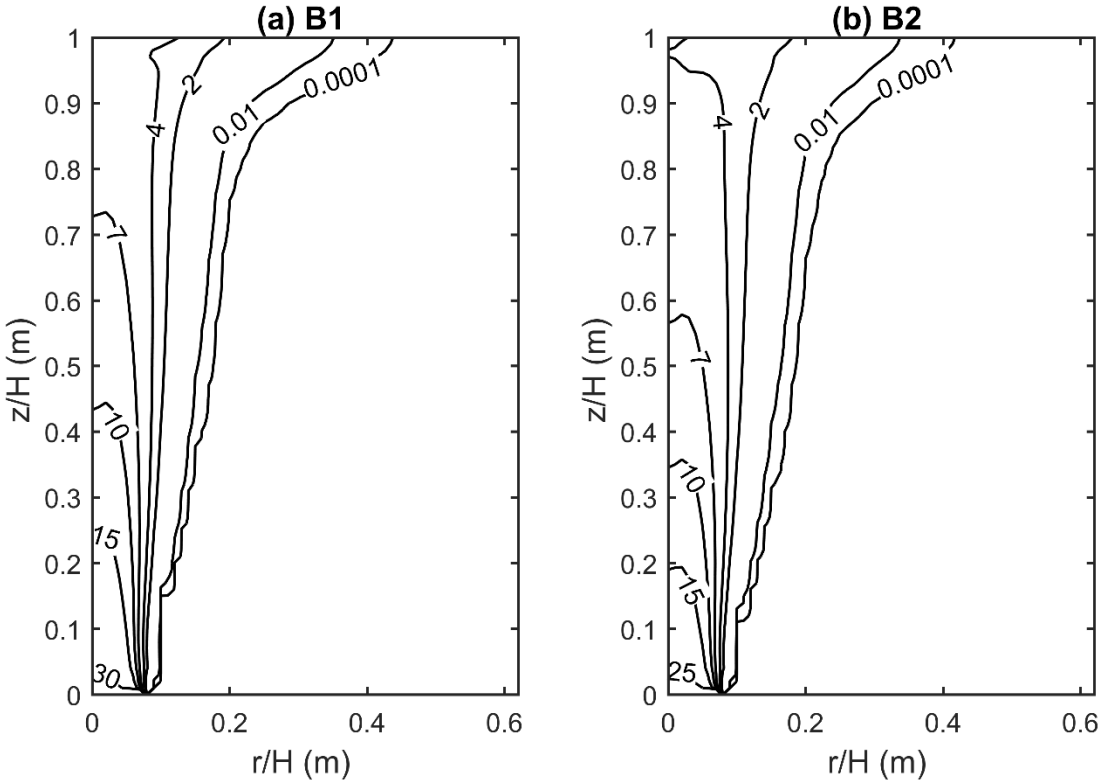

Figure 4.10 Contours of air volume fraction (α_a in per cent) for four model runs: (a) B1, 3-mm bubbles; (b) B2, 4-mm bubbles; (c) B3, 1-mm bubbles; (d) B4, 0.5-mm bubbles (see Table 4.7).

Figure 4.10 (Continued).

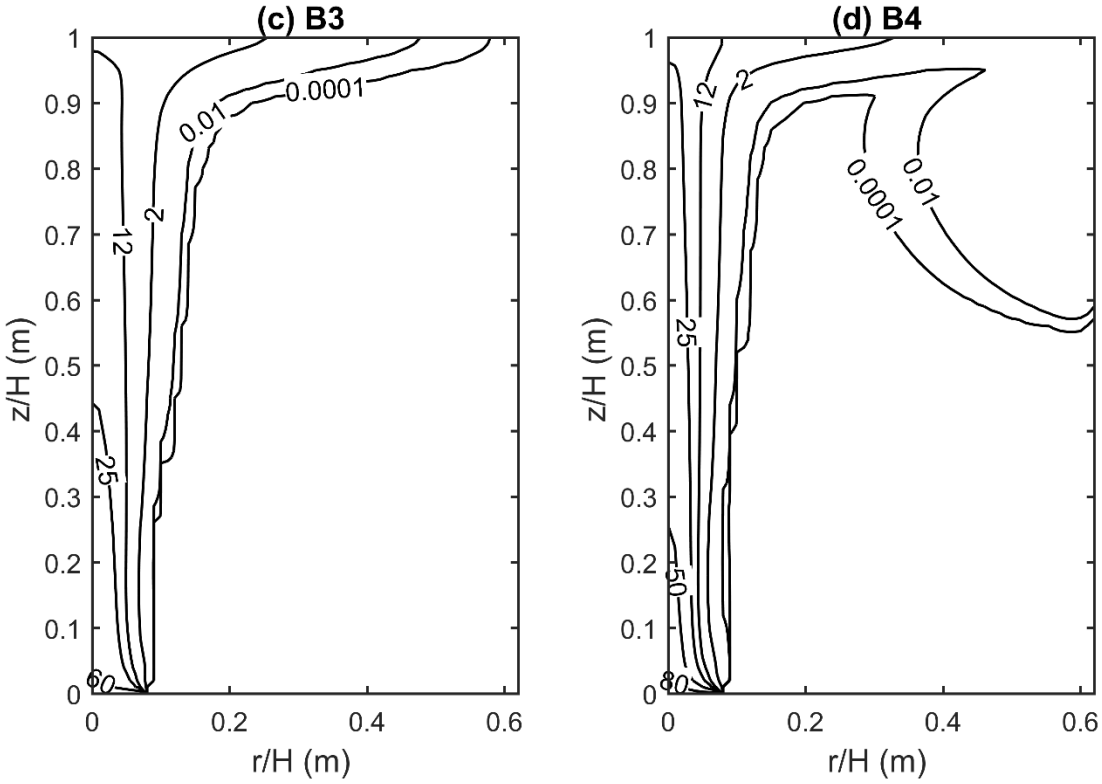

4.6 Influence of port diameter

In this section, the effect of inlet (injector) diameters on the flow pattern and gas dynamics are examined. Results are predicted with Eulerian method and extracted for runs PO1 and PO2 (Tables 4.1 and 4.8) at model time $t = 10.7\ s$ for five selected heights from the bottom of the domain: z/H = 0.125, 0.25, 0.5, 0.75, and 0.95, where H = 0.4 m. The diameter of air bubbles injected is d_b = 3 mm. In two runs PO1 and PO2 all the simulation condition are kept the same while the inlet diameter in run PO1 is equal to 0.06 m and in run PO2 is equal to 0.1m. The bubbles are injected to the water with initial upward velocity of 0.085 m/s.

Table 4.8 Summary of inlet (injector) diameter (d_p) used in two model runs.

Model run	Turbulence closure	Domain treatment	Solution method	Time step (s)	Bubble diameter (mm)	Port diameter (m)
PO1	SST k-ω	A	Eulerian	0.001	3	0.06
PO2	SST k-ω	A	Eulerian	0.001	3	0.1

Figures 4.11 (a)-(e) demonstrates the distribution of water turbulent kinetic against normalised radial distance from the centre of the model domain. The curves for run PO2 bubbles are plotted mostly above those for run PO1. This means that the injector with a larger diameter produces higher turbulent kinetic energy than the injector with a smaller diameter. The larger injector in diameter provides higher turbulent kinetic energy due to providing higher upward and downward water velocity and higher air volume fraction in the model domain.

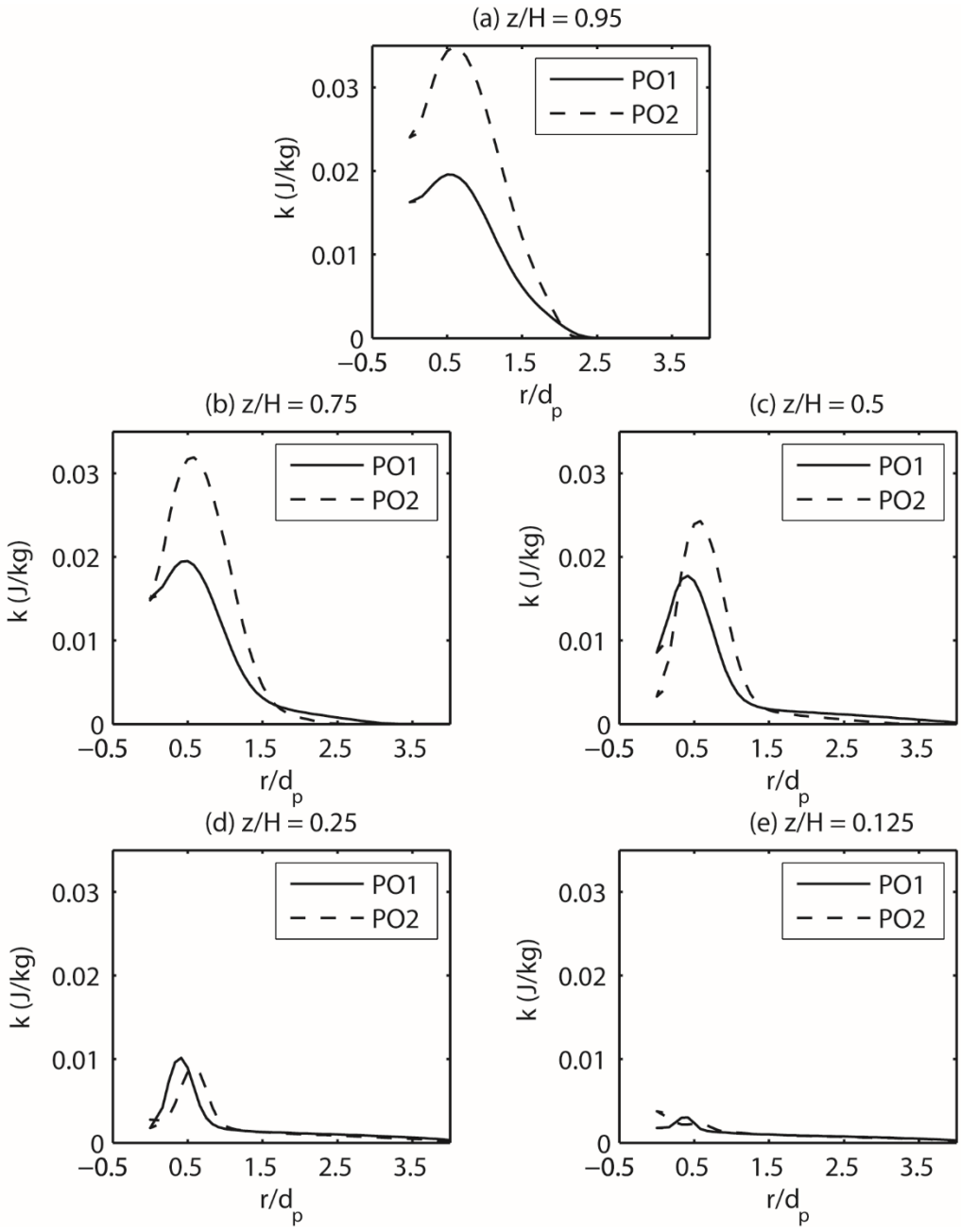

Figure 4.11 Comparison of turbulence kinetic energy (k) between two model runs (PO1 and PO2, Table 4.8) using different values for the port diameter (d_p). For PO1, d_p = 0.06 m, and for PO2, d_p = 0.1 m. The horizontal axis displays the radial distance from the centre of the model cylinder [Figure 4.2(a)], normalised by the pipe diameter for PO1.

In Figures 4.12 (a)-(e), the distributions of the vertical component of water velocity with normalised radial distance, r/d_p, are plotted for runs PO1 and PO2. The figures illustrate that model run PO2 can produces a higher upward velocity around the centre and higher downward velocity close to the walls. The higher water velocity produces the larger water fluctuating component that results in bigger values for turbulent kinetic energy in the model domain.

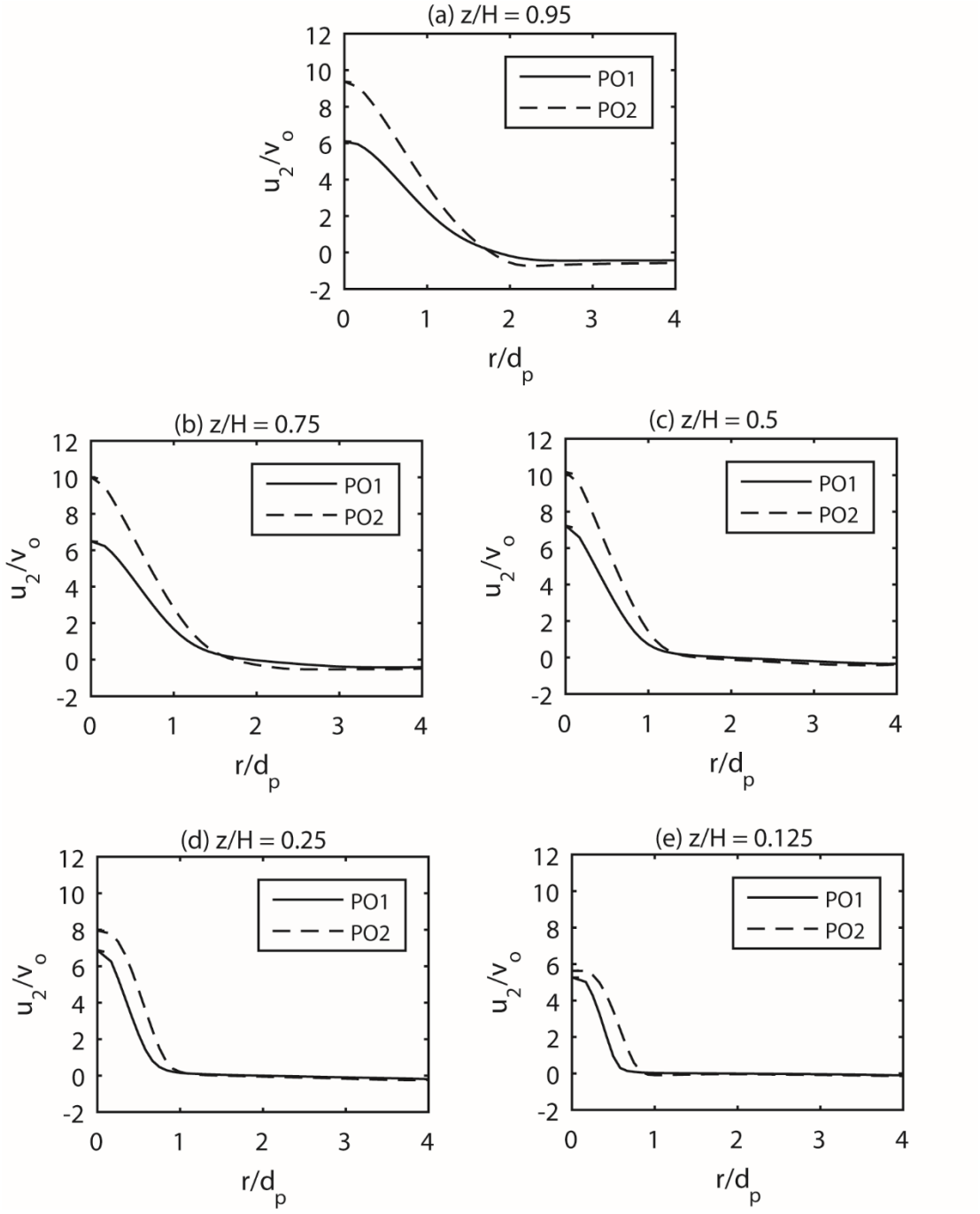

Figure 4.12 Comparison of the z-direction water velocity (u_2) between two model runs (PO1 and PO2, Table 4.8) using different values for the port diameter (d_p). For PO1, d_p = 0.06 m, and for PO2, d_p = 0.1 m. The horizontal axis displays the radial distance from the centre of the model cylinder [Figure 4.2(a)], normalised by the pipe diameter for PO1.

Figures 4.13 (a)-(e) and Figures 4.14 (a)-(e) indicate the influence of inlet diameter on the air volume fraction and vertical component of air bubble velocity, respectively. The predicted air velocity and air volume fraction by the model run with a smaller inlet (PO1) is smaller than the predicted results by run PO2. This is valid for all five heights above the bottom of the model domain. High liquid velocities are formed in the high void fraction regions due to strong updraft induced by bubbles. Figures 4.11 to 4.14 indicate that with a larger inlet the profiles are wider. It indicates that a larger inlet/injector/diffuser affects a larger area of the liquid phase, leading to a more uniform velocity distribution and turbulent energy distribution in the water region above the inlet.

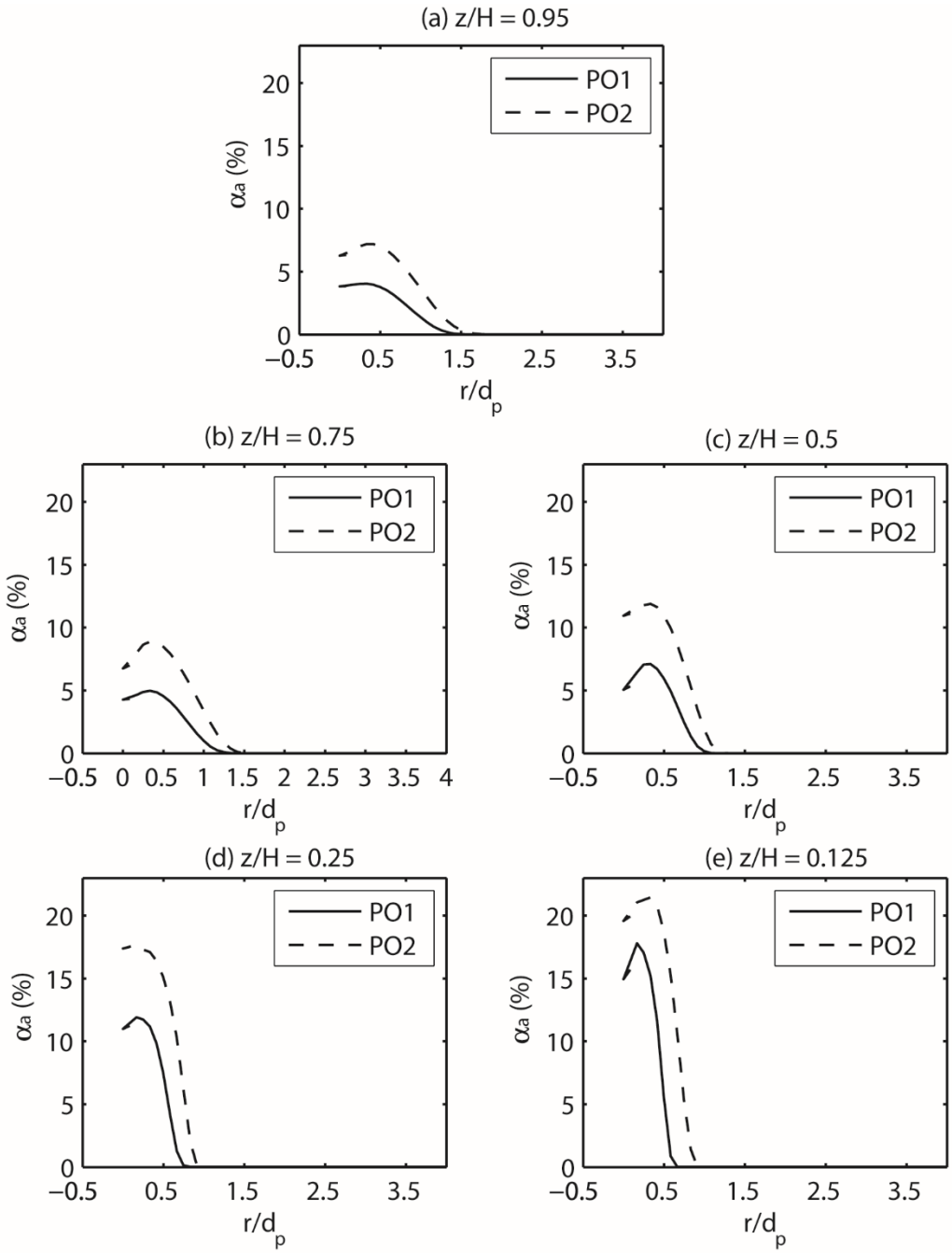

Figure 4.13 Comparison of air volume fraction (α_a) between two model runs (PO1 and PO2, Table 4.8) using different values for the port diameter (d_p). For PO1, d_p = 0.06 m, and for PO2, d_p = 0.1 m. The horizontal axis displays the radial distance from the centre of the model cylinder [Figure 4.2(a)], normalised by the pipe diameter for PO1.

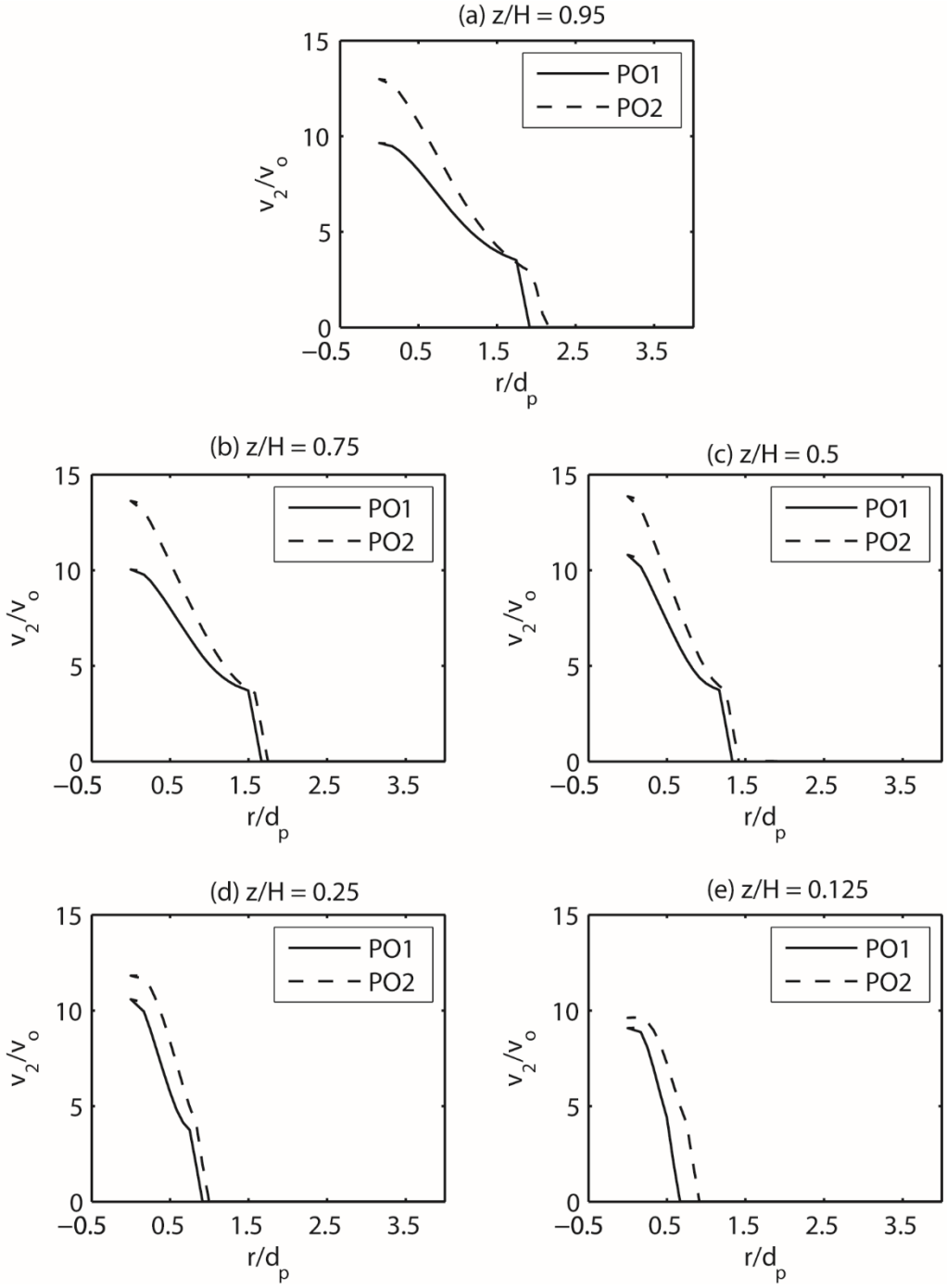

Figure 4.14 Comparison of the z-direction air velocity (v_2) between two model runs (PO1 and PO2, Table 4.8) using different values for the port diameter (d_p). For PO1, d_p = 0.06 m, and for PO2, d_p = 0.1 m. The horizontal axis displays the radial distance from the centre of the model cylinder [Figure 4.2(a)], normalised by the pipe diameter for PO1.

4.7 Oxygen mass transfer in bubbly flow

This section deals with calculations of the volumetric mass transfer coefficient (K_La) based on the equations provided by Gulliver (2007) and Schierholz et al. (2006). The calculations are carried out in the 2D axisymmetric cylindrical domain A [Figure 4.2(a)] for model run TA1 (Table 4.1).

The gas transfer process for a bubble column or a lake can be broken into the two parts: (1) oxygen absorption from the air bubbles; and (2) oxygen absorption at the water surface. In a completely mixed body of "clean water", the total change in DO concentration caused by aeration is often expressed as (Gulliver, 2007):

$$V\frac{dC}{dt} = K_L A_b\left(C^* - C\right) + K_{LS} A_S (C_s - C) \tag{4.2}$$

where V is the volume of the water body (m^3); K_L is the liquid film coefficient (m/s); K_{LS} is the liquid film coefficient of the water exposed to the atmosphere (m/s); C is the water side concentration (mg/L); C^* is the concentration of the water in equilibrium with the bubble (mg/L); and C_s is the saturation concentration of water exposed to the atmosphere (mg/L).

Schierholz et al. (2006) suggested the following bubble-water transfer coefficients:

$$Sh = \frac{1}{6}\frac{We^{3/5} Sc^{1/2}\,\mathrm{Re}}{Fr} \qquad \text{Fine bubble diffusers} \tag{4.3}$$

$$Sh = \frac{1}{37}\frac{We^{3/5} Sc^{1/2}\,\mathrm{Re}}{Fr} \qquad \text{Coarse bubble diffusers} \tag{4.4}$$

where $Sh = K_L A_b h_d^2 / DV$; $We = u_s{}^2 h_d \rho / \sigma$; $Sc = \upsilon / D$; $\mathrm{Re} = u_s h_d / \upsilon$, and $Fr = v_s / \sqrt{g h_d}$ is the Froude number; h_d is the diffuser depth (m); V is the volume of the water body (m^3); and v_s is the superficial gas velocity (m/s); D is the diffusion coefficient of oxygen in water (m^2/s); Sc is Schmidt number(dimensionless). In a fine bubble diffuser, bubble diameter is less than 4 mm. Surface mass transfer depends on similar parameters such as bubble mass transfer, with the exception of the Froude and Weber numbers. Thus, the resulting water surface transfer coefficients were fit to the following equation:

$$Sh_s = 49 Sc^{1/2} \mathrm{Re} \left(\frac{A_{cs}}{h_d^2} \right)^{0.72} \tag{4.5}$$

where Sh_s is the Sherwood number for surface transfer, $Sh_s = K_L A_s / (h_d D)$; A_s is the surface area of the water body; A_{cs} cross-sectional tank area (m^2). The K_{LS} is linearly dependent on gas flow rate. The reason is that the bubbles passing through the surface create a significant free surface turbulent.

Table 4.9 Summary of model parameters. The water temperature is taken as 25° C. The turbulence closure model used is the *k-ε* model.

Parameter	Value
Surface tension σ (N/m)	0.073
Density of water ρ (kg/m^3)	998.2
kinematic viscosity υ (m^2/s)	10^{-6}
Air velocity at the inlet (m/s)	0.085
Water velocity at the inlet (m/s)	0
Total flow rate at inlet Q (m^3/s)	2×10^{-4}
Bubble size at the inlet d (mm)	3
Volume of the water body V (m^3)	0.078
Diffusion coefficient of oxygen in water D (m^2/s)	2×10^{-9}
Surface diameter of the cylinder (m)	0.5
Diffuser depth h_d (m)	0.4
Cross-sectional tank area A_{cs}(m)	0.196
Inlet diameter of the air pipe (m)	0.06

At T = 25°C, C^* = 8.05 mg/L, C_s = 8.24 mg/L, and C^*/C_s = 1.0. Thus, C^* can be replaced by C_{sat} in equation (4.2) and the equation can rewritten as below:

$$V\frac{dC}{dt} = K_L A_b (C_s - C) + K_{LS} A_S (C_s - C) \tag{4.6}$$

Dividing both sides of the equation by V

$$\frac{dC}{dt} = K_L a_b (C_s - C) + K_{LS} a_S (C_s - C) \tag{4.7}$$

where $K_L a_b$ is the volumetric bulk mass transfer coefficient for oxygen at the bubble surface (s^{-1}); $K_{Ls} a_s$ is the volumetric mass transfer coefficient for oxygen at the water surface (s^{-1}). The volumetric gas-liquid mass transfer coefficient is typically used when determining the mass transfer coefficient since it is difficult to measure K_L or a independently.

Integrating from an initial oxygen concentration C_o (at time $t = 0$) to a final oxygen concentration C_f (at a lapse time $t = t_f$) gives

$$\frac{C_s - C_f}{C_s - C_o} = e^{-t(K_L a_b + K_{LS} a_s)} \tag{4.8}$$

Thus, we have

$$C_f = C_s \left[1 - e^{-t(K_L a_b + K_{LS} a_s)}\right] \tag{4.9}$$

The calculation procedures for oxygen mass transfer are summarized as follows:

a. Calculate *Sh* using Equation (4.3) and find $K_L a_b$

b. Calculate Sh_s using Equation (4.5) and find $K_L a_s$.

c. Substitute $K_L a_b$ and $K_L a_s$ into Equation (4.9) and find oxygen concentration at different times.

Table 4.10 Calculated oxygen mass transfer coefficients using Equations (4.3), (4.5) and (4.9) at T = 25°C

t (s)	Sh (-)	Sh_s (-)	K_La_s (1/s)	K_La_b (1/s)	K_La_{s+} K_La_b (1/s)	C_f (mg/L)
0.2	245125	863085	0.0088	0.0031	0.0119	0.020
1	1214725	3275631	0.0334	0.0152	0.0485	0.390
2	1617463	4158390	0.0424	0.0202	0.0626	0.969
5	1330541	3533896	0.0360	0.0166	0.0526	1.906
10.7	699359	2067666	0.0211	0.0087	0.0298	2.250
20	711198	2096794	0.0214	0.0089	0.0302	3.740
100	580635	1770717	0.0180	0.0073	0.0253	7.583
200	580688	1770853	0.0180	0.0073	0.0253	8.188
300	580738	1770980	0.0180	0.0073	0.0253	8.236
400	593103	1802348	0.0184	0.0074	0.0258	8.240
500	588595	1790925	0.0182	0.0074	0.0256	8.240
1000	589897	1794224	0.0183	0.0074	0.0256	8.240
1500	580257	1769758	0.0180	0.0073	0.0253	8.240
2000	580247	1769733	0.0180	0.0073	0.0253	8.240

Figure 4.15 illustrates variations in the concentration of oxygen demand with time, in the cylinder. The initial upward velocity of the air bubbles is equal to 0.085 m/s. Calculated DO concentrations are showed continuously over time until the oxygen level in the water reaches the presumed steady-state DO value. Figure 4.15 shows that DO increases in time and reaches to a steady state at t = 300 s. Over time, the ambient water DO increases, the oxygen concentration changes little. The liquid phase (water) equilibrium oxygen concentration approaches the saturation value. Table 4.10 and Figure 4.15 demonstrate that injection of air bubbles to the water has increased the DO level in water effectively.

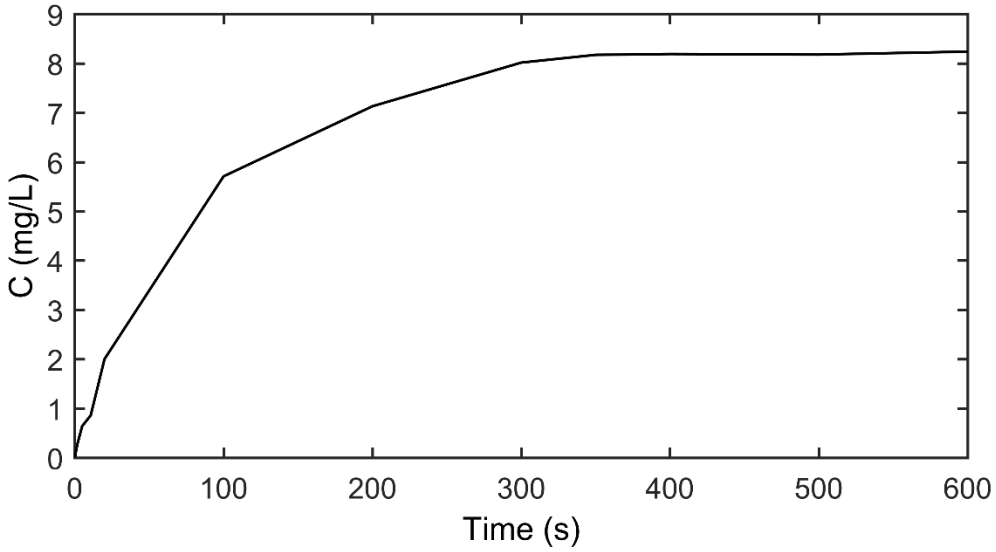

Figure 4.15 Time series of spatially averaged oxygen concentration (*C*) in the model cylinder [Figure 4.2(a)].

4.8 Discussion

The difference between degassing boundary condition (for Run BC2) and pressure outlet boundary condition (for run BC1) is indicated in Figure 4.16. The first noticeable difference of using degassing and pressure boundary condition is on flow pattern in the model domain. Water velocity vectors plotted for pressure outlet condition [Figure 4.16 (a)] demonstrates that water is leaving the domain, while this is fixed by using degassing condition [Figure 4.16(b)]. The use of degassing boundary condition predicted a bigger vortex than the use of pressure outlet boundary condition. The former produced numerical results in better agreement with observations than the latter. The results correspond to more realistic water circulation and renewal of water in the domain. Including freeboard region of air on top of the water (for run BC3) also produced nearly the same flow

patterns as degassing condition, although the computing time was longer than the degassing condition.

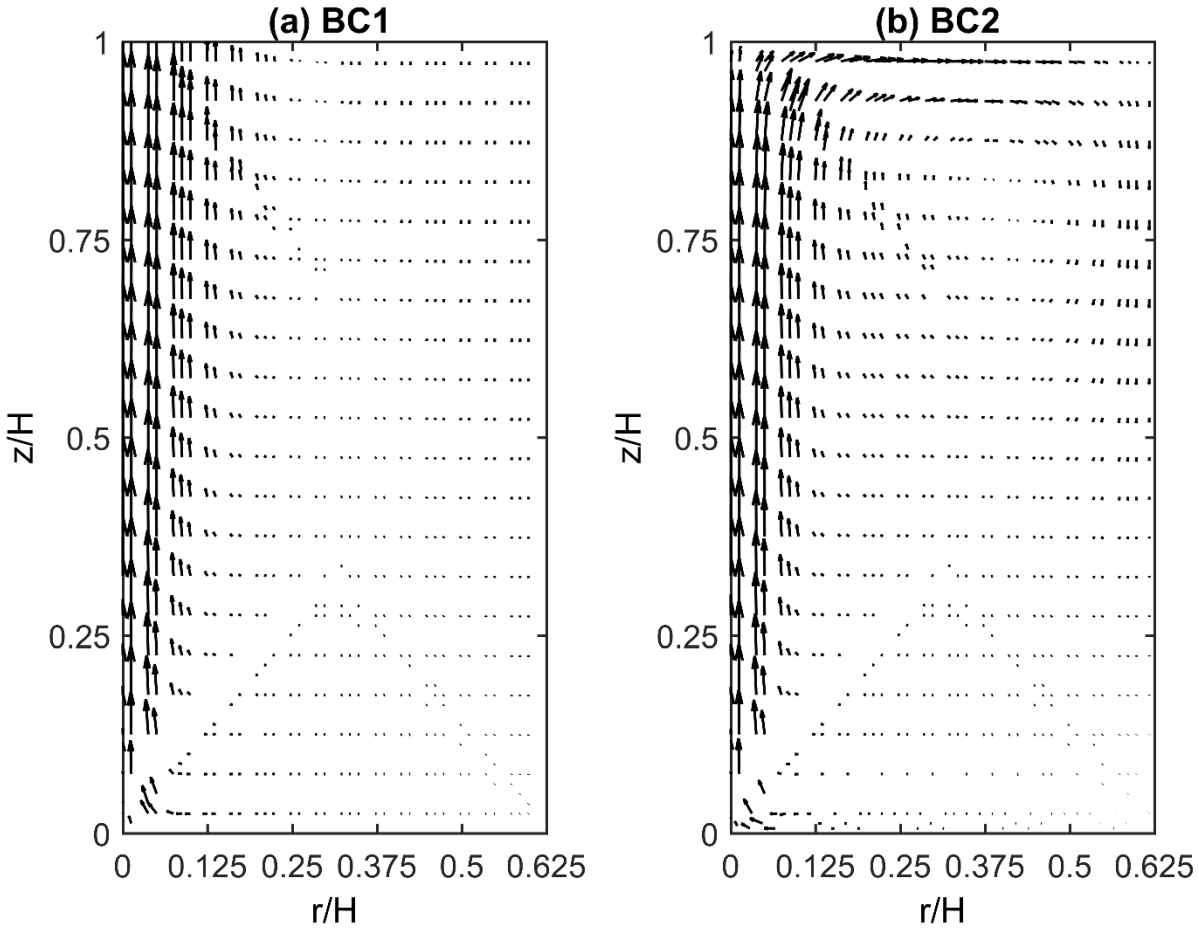

Figure 4.16 Comparison of water velocity vectors between two model runs (Table 4.1): (a) Run BC1 for which pressure outlet boundary condition was used; (b) Run BC2 for which degassing boundary condition was used. The velocity vectors were extracted from the model results at model time of t = 10.7 s.

It is clear that the use of a 3D simulation domain has produced more realistic results, in comparison to the use of a 2D domain. However, the computing costs of 3D simulations were much higher. It

would be constructive to carry out 2D axisymmetric simulations in order to obtain results in reasonable comparison with laboratory measurements.

The axisymmetrical mesh was more efficient in computing than the full width mesh because the former had lower node count. Also, the use of the former can be justified by the fact that the tank of cylindrical shape [Figure 4.1(a)] is actually symmetrical about its axis. Moreover, Anagbo and Brimacombe (1990) indicated that the experimental results were symmetrical about the axis of the plug.

Concerning the use of a full-width 2D domain, after 20 *s* from the beginning of the simulation, the plume was seen to develop asymmetrical patterns. The jet tended to migrate to the walls [Figure 4.17(a)]. The tendency can be removed by using degassing boundary condition at the outlet instead of the pressure outlet [Figure 4.17(b)]. In the literature, the bending of the plume toward the wall is called the Coanda effect, as illustrated in Figure 4.17(a) at model time $t = 30$ *s*. Note that the same run conditions were used to produce the results shown in Figure 4.17(a) and 4.17(b), except for the boundary condition at the outlet.

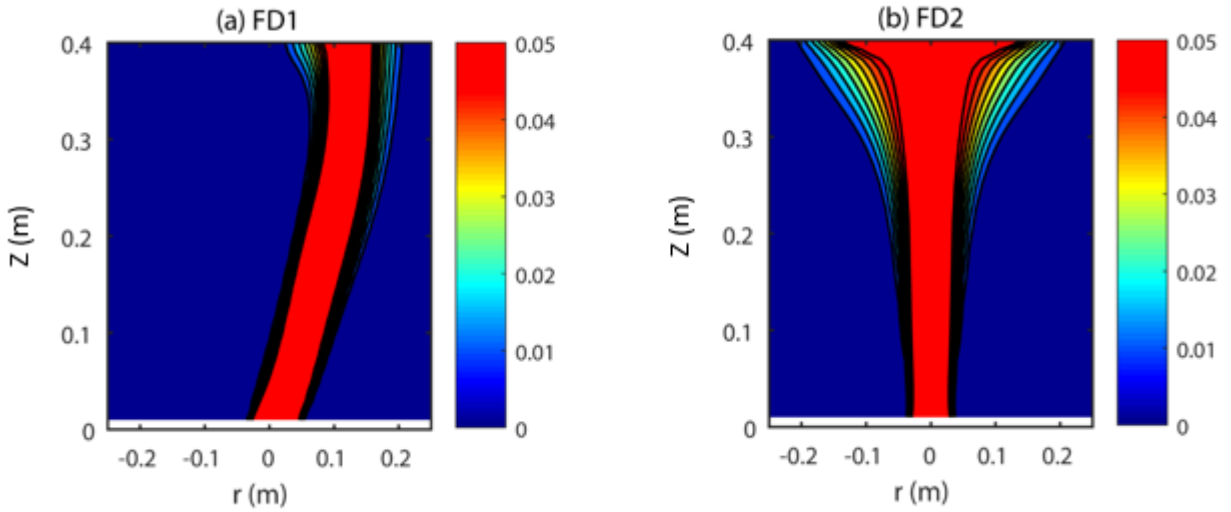

Figure 4.17 Air volume fraction: (a) pressure outlet boundary condition; (b) degassing boundary condition, at model time of t = 30 s.

The results with an axisymmetric domain are close to those for simulations with a 3D domain. Thus, a 2D axisymmetric computational domain is recommended. This is for two reasons: a) it offers high computational efficiency, relative to a 3D domain; and b) it appears to be sufficient to capture measured characteristics of air velocity, water velocity, and air volume fraction.

The use of the four turbulence closure models: SST k-ω, RNG k–ε, Realisable k–ε, and RSM, incurs more computing time than the standard k–ε turbulence model. The use of the standard k–ε turbulence model saves computing time by 35% or more in comparison to the other turbulence models.

Near the injector/diffuser, none of the turbulence models predicted the axial air velocity as reported experimentally. The predictive capability improved at higher axial locations, where the flow becomes developed. Along with the use of degassing condition, the k–ε turbulence model gave good results of air volume fraction and velocity profiles in the fully developed region, The RSM

model gave better results of gas holdup close to the injector. The RSM model is more successful to predict air- and water-velocity profiles than the other four models. The Realisable k–ε model gave the least accurate results.

All turbulence models were found to lead to stable and robust simulations. They all gave similar and acceptable predictions with respect to the air volume fraction.

The differences between predictions obtained by using the RSM model and standard the k–ε turbulence model in predicting air and water velocity are very small. Given that the standard k–ε model requires lower computing costs than the RSM model, the standard k–ε model is considered to be more suitable than the other four models.

4.9 Conclusions

This chapter discusses artificial circulation in a cylinder, induced by injecting air bubbles, for the control of eutrophication. We simulate artificial circulation using CFD modelling techniques, and reach the following conclusions: (1) The injection of air bubbles triggers turbulent motions of water and bubbles, which feature a strong upward flow above the injection location (Figure 4.3) and energetic turbulent eddies on both sides of the upward flow (Figure 4.3). (2) These large scale eddies enhance renewal of bottom water with oxygenated surface water, which helps improve the dissolved oxygen level in the lower water column. (3) Air bubbles entering the water column produce turbulent kinetic energy (Figure 4.11); this source of energy will maintain small scale eddy motions in the water, with beneficial mixing effects. (4) The dissolved oxygen level in the water is improved as a direct response to air bubbles entering the water column. (5) From the computational perspective, a 2D axisymmetric computational domain is recommended for two reasons: a) it offers high computational efficiency, relative to a 3D domain; and b) it appears to be

sufficient to capture measured characteristics of air and water velocities [Figures 4.6 (a)-(o)]. (6) Model predictions of water velocity, air velocity, air volume fraction agree well with experimental data, as shown in Figures 4.6(a)-(o).

5 Results of Artificial Flow in a Model Lake

This chapter presents results of the simulations for a model lake. A description of the simulation setup and conditions is given in this chapter.

A total of nine model runs were carried out using the Eulerian approach. These runs use the standard k-ε model for turbulence closure [Equations (3.22) and (3.23)]. The time period of all the simulations was t = 13 s. The diameter of the air bubbles is d_b = 3 mm. Control parameters and their values are listed in Table 5.1. Air bubbles introduced to the lake water have an initial upward velocity of 0.085 m/s.

Table 5.1 Summary of model run parameters and their values.

Parameter	Value
Time step Δt (s)	0.001
Grid spacing Δx, Δy (mm)	1 to 8.5
Air velocity at the inlet (m/s)	0.085
Water velocity at the inlet (m/s)	0
Total flow rate at inlet q (m^3/s)	2×10^{-4}
Bubble size at the inlet d_b (mm)	3
Air volume fraction at the inlet	1
Water volume fraction at the inlet	0
Convergence criteria	10^{-6}
Number of time steps N	13000
Simulation time period T (s)	13
Initial time (s)	0
Gravity g (m^2/s)	9.81
Air density ρ_a (kg/m^3)	1.225
Water density ρ_w (kg/m^3)	998.2
Surface diameter of the lake D_s (m)	20
Maximum depth of the lake (m)	2.0
Maximum depth of the water H (m)	2.0
Inlet diameter of the air pipe (m)	0.06
Turbulence closure model	k-ε

The four runs SP1, SP2, SP3 and SP4 vary in terms of port spacing (L) and the number of ports (N_p) in the model lake (Table 5.2). Also a comparative study has been conducted on five model runs with different choices of port elevation in the lake. The model runs and their elevations are listed in Table 5.3. All the eight runs produced finite volume solutions to the RANS equations. The results are presented and discussed in sections 5.5 and 5.6.

Fischer et al. (1979) reported that stratification in reservoirs depends on wind speed, inflow water temperature, and solar radiation intensity. Strong wind generates a large amount of kinetic energy within a reservoir which can lead to reservoir destratification. On the other hand, a strong stratification is developed for inflow water temperature much lower than the ambient temperature, weak wind speed, and intense solar radiation (Sahoo and Luketnia, 2006).Weak wind speed patterns denote low oxygen transfer rate at the atmosphere and water interface. Thus, the only way to prevent stratification and anoxia is that oxygen must be supplied by rising bubbles of an aeration system (Johnson et al., 2000; Sahoo and Luketnia, 2006; Yang et al., 1993). The influence of winds was neglected as this was not the focus of this study. Therefore, the following simulations consider the condition of no winds, and focus on the maximum potential effects of an aeration system on controlling the anoxic conditions and on stratification structure of lakes.

5.1 Model lake

Consider the problem of two-phase turbulent motion of water and air bubble as a mixture in the model lake (Figure 5.1). The motions are induced by injecting air bubbles into the middle of the lake at the bottom (Point O, Figure 5.1). Without losing generality, the lake is assumed to be symmetrical about the vertical line $\overline{OM}$ through the middle. This justifies the use of a two-dimensional vertical section through the middle (Section ABO, Figure 5.1) for computations of

flow velocities and turbulence quantities. Such a choice of two-dimensional computations is made to reduce computational costs.

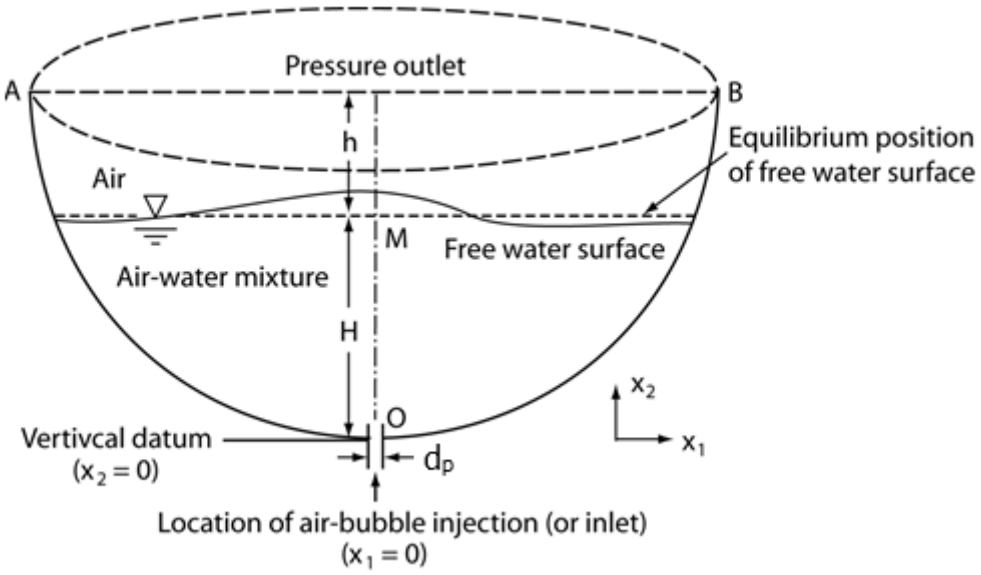

Figure 5.1 Diagram of the model lake, showing its axis-symmetrical geometry, the free water surface (in the x_1x_2-plane), and the location of air-bubble injection into the otherwise stagnant water. The vertical section ABO is chosen as the two-dimensional model domain for flow computations. The dimensions are as follows: $\overline{AB}$ = 20 m; H = 2 m; h = 0 m; d_p = 0.06 m.

5.2 Initial and boundary conditions

Initially (at time $t = 0$), the free water surface is located at the equilibrium position (Fig. 5.1). The volume fraction of water α_w below the surface is equal to one (for $x_2 \leq H$). Both water and air are stagnant or the velocity components u_1 and u_2 are set to zero in the entire model domain.

At the boundaries of the model domain (Fig. 5.2), appropriate kinematic and dynamic conditions are imposed. These boundaries include:

1) the inlet, through which air bubbles enter the lake water
2) the outlet (AB)

3) the solid walls (AOB)

The inlet has a width of d_p, and it's smaller (by a few order of magnitude) than the top width $\overline{AB}$ of the model domain (Figures 5.1 and 5.2). Through the inlet ($-d_p/2 < x_1 < d_p/2$ and $x_2 = 0$, Figure 5.1), air bubbles of given diameter d_b (smaller than d_p) enter the model domain continuously throughout the time period T of a simulation, at a pre-specified upward velocity u_o, i.e. $u_2 = u_o$ and $u_1 = 0$. At the inlet, the volume fraction of water α_w is taken as zero.

At the outlet (at $x_2 = H + h$ along the line $\overline{AB}$, Figures 5.1 and 5.2), the fluid is exposed to the atmosphere. Degassing boundary is used to allow bubbles to leave the domain.

At the solid walls (the curved lines between points B and O and between points A and O, Figure 5.2), no slip condition is applied, meaning that the fluid velocity tangential to the walls is set to zero. The fluid velocity normal to the walls is also zero.

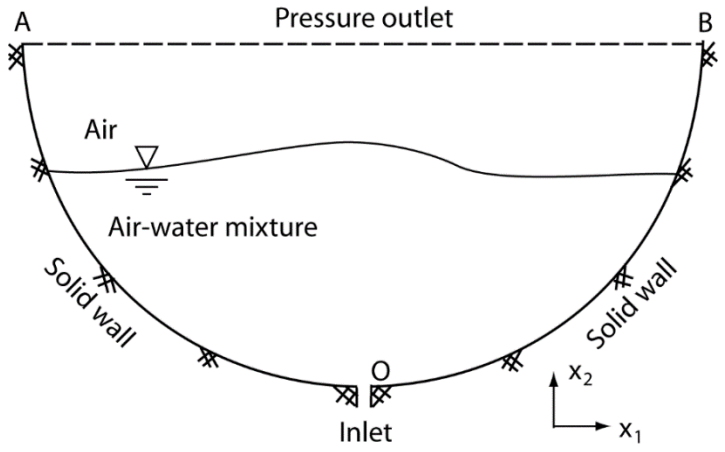

Figure 5.2 Model domain and boundaries. Air bubbles are forced to enter the model domain through the inlet. They cause fluid motions in the model lake.

5.3 Computational mesh

Quadrilateral mesh was created using ANSYS Workbench. The mesh contains 1025450 computational nodes. The cell sizes vary from 1 to 9 mm. The mesh allows fine resolutions for the central region around the line OM above the inlet (Figures 5.1 and 5.2), and less fine for regions further away from the central line. Such configuration is appropriate for resolving expected large spatial gradients of the flow field in the central region and at the same time for reducing computing costs.

5.4 Conditions of simulations

The model domain is a lake with a width of $\overline{AB} = 20$ m at the water surface, and a maximum depth of $H = 2$ m at the lake's centre (Figure 5.2). A circular pipe of $d_p = 0.06$ m in diameter, installed vertically around the centre of the lake bottom, allows air to enter the lake water with an initial vertical velocity of 0.085 m/s. The gas-liquid phases consist of water with a maximum depth of 2 m in the domain and air bubbles with a diameter of 3 mm. The air bubbles are injected to the lake from the bottom of the lake. The horizontal dimension of the model domain is so large that the sidewalls (solid walls, Figures 5.1 and 5.2) will not produce artificial effects on the lateral dispersion of air bubbles in the model lake. Model parameters and their values employed in simulations of air bubble dispersion are summarized in Table 5.1.

5.5 Port spacing and number of ports

In order to produce efficient circulation and vigorous turbulent mixing in the entire lake, more than one port are required. The aeration system is considered to be effective if it generates sufficient water circulation and mixing in a lake. The spacing between adjacent air inlets should be practical and economical. Four simulations were performed (runs SP1, SP2, SP3, and SP4). These model runs vary in terms of port spacing (L) and the number of ports (N_p) in the model lake (Table 5.2). These different simulations used the same conditions as listed below: (1) The turbulence closure model used was the standard k-ε [equations (3.22) and (3.23)]; (2) at the outlet, degassing was used as a boundary condition; (3) the bubble size was 3 mm; (4) the initial air velocity was 0.085 m/s; (5) the mesh size varies from 1 to 9 mm with inflation along the solid walls; (6) the 2D full width model domain was used (Figure 5.3); (7) Schiller-Naumann (Schiller and Naumann, 1935) drag force was considered as the only force for the interfacial force.

The computations using the 2D axisymmetric model domain were not successful in predicting water velocity in the central regions of the lake. For this reason, this modelling approach is not used in simulations of multiple ports/injectors. The 2D model domain is used in simulations containing more than one injector on the lake bottom, which has higher computational efficiency than the 3D domain.

Table 5.2 Summary of model runs with different port spacings and number of ports.

Model run	SP1	SP2	SP3	SP4
Port spacing , L (m)	0	1H	2H	1H
Number of ports, N_p	1	3	3	5

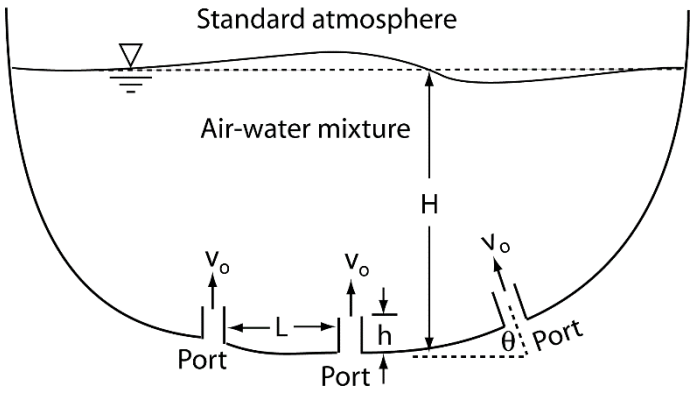

Figure 5.3 Sketch definition of a model lake, showing three ports at the bottom for air-bubble injection. *H* represents the maximum depth of water at equilibrium and *L* represents the distance between two adjacent ports.

The distribution of air volume fraction in the model lake at model time t = 13s for the four runs SP1, SP2, SP3 and SP4 are plotted in Figures 5.4(a)-(d). Air bubbles are seen to rise from the inlet (Figure 5.2) and reach the water surface [Figures 5.4(a) and 5.4(d)]. There are a significant amount of air bubbles along the centre of the lake and scattered around. This has important implications with respect to maintaining oxygenated water near the bottom.

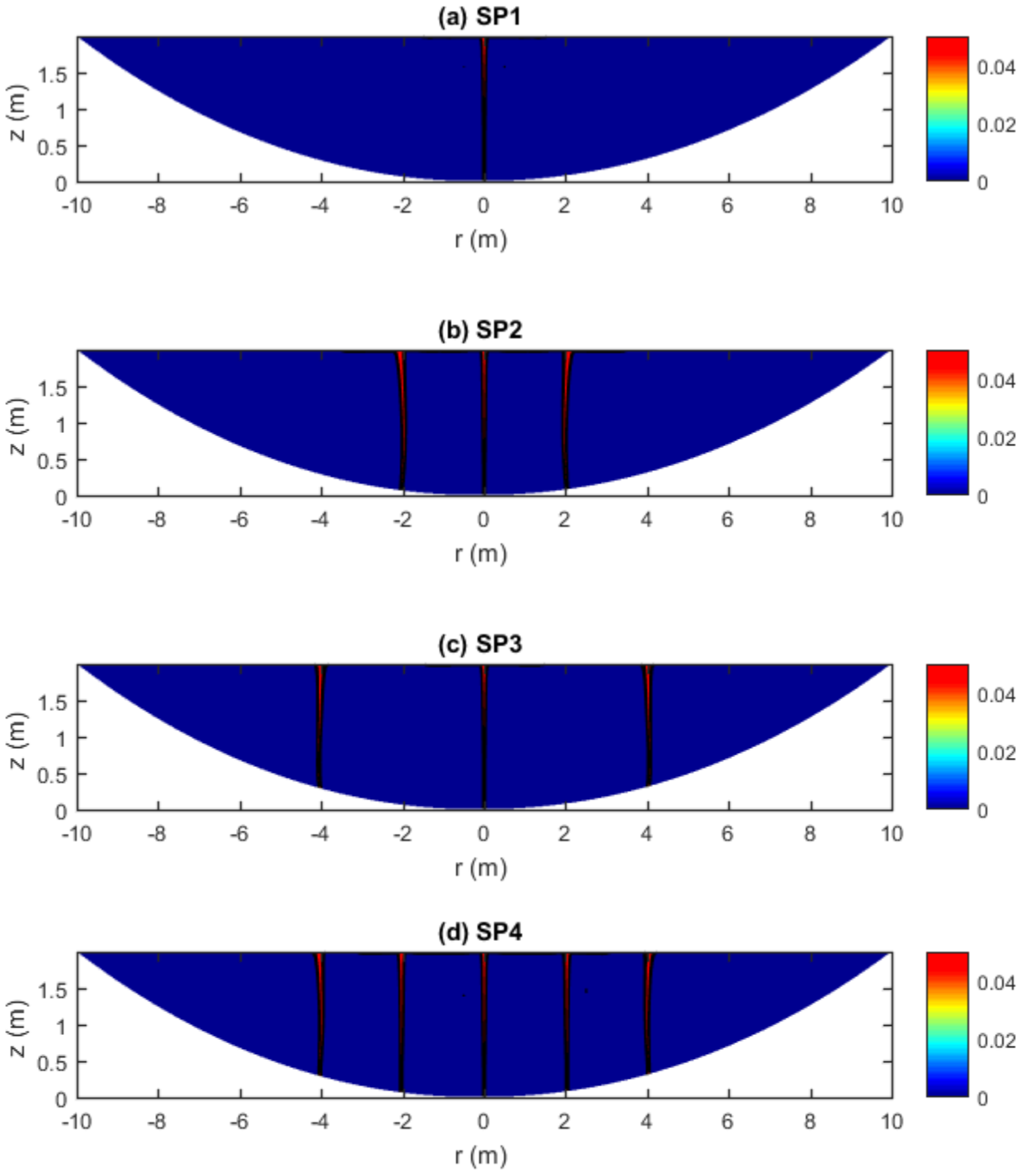

Figure 5.4 Distribution of air volume fraction for four model runs: (a) SP1; (b) SP2; (c) SP3; and (d) SP4. A value of zero means 100% of water and a value of one means 100% of air (see Table 5.2).

The distribution of water velocity in the model lake at model time t = 13 s for runs SP1, SP2, SP3, and SP4 are plotted in Figures 5.5(a)-(d). A comparison between run SP1 and the other three runs SP2, SP3, and SP4 illustrates the effects of employing single plume versus multiple plumes on flow patterns. The water velocity contours show the velocity of water in the model lake. Figure 5.5 (a) indicates that aeration affects the region between the injector and top surface. It also affects the region with a radius of 2.5 m from the centreline toward the shorelines in both directions. Thus, other regions with R> 2.5m (showed in dark blue color in Figure 5.5 (a)) belong to the dead zone, where water velocity is very small and close to zero. The dead zone region in run SP1 is much larger than the aerated zone. Therefore, in order to reduce the dead zone region and increase the aeration efficiency, it is required to employ more than one injectors in the lake. To generate strong motions in the water body, runs SP2, SP3, and SP4 were conducted to: (1) find the optimal distance between adjacent injectors; and (2) the optimal number of injectors. All four simulations are conducted with the same conditions and setup.

For run SP2, three inlets were employed. One port is located in the centre of the lake and the other two ports are located at equal horizontal distances from the central port, one on the left and the other one on the right. This horizontal distance (L) is equal to the maximum depth of the lake $L = H = 2$ m. For run SP3, similar to run SP2, three ports are used; however, the spacing between the ports is two times the maximum depth of the lake, $L = 2H = 4$ m. The water velocity contours for runs SP2 and SP3 are plotted in Figure 5.5 (b) and Figure 5.5 (c), respectively. A comparison between the two adjacent plumes for runs SP2 and SP3 illustrates that the region with low velocity is larger for run SP3 than SP2. In addition, the water velocity streamlines plotted in Figures 5.6(a)-5.6(d) demonstrate that run SP2 produces stronger downward flows compared to run SP3. Stronger downward flows for run SP2 is the result of the combined downward flows of the closer plumes.

A comparison of the three runs SP2, SP3, and SP4 with run SP1 indicates that employing more injectors reduces the dead zone region and increases the aerated area [Figures 5.5(a)-(d)].

Water velocity contours for run SP4 are plotted in Figure 5.5 (d). The distance between the injectors for this run is similar to SP2. However, for SP4, five injectors were employed along the lake domain. As expected, using five injectors in SP4 reduced the zone significantly, compared to SP2.

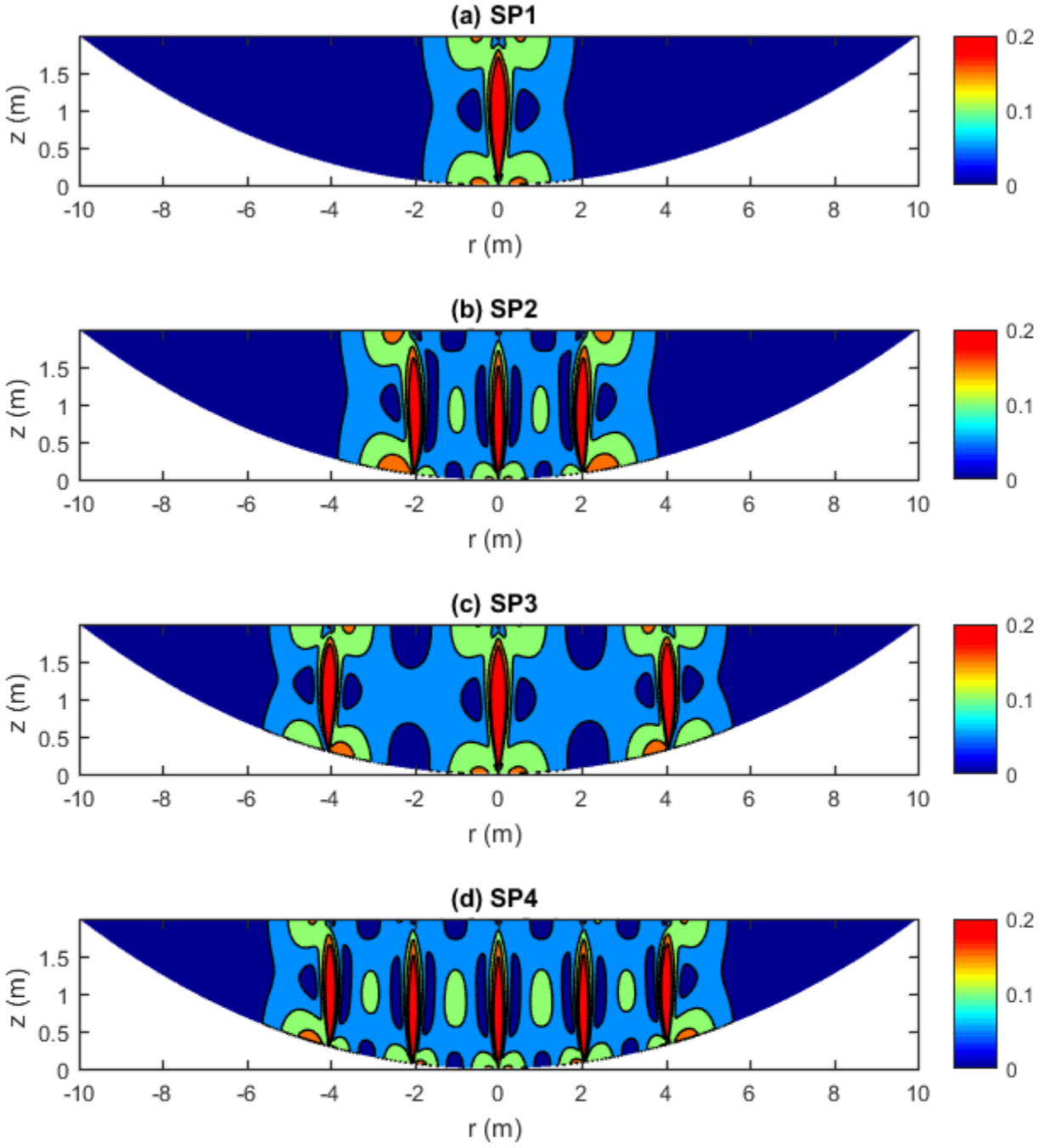

Figure 5.5 Contours of water velocity (in m/s) for four model runs: (a) SP1; (b) SP2; (c) SP3; and (d) SP4 (see Table 5.2).

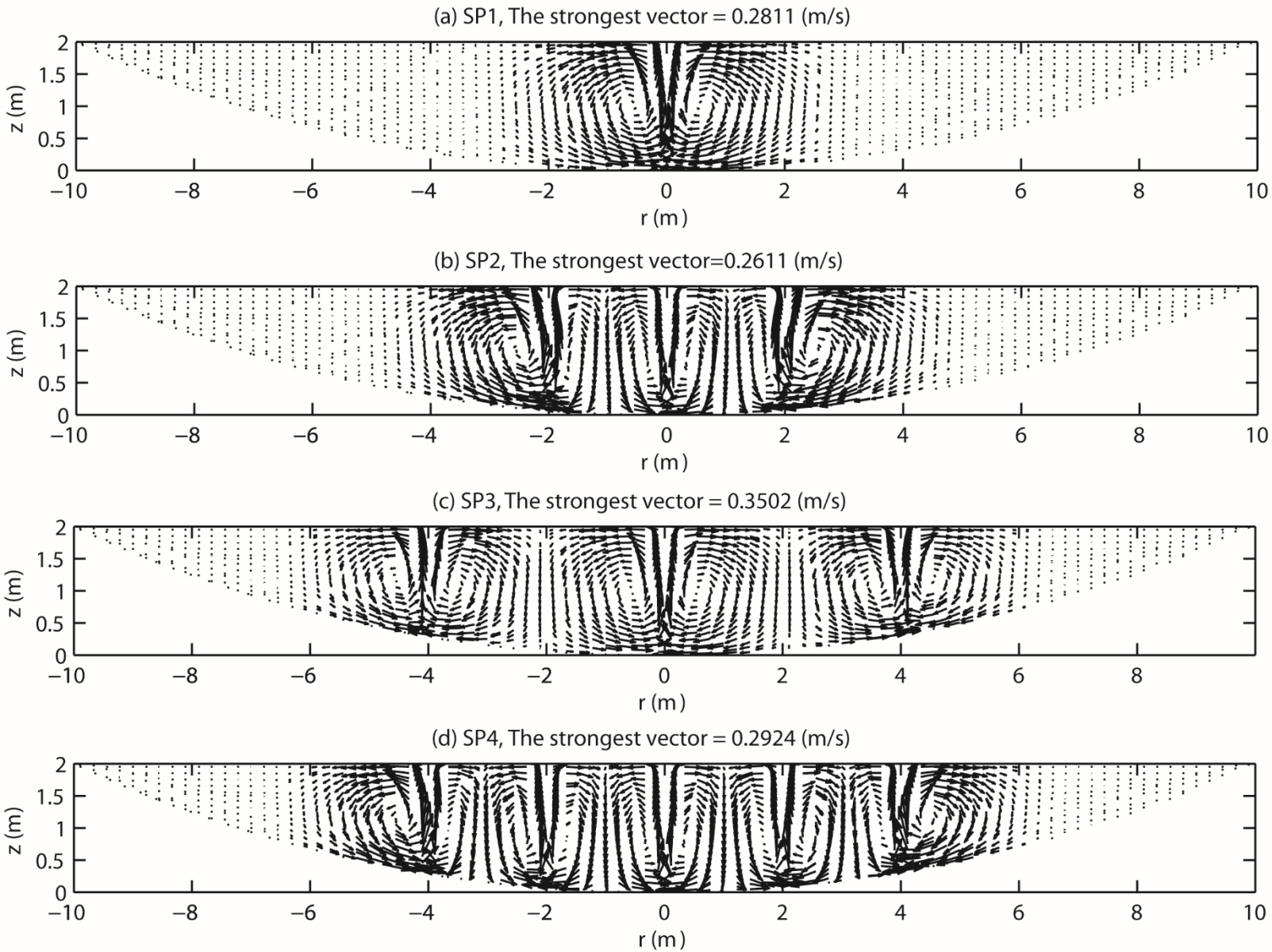

Figure 5.6 Water velocity vectors (in m/s) for four model runs: (a) SP1; (b) SP2; (c) SP3; and (d) SP4 (see Table 5.2).

Velocity vectors of water flow in the lake for runs SP1, SP2, SP3 and SP4 are plotted in Figures 5.6(a)– (d). These streamlines show the magnitude and direction of flow; therefore, they are helpful in visualizing the flow patterns in the lake.

The results for these four runs show two common features: First, aeration causes clockwise eddy motion to the right of the individual injector's centre and counter-clockwise eddy motion to the left. Second, these eddy motions cause circulation of water over the whole water depth. This means that aeration is effective in producing exchange of water masses.

The flow field shown in Figures 5.6(a)-(d) exhibits a number of interesting features:

- A strong jet flow is seen to occur in the centre region above each port as a direct response to the injection of air bubbles.
- The jet flow entrains lake water from both sides of its centre in the lower water column and creates eddy motions on each side. These eddy motions produce diverging flows from the centre above the port in the upper water column. The flow of water converges to compensate the upward motion of water at the centre. This prediction is realistic.
- There are upward and downward motions on both the left side and the right side of the individual injectors in the lake. These conditions would enhance the renewal of bottom water with oxygenated surface water.

All four runs produce motions in the water. However, the radius of influence varies with the number of ports and port spacing. The radius of influence is defined as half the horizontal distance between the distinct outer edges of the two individual eddies on both sides of each port [Figs. 5.6(a)-5.6(d)]. In other words, motions created for runs SP1, SP2, SP3 and SP4 spreads to a radius of 2.5, 4.5, 6, and 6.5 m away from the centre of the lake, respectively. However, due to a larger

port spacing for run SP3 (Table 5.2), there is a region with a velocity smaller than 0.04 m/s between the two plumes for the run.

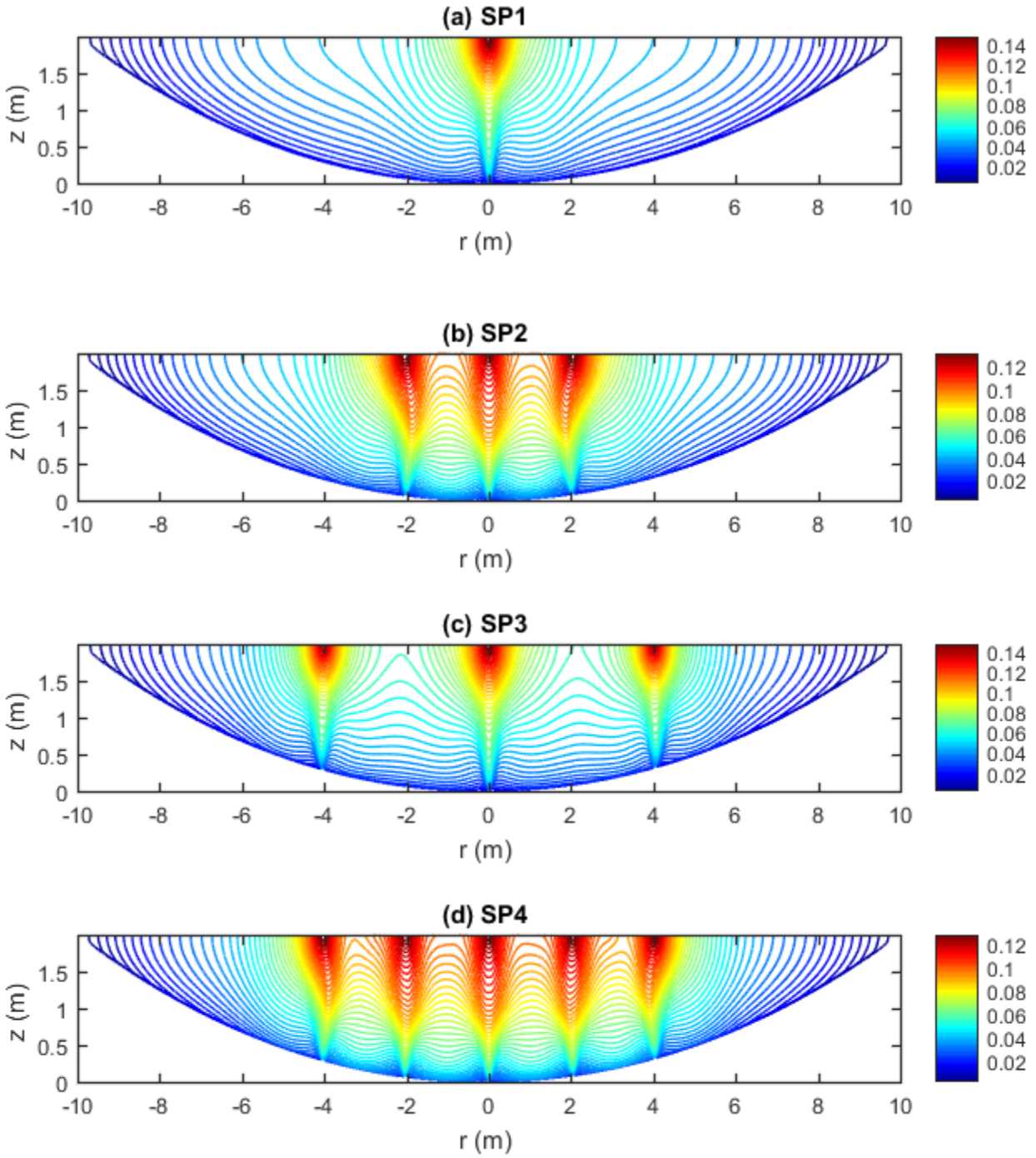

Figure 5.7 Distribution of turbulence kinetic energy (k in J/kg) for four model runs: (a) SP1; (b) SP2; (c) SP3; and (d) SP4 (see Table 5.2).

The distribution of turbulent kinetic energy of water in the lake is illustrated in Figures 5.7 (a)-(d). The turbulent kinetic energy is plotted for four runs SP1, SP2, SP3, and SP4. Bubble plumes promote mixing and improve water quality in the lake. Bubbles work to mix and aerate the lake to prevent anaerobic conditions. Figures 5.7 (a)-(d) depict that the highest kinetic energy is generated inside the bubble plume and in the vicinity of the air-water interface. This confirms that the bubble plume can indeed generate a strong and wide surface flow.

A comparison of water turbulent kinetic energy created by the injection of air bubbles in the lake demonstrates which model run is successful in generating water circulation and mixing in the lake. Comparing run SP1 with SP2 [Figures 5.7 (a) and (b)], shows that employing two additional air bubble injectors results in an overall increase in the mixing rate of the liquid phase. This is observed by the higher values of water velocity and water turbulent kinetic energy in Figures 5.5 (a)-(b) and Figures 5.7 (a)-(b), respectively. However, model run SP2 still produces zones of weak mixing.

Analysing the results of model runs SP2 and SP3, indicates lower speeds between the two adjacent injectors in SP3. In addition, an analysis of turbulent kinetic energy implies the existence of areas with low mixing located between the adjacent injectors in the model lake. Thus the horizontal distance of L=2H or 4 m cannot provide sufficient mixing while run SP2, where L=H or 2 m, provides better mixing in the water between the two adjacent injectors. For run SP2, the turbulent kinetic energy has higher values between the two adjacent injectors, which indicates an optimization of the mixture [Fig. 5.7 (b)]. Lower values of turbulent kinetic energy are observed mainly on the left-hand side and right-hand side of the injectors located on the left-hand side and right-hand side of the lake's centre, respectively. This indicates the existence of areas with weak

mixing in this model run. Therefore, three injectors are not sufficient to provide circulation in the entire lake. Thus, two more injectors were added to the lake for run SP4.

For run SP4 in the area between the five inlets, the water is fully mixed [figures 5.7 (d)]. The turbulent kinetic energy values between the injectors close to the bottom are increased compared to those for run SP2. Thus, between the five injectors there are no dead zones. It can be concluded that run SP4 is sufficient to provide an efficient circulation in the entire lake, except in two small areas close to the shorelines. It is noticed that the stagnation area is reduced compared to the other three runs, meaning that better circulation is attained by run SP4.

Dissolved oxygen concentration in the water for the four runs is depicted in Figure 5.8. The oxygen concentration is calculated using equation (4.9). The oxygen concentration is continuously increased with time for runs SP1, SP2, SP3, and SP4. The values of concentration of oxygen added to water for run SP1 are small and are not sufficient to prevent anoxic condition in the model lake. A comparison of SP2 with SP3 demonstrates that mixing intensification induces the dispersion of air and increases the oxygen transfer rate for model run SP2. The oxygen concentration curve for model run SP4 is plotted above those for runs SP3, SP2, and SP1. In other words, the injection of air bubbles from five inlets appears to generate higher amounts of oxygen in the lake water.

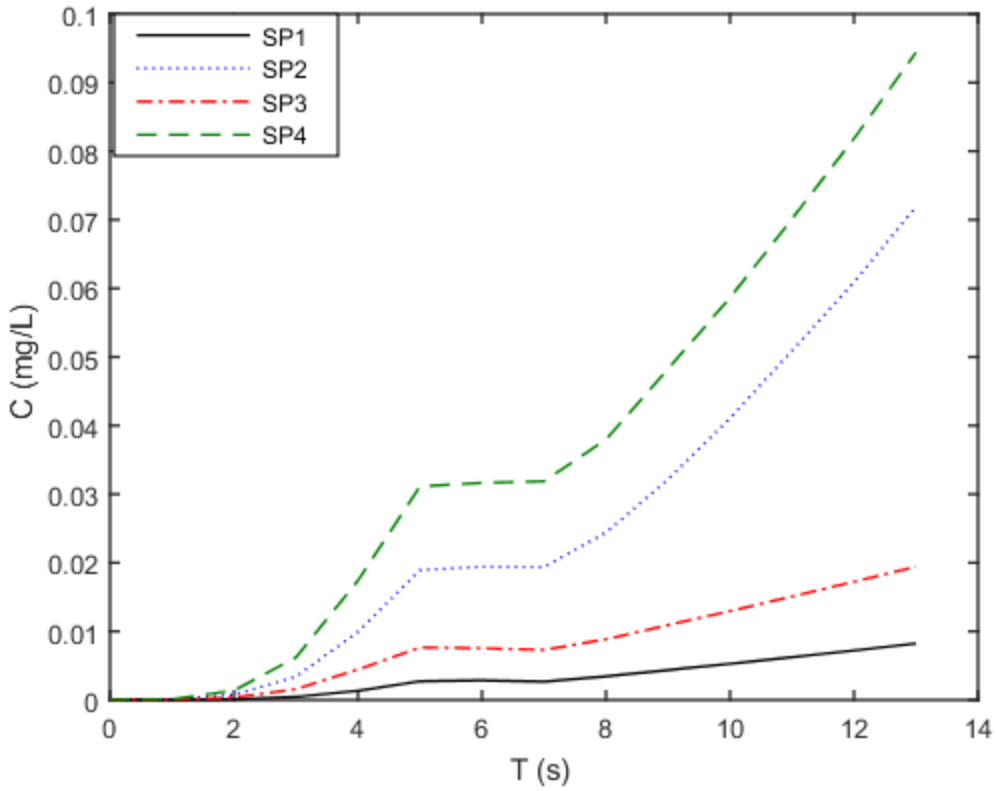

Figure 5.8 Oxygen mass transfer in the model lake for four model runs: (a) SP1; (b) SP2; (c) SP3; and (d) SP4 (see Table 5.2).

5.6 Port elevation above the lake bottom

Bubbles are injected with an initial upward velocity of u_o = 0.085 m/s and diameter of d_b = 3 mm. For five runs EL1,EL2, EL3, EL4, and EL5, all simulation conditions were kept the same, while the height of the inlet (opening of the aerator) varies from 0.05 to 0.5 m. The heights of the opening of the aerator for runs EL1, EL2, EL3, EL4 and EL5, are equal to 0.05, 0.1, 0.2, 0.3 and 0.5 m, respectively. The setup and other conditions used for the five simulations were as follows: The 2D axisymmetric model domain was used; the time step was 0.1 s; the turbulence closure model was the standard k-ε [equations (3.22) and (3.23)]; the bubble size was 3 mm; the initial air velocity

was 0.085 m/s; the mesh resulution varied between 1 and 9 mm with inflation; Schiller-naumann (Schiller and Naumann, 1935) drag force was considered as the only force for the interfacial force. A summary of the model runs is listed in Table 5.3.

For these five runs of $y^+ <1$ for the first node off a wall boundary. At very small y, the velocity profile is linear (White, 1991, p. 415):

$$\tau_w = \frac{\mu u}{y} \quad or \quad u^+ = y^+ \quad for \quad y^+ \leq 5 \tag{5.1}$$

where y^+ is the dimensionless wall distance and u^+ is dimensionless friction velocity; y is the vertical coordinate of the first computational node from the bottom; μ is the dynamic viscosity (kg/ms); τ_w is the bottom shear stress (N/m^2); u is the Reynolds-averaged velocity component parallel to the bottom (m/s). This very thin region near the wall is called the viscous sublayer.

Table 5.3 Summary of port elevation used for model runs.

Model run	EL1	EL2	EL3	EL4	EL5
Port elevation, h_d (m)	0.05	0.1	0.2	0.3	0.5

Aeration-induced water flow can possibly disturb the bottom surface sediments and lead to re-suspension of the sediments in the lake water. Care should be taken to avoid significant re-suspension. The opening of aerators should be installed at a certain height from the bottom. The optimal height will be determined through sensitivity tests. The ideal condition is that air bubbles rise continuously from the bottom to the water surface where they become fully saturated with oxygen, and circulate back to the bottom layer of water. The results will be a thorough mixing of the entire water column, elimination of thermal stratification, and high oxygen level at the sediment-water interface.

The optimal height prediction is feasible by predicting the flow strength at which sediment movement first begins. This condition is usually expressed in terms of a critical shear stress.

Critical shear stress is the shear stress required to mobilize sediments delivered to the water. When the shear stress equals to the critical shear stress ($\tau_w = \tau_c$), the bottom sediments will be liked to be picked up by the flow of water. When shear stress is excessively greater than the critical shear stress, sediment resuspension will be likely to occur. When shear stress is lower than the critical shear stress, sediment settling and aggradation will occur.

This is typically represented by a comparison between a dimensionless bottom shear stress (τ_w^*) and a dimensionless critical shear stress (τ_c^*). The dimensionless shear stress is called the Shields parameter and is defined as (Shields, 1936):

$$\tau_w^* = \frac{\tau_w}{(\rho_s - \rho_w) g D_{50}} \tag{5.2}$$

where ρ_s is the density of the sediment (kg/m^3); ρ_w is the density of the water (kg/m^3); g is the acceleration due to gravity (m/s^2); D_{50} is the reported median grain size of the surface bed material (m).

The distribution of wall shear stresses along the bottom of the lake for the five runs is demonstrated in Figures 5.9 (a)-(e). Shear stress distributions for all five runs have a triangular shape with a steep gradient at thedistance of 0.1 to 0.2 m from the centre of the lake. A maximum value of wall shear stress is observed slightly off the centre. The wall shear stress then progressively decreases to reach value close to zero at the distance of r =3 m from the centre approximately. In other words, shear

stress first increases to the maximum and then decreases rapidly with radial distance and drops to zero at the distance about r = 3 m.

The flow of water converges to compensate the upward motion of water close to the centre for all five runs. The peak shear stress is found at locations off the centre due to strong flow convergence created there. The strength of flow convergence is enhanced by decreasing the port elevation.

For runs with a lower port elevation (EL1 and EL2), the transport of high momentum towards the bottom leads to steeper streamwise velocity gradients there and hence to enhanced shear. The opposite occurs for the runs with higher port elevation, where low momentum fluid is convected away from the wall, thereby reducing streamwise velocity gradients.

Table 5.4 Dimensionless shear stress for five model runs (EL1, EL2, EL3, EL4, and EL5).

Sediment type	Grain size (mm)	d_{50} (mm)	Maximum dimensionless shear stress (-)				
			EL1	EL2	EL3	EL4	EL5
Very fine sand	0.062-0.125	0.12	0.0934	0.0807	0.0297	0.0132	0.0115
Fine sand	0.125-0.250	0.19	0.0590	0.0510	0.0188	0.0083	0.0072
Medium sand	0.250-0.500	0.34	0.0330	0.0285	0.0105	0.0047	0.0041
Coarse sand	0.5-1.0	0.59	0.0190	0.0164	0.0061	0.0027	0.0023
Very coarse sand	1.0-2.0	1.5	0.0075	0.0065	0.0024	0.0011	0.0009
Very fine gravel	2.0-4.0	3	0.0037	0.0032	0.0012	0.0005	0.0005

The values for the dimensionless maximum shear stress for runs EL1, EL2, EL3, EL4, and EL5 are presented in Table 5.4 for four different grain size. A comparison is made between the values listed in Table 5.4 and the dimensionless critical shear stress of 0.023 to 0.0385 as suggested by Parker (1990). The grain size composition in Lake Caron is dominated by fine sand (Appendices A and B). The comparison showed that runs EL1 and EL2 can cause resuspension of the sediment for the first three types of sediments (very fine sand, find sand and medium sand) since the shear stress is larger than the critical shear stress. However, the maximum shear stress for the larger sediment grains (such as coarse sand, very coarse sand and very fine gravel) with runs EL1 and EL2 is smaller than the dimensionless critical shear stress. This means that resuspension of sediments will not occur for coarser sediments with runs EL1 and EL2. Increasing the port height to 0.2 m in run EL3 will reduce the wall shear stress. The shear stress for the very fine sand in run EL3 is very close to and larger than the critical shear stress. Thus, model run EL3 can only resuspend the very fine sands. In run EL4 and EL5, the wall shear stress is smaller than the critial shear stress for all particle sizes. Therefore, an increase in the port height will cause a decrease in the resuspension of sediments to the water. A comparison between τ_w^* and τ_c^* showed that both runs EL4 and EL5 prevent resuspension of the sediments to the water. However, the port elevation for EL4 is smaller than the port elevation for EL5, this means that EL4 can aerate more regions than EL5. Therefore, among these five model runs, EL4 is preferable.

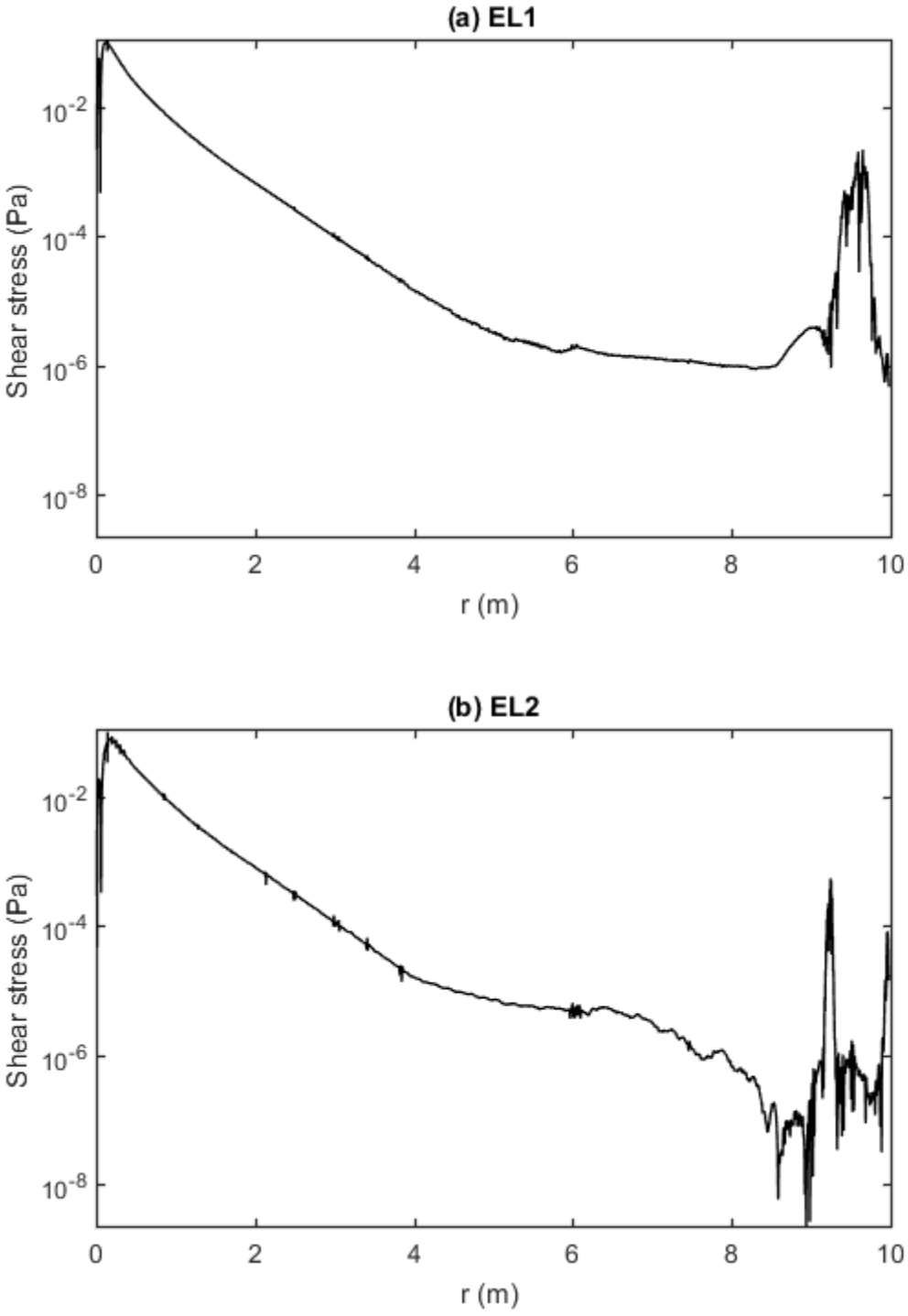

Figure 5.9 Distribution of the bottom shear stress (τ_w in Pa) along the radial distance (r) for five model runs: (a) EL1; (b) EL2; (c) EL3; (b) EL4; and (e) EL5 (see Table 5.3).

Figure 5.9 (Continued).

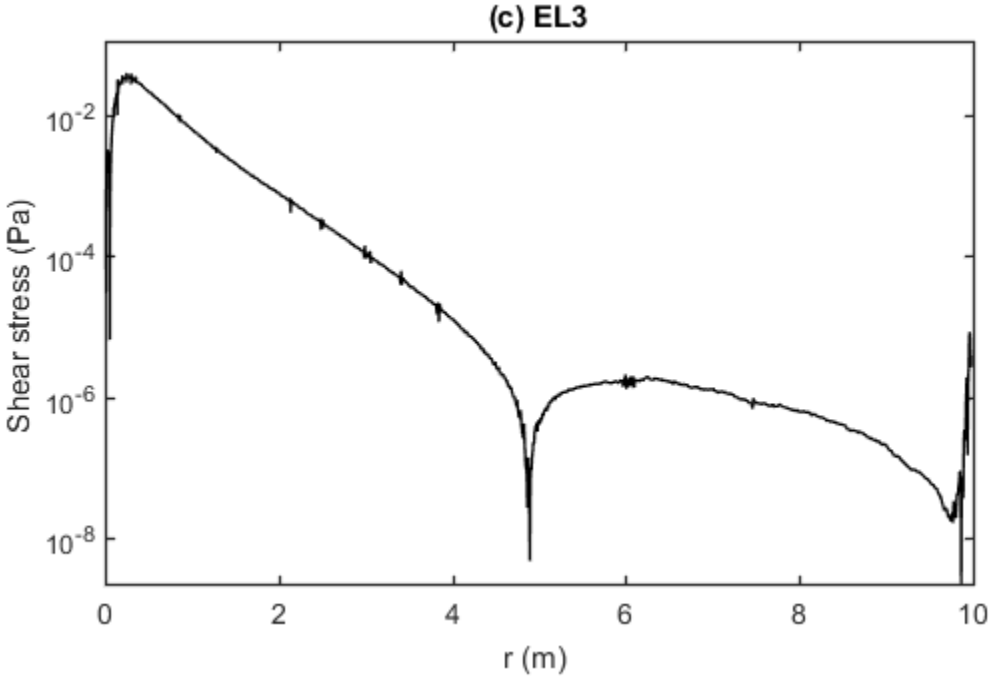

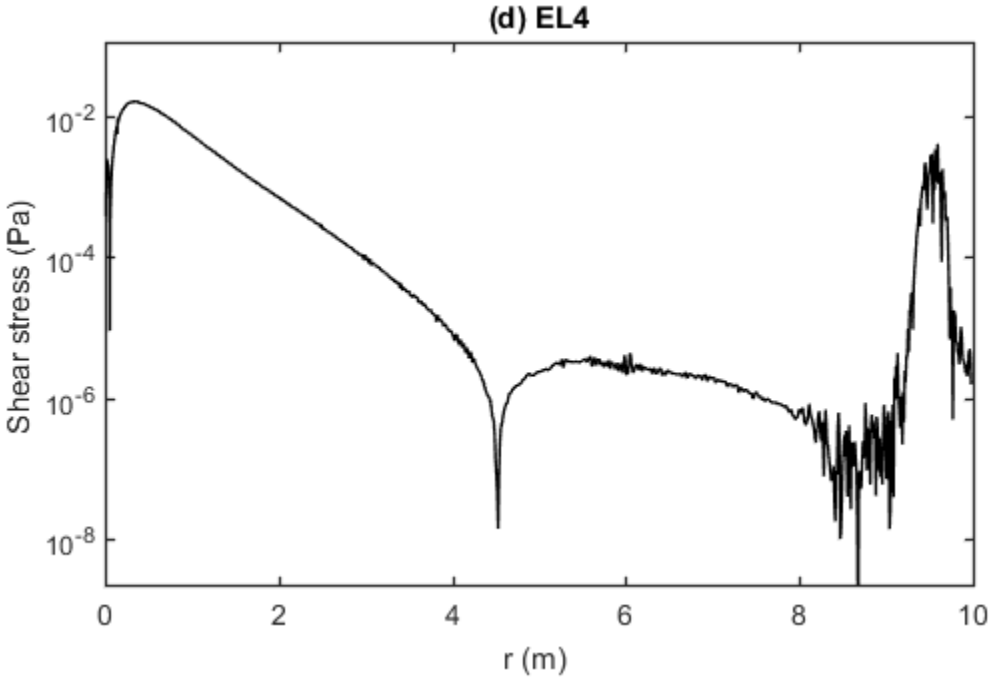

Figure 5.9 (Continued).

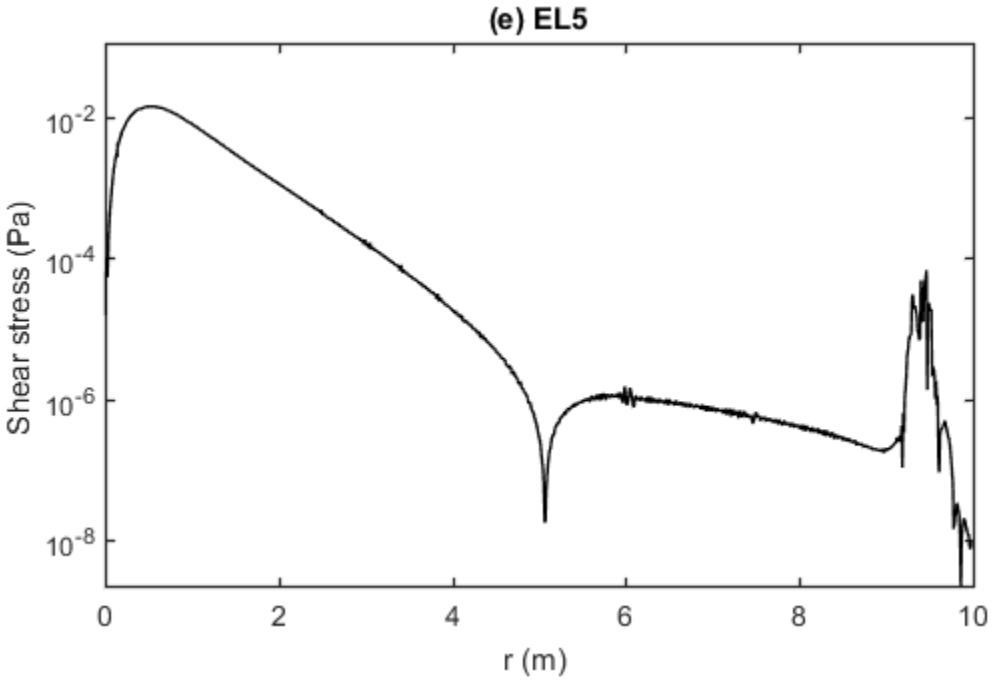

5.7 Bubble aeration of a deep stratified lake

A bubble plume diffuser was applied to Loon Lake to break the stratification. Loon Lake is located in the southern part of the Town of Wayland in the western part of Steuben County in the State of New York, U. S. The lake has a surface area of 141 acre (or 0.5706 km^2) with a maximum depth of 13 m. The stratification in the lake is due to mainly vertical variations in water temperature.

The purpose of this was to apply the computational fluid dynamic model to investigate the feasibility of using bubble plume aerators to reduce stratification in a lake, thus potentially reducing hypoxia. During the summer, as the temperature warms in the lake, the top layer of the lake (epilimnion) gets warmer, while the bottom layer of the lake (hypolimnion) stays very cold [Figure 5.10 (a)]. At the interface between these layers (metalimnion), a thermocline develops

with the temperature changing very rapidly over a very short vertical distance. This thermocline creates a thermal barrier to the mixing of surface and bottom waters because of the different densities. The initial temperature profile had thermal stratification during summer and winter, as shown in Figure 5.10 (a) and Figure 5.10 (b), respectively. The temperature difference between the epilimnion and hypolimnion was approximately 10 º C and 3 º C in summer and winter, respectively.

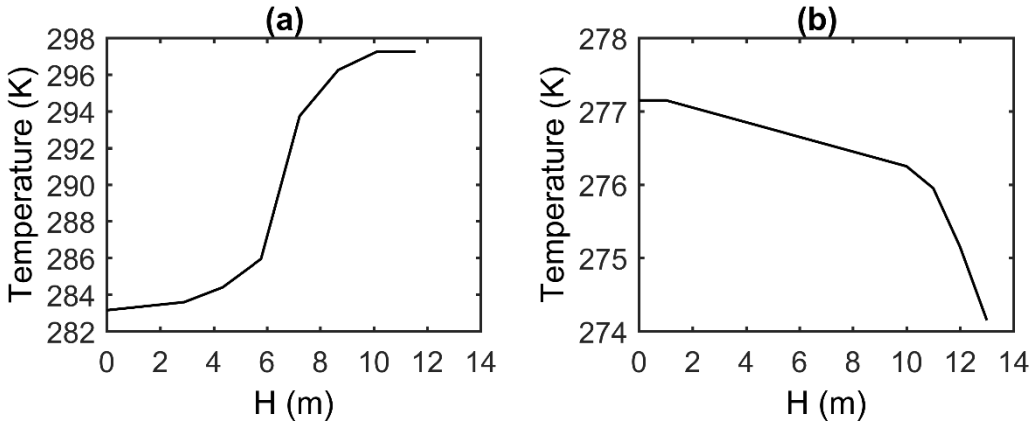

Figure 5.10 Temperature profile of Loon Lake at initial stage (t = 0) before aeration: (a) during the summer; (b) during the winter.

Two simulations were performed to investigate efficiency of aeration in eliminating stratification in a stratified model lake, reflecting the condition of Loon Lake. The Euler–Euler approach with the standard k–ε model was used. The full 2D model domain is a lake with a width of $\overline{AB} = 20\,\text{m}$ at the surface, and a maximum depth of H = 13 m at the lake's centre. A summary of setup for both model runs is given in Table 5.5 .The total simulation time was $t = 450\,s$. This is long enough, as explained below. First, air bubbles entered the domain (Figure 5.1) at an upward velocity of v_o = 0.085 m/s. The model domain had a maximum depth H = 13 m (Figure 5.1). Thus, the air bubbles

entering the domain at the bottom were expected to reach the water surface in 153 s or the advection time scale was 153 s. Therefore, the simulation time period of 450 s is almost three times of the advection time scale. Results are exported at t = 0 s, t = 50 s, t= 75 s, t = 100s, t =150 s, t = 200 s, and t = 450 s.

Table 5.5 Summary of setup for CFD model runs. The two runs use the Eulerian approach. The time step Δt is 0.1 s for both runs.

Run	Season	Turbulence closure	Model domain	Lift force	Turbulent dispersion	Wall lubrication	Turbulence interaction	Top boundary condition
STR1	Summer	Standard k-ε	Full 2D	TM	LDB	Frank	Sato	de-gassing
STR2	Winter	Standard k-ε	Full 2D	TM	LDB	Frank	Sato	de-gassing

5.7.1 Summer de-stratification

Figures 5.11 (a)-(g) illustrate distribution of water temperature in the lake in the summer. The initial temperature distribution before the operation of aeration is depicted in Figure 5.11 (a). It illustrates a thermally stratified lake before air injection. Figures 5.11 (b)-(g) show de-stratification patterns caused by a diffused aeration system. The simulated temperature distribution are plotted at six different times from the beginning of aeration in Figures 5.11 (b)-(g). Figures 5.11 (a)-(g) show that as the bubbles rise from the diffuser, they entrain cold and dense water in the cold hypolimnion layer and form plumes. As the air is released and bubbles rise to the surface, vertical water flows are generated. Near the water surface, the entrained water is detrained and emitted horizontally [Figure 5.11 (b)]. This is due to the fact that the mixture of air-water reaches its natural

buoyancy where its density is equal to the density of the surrounding water (Moshfegi et al., 2005). The now horizontally flowing cold bottom water converges and sinks below the warm, surface water.

Thus, bubble plumes carry the denser hypolimnetic water up to the epilimnion and diverges radially at the water surface. The horizontally flowing cold bottom water converges and sinks below the warm, surface water [Figure 5.11 (c)]. After mixing with the less dense epilimnetic water, it submerges and expands up and down until it mixes the entire lake and breaks the thermal gradient. A comparison of Figures 5.11 (b)-(g) with Figure 5.11 (a) demonstrates that the water temperature difference between the surface and bottom layer is significantly reduced. As the bubbles continue to enter water and mixing continues at the simulation time of $t = 450\ s$, results show that the aeration is effective in breaking down the stratification [Figure 5.11 (g)].

As the bubbles continue to erode the metalimnion and hypolimnion, the rate of erosion increases as the temperature of the epilimnion approaches that of the hypolimnion.

Figures 5.11 (a)-(g) also depict that the bubble aeration system diffuses air from the hypolimnion to the water surface, circulates the whole water body and brings water to the surface so that it can be exposed to oxygen in the atmosphere. Circulation caused by aeration successfully eliminates thermal stratification in the water body. The ensuing circulation decreases surface water temperature from 297 K [Figure 5.11 (a)] to 292 K [Figure 5.11 (e)]. At this flow rate, bubble plumes have enough buoyancy to allow the negatively buoyant hypolimnion water to reach the free surface.

The procedure of aeration by injecting air bubbles will increase the oxygen level in the water. Also, oxygen is gained when surface water is pushed to the lake bottom and bottom water is raised to

the surface [Figure 5.11 (b)-(d)]. This circulation pattern will allow a large amount of oxygen to reach the bottom of the lake when oxygen-poor hypolimnetic water is in contact with the atmosphere.

The summer surface temperature was lowered by continuous mixing. However, the bottom temperatures approached, the surface temperature. This may be beneficial to warm-water fish, but disastrous to cold-water fish. Therefore, in some lakes, hypolimnetic oxygenation is preferable to de-stratification of the whole lake.

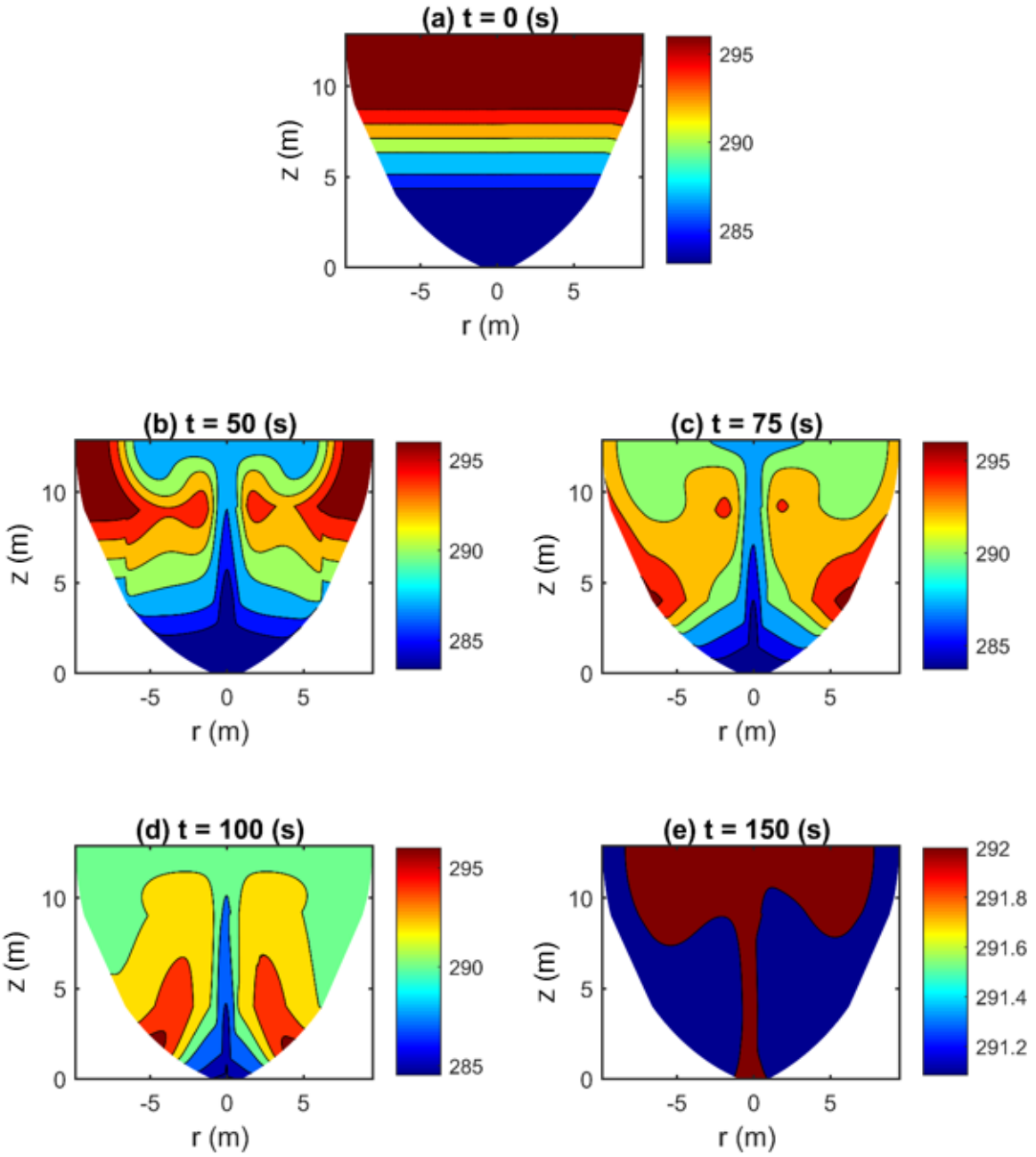

Figure 5.11 Distribution of water temperature and de-stratification patterns caused by a diffused aeration system during the summer: (a) stratified lake; being de-stratified at: (b) $t = 50$ s; (c) $t = 75$ *s*; (d) $t = 100$ *s*; (e) $t = 150$ *s*; (f) $t = 200$ *s*; (g) $t = 450$ *s* after starting the aeration.

Figure 5.11 (Continued).

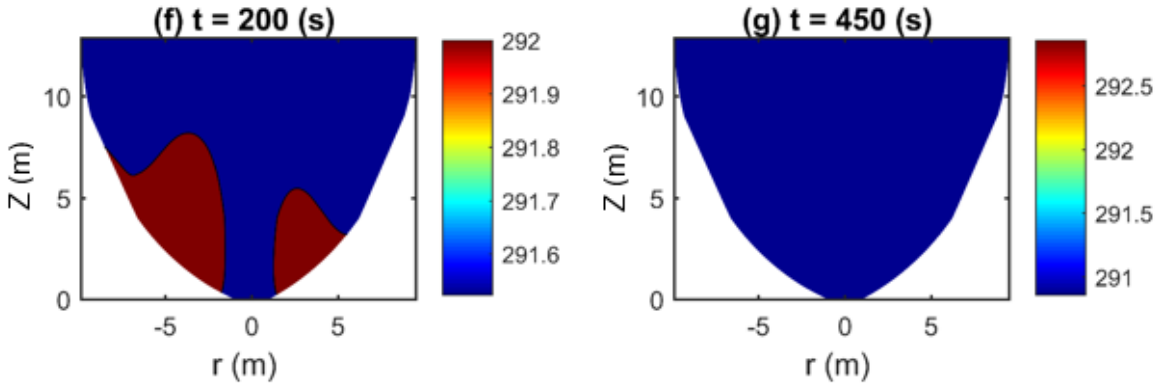

5.7.2 Winter de-stratification

The advent of ice formation in Loon Lake during the winter has caused winter stratification as shown in Figure 5.12 (a). The formation of ice ceased the exchange of oxygen with the atmosphere and caused reduction of dissolved oxygen concentrations with depth.

Figures 5.12 (b)-(h) demonstrate aeration procedures at different times after injecting air bubbles. Figure 5.12 (b) depicts that as the bubbles rise, they disturb the stratified water layers by entraining denser water (the density of water is greatest at T = 277 K) and carrying it towards the surface. Warm bottom water is lifted to the surface and warms the less dense cold water. The surface water approached 277 K [Figure 5.12 (c)].

Near the water surface, denser water is detrained from the plume and diverges radially. The horizontally flowing bottom water converges and sinks back toward the bottom [Figures 5.12(c)-(e)]. The downward vertical flow is perpetuated by density differences. This process is continuously repeated until the density structure of the water column is completely dismantled and water temperature equals to 276 K [Figures 5.12(f)-(h)].

Thus, aeration circulates slightly warmer bottom water to the surface where the heat can melt the ice cover or prevent its formation in the first place. Also, aeration not only adds oxygen to the water directly via the bubbles and agitation, but the open area allows the exchange of oxygen with the atmosphere.

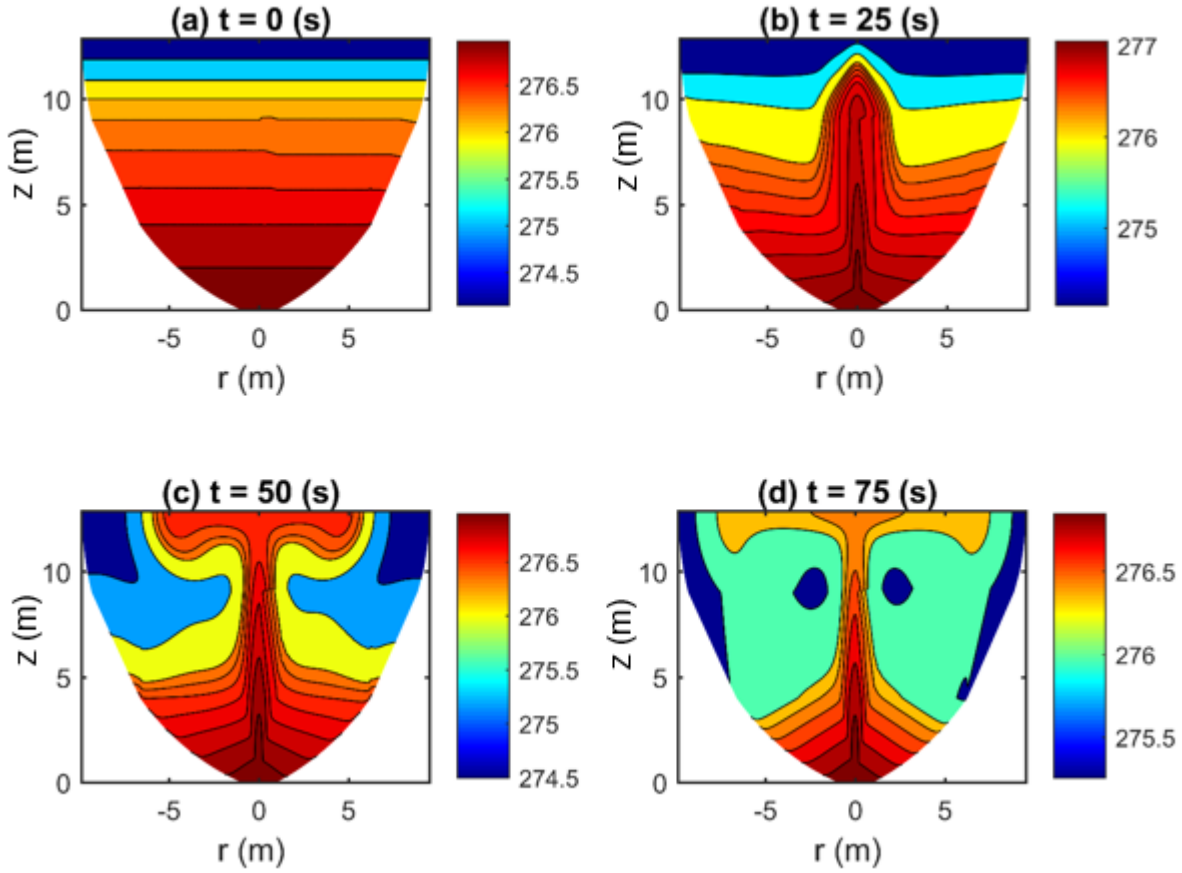

Figure 5.12 Distribution of water temperature and de-stratification patterns caused by a diffused aeration system during the winter: (a) stratified lake; being destratified at: (b) t = 25 s; (c) t= 50 s; (d) t = 75 s; (e) t =100 s; (f) t = 150 s; (g) t = 200 s; (h) t = 450 s after starting the aeration.

Figure 5.12 (continued).

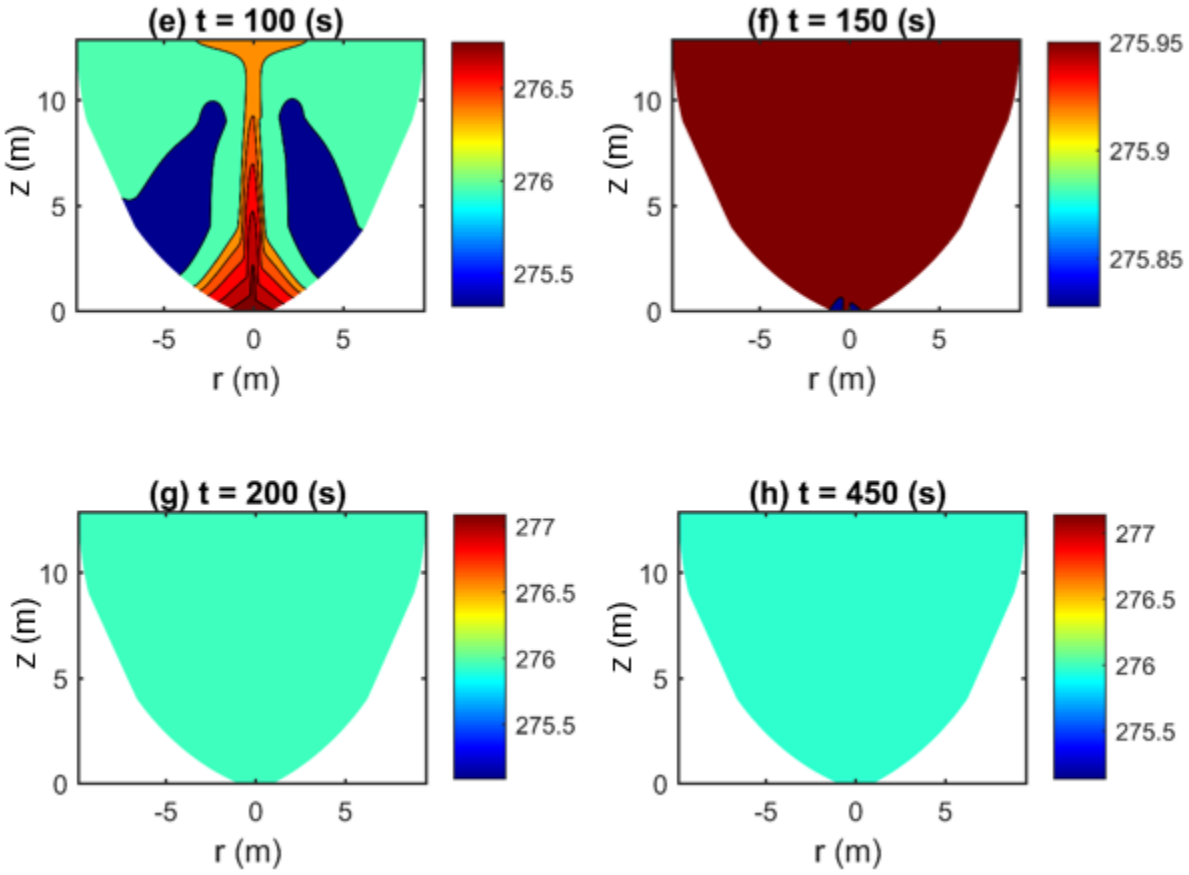

6 Conclusions and Recommendations for Future Work

6.1 Conclusions

There has been very limited numerical studies reported in the literature about aeration effects on lake eutrophication. In this thesis, simulations of bubbly flow in two different types of domains have been performed: (a) cylindrical bubble column; and (b) lakes. Motions of air bubbles moving through the liquid phase (water) are characterized by the use of multiphase models and computational techniques for gas–liquid flows. The numerical simulations presented in this thesis are based on the two-fluid Euler–Euler modelling approach. The Eulerian modelling framework is based on ensemble-averaged mass and momentum transport equations governing each phase (Ishii, 1971). For this particular class of two-phase flows, air bubbles are considered as finite fluid particles of the disperse phase co-flowing with the continuum liquid phase, water. Numerical solutions for two- and three-dimensional air bubble systems in stagnant water are presented in both dimensional and normalised form.

In Chapter Four, the computational domain was a water holding tank of cylindrical shape (Figure 4.1). The laboratory data of Anagbo and Brimacombe (1990) were used to validate the CFD predictions in the chapter. The predictions of air volume fraction, water velocity and air velocity presented in the chapter yielded satisfactory agreement with the experimental results.

The gas fraction profiles are bell-shaped, with the gas fraction decreasing with increasing height above the port and with increasing radial distance from the centerline axis at selected heights. Vertical water velocity profiles are sigmoidal; velocities increase with increasing height above the port but decrease with increasing radial distance at selected heights. The flow reverses from upward to downward at the distance of $r/H = 0.42$ beyond the axis, approximately.

The bubble velocity profiles show that velocities decrease with increasing height above the port and with increasing radial distance. Close to the water surface, the vertical bubble velocities decrease more rapidly as the liquid begins to flow radially outwards from the plume. These findings were consistent with the observations of Anagbo and Brimacombe (1990), for injection through a porous plug.

Steady state simulations have been performed to identify the dynamic and steady state behaviour of a cylindrical bubble column. The results for these simulations were the same as the results for transient simulations at the time of reaching the steady state. Specifically, there are no significant differences of predicted air volume fraction, water velocity, and air velocity between the two types of simulations. The transient simulations produce movement of bubbles in water at different times during the bubble injection process, which cannot be obtained from steady state simulations. The transient simulations allow a comparison of results, after reaching the steady state, with experimental data.

In Chapter Five, the model domains have geometry similar to lakes of different depths (Figure 5.1). The chapter discusses artificial circulation in lakes induced by injecting air bubbles for the control of anoxic condition in lakes and the improvement of lake water quality. The idea was to generate optimal artificial circulations in the lake of interest for the purpose of decreasing the impact of anoxic conditions on water quality.

The following conclusions can be drawn from the numerical results.

(1) A proper solution for bubble columns is crucially dependent on the correct modelling of interphase forces and turbulence models. The effect of interfacial forces has been thoroughly assessed. The predicted radial distributions of three primitive variables (air

volume fraction, air velocity and water velocity) are validated against experimental data of Anagbo and Brimacombe (1990). Comparisons show that the consideration of the effect of interfacial forces has improved the predictions, especially at larger distances from the centreline of the model cylinder. The best agreement is obtained with the use of the Schiller-Nauman (Schiller and Nauman, 1935) model for drag, the Tomiyama (Tomiyama, 1998) model for lift, the Lopez-de-Bertodano (Lopez-de-Bertodano, 1992) model for turbulent dispersion, and Frank (Frank et al., 2004) model for wall lubrication.

(2) The standard k-ε model appears to perform better than the RNG k-ε model and the Realisable k-ε model. With the RNG k-ε model, the percentage errors in water-velocity predictions have a relatively high standard deviation. The SST k-ω model slightly improves air-velocity predictions but not water-velocity predictions, in comparison to those from the standard k-ε model. RSM performs the best among all the turbulence closure models. It is worth noting that relatively speaking, the standard k-ε model is conceptually less complicated and is seen to produce relevant results.

(3) Bubble diffusers/injectors, releasing air bubbles from the bottom of the lake in question, are shown to produce free, turbulent bubble-plumes, rising to the water surface through buoyant forces. Injected air forms bubble plumes. The ascending plumes entrain water, producing vertical circulation and lateral surface spreading. Oxygen transfers to the water across the bubble interfaces as the bubbles rise from the diffuser to the water surface. This is quantified through the calculations of volumetric mass transfer coefficient $K_L a_b$.

(4) Simulation results of the cylindrical bubble column show that circulations are produced by the injection of air bubbles. Also, the ascending plumes widens at an angle of 16.2°as they ascend. This angle does not include the effect of radial flow, which occurs near the water

surface. The predicted angle is close to observations. For example, the laboratory work of Miller and Mackay (2001) showed that the ascending plumes widen at an angle of 12-15°. Olsen and Skjetne (2016) suggested a widening angle of roughly 15°.

(5) The aeration is shown to be effective in producing exchange of water masses and enhancing the renewal of bottom water with oxygenated surface water. Air bubbles rise continuously from the bottom to the water surface where they become fully saturated with oxygen, and circulate back to the bottom layer of water. Thus, oxygen transfer also occurs across the air-water interface as a result of turbulence induced by bubbles motions and water circulations.

(6) The highest turbulent kinetic energy is generated within bubble plumes and in the vicinity of the air-water interface. This confirms that bubble plumes can indeed generate a strong and wide surface flow.

(7) To avoid significant re-suspension of sediments from the lake bottom, the opening of aerators in the lake in question should be mounted at a certain height from the bottom. The optimal height has been determined through sensitivity tests. It is concluded that port elevation of $h_p = 0.3$ m (the total depth at the centre of the lake being $H = 2$ m) will prevent re-suspension of bottom sediments while it creates full circulations around the injector.

(8) Many independent variables have influence on the flow field. The first set of variables are variables related to air injection, including bubble size (d_b), initial velocity (v_o), and air flowrate (q). The second set of variables are diffuser variables, including the number of ports, port diameter or diffusion area (d_p), spacing between adjacent ports, port angle with the horizontal (ϕ), and elevation of ports above the lake bottom.

a. The air bubble diameter is considered as an important parameter in modeling the gas dispersion mechanism in the water body, since it directly affects the gas volume fraction and interfacial area. It determines the bubble rising velocity and the gas residence time, which in turn governs the gas hold-up, the interfacial area and subsequently the gas–liquid mass-transfer rate. Smaller air bubbles would rise slower and remain longer in the water. Also, smaller bubbles have greater contact area, hence the area for the mass transfer. Therefore, a greater proportion of the oxygen in the air bubbles will dissolve in the water.

b. An injector of a larger diameter produces higher turbulent kinetic energy than an injector of a smaller diameter. The former provides higher turbulent kinetic energy due to higher upward and downward water velocity and higher air volume fraction in the model domain.

c. With respect to the number of ports, to produce efficient circulations and vigorous turbulent mixing in the entire lake, multiple ports are required. Employing additional injectors of air bubbles results in an overall increase in the mixing rate of the liquid phase. This has clearly been demonstrated by the higher values of water velocity and water turbulent kinetic energy.

d. The effect of the port spacing is significant in generating motions in water and reducing dead zones. It has been shown that the horizontal distance equal to the maximum depth of the lake ($L = H$ or 2 m) reduces dead zones between two adjacent injectors and produce stronger downward flows. This induces the dispersion of air and increases oxygen transfer rate in water.

(9) The degassing boundary condition is recommended since there is no need to include a freeboard region. This will save computing time. It realistically allows air bubbles to leave the domain, but prevents water from leaving.

(10) The results with 2D axisymmetric domain are in a good agreement with the 3D simulation. Thus, a 2D axisymmetric computational domain is recommended for two reasons: a) it offers high computational efficiency, relative to a 3D domain; and b) it appears to be sufficient to capture measured characteristics of air and water velocities, and air volume fraction.

(11) Simulations of the winter condition of Loon lake (where the maximum depth at the centre of the lake is H = 13m) show that bubble plumes can successfully inhibit the formation of surface ice by bringing bottom water to the surface. It circulates slightly warmer bottom water to the surface where the heat can melt the ice cover or prevent its formation in the first place.

(12) Bubble plumes are shown to be successful in controlling the stratification structure of lakes to improve water quality, enhancing oxygen levels for aquatic growth. De-stratification of lake water can occur by mixing the lower-level water (hypolimnion) with the surface water (epilimnion). Denser water is lifted upward where turbulence generated by the bubbles produces mixing with the less dense water.

6.2 Recommendations for future research

Although the provided analyses and methodologies are quite good and constitute a set of powerful tools to improve water quality in lakes and capture bubble flow characteristics, there are some improvements that can still be made. This section provides some suggestions for future studies.

- The accuracy of the Eulerian-Eulerian approach greatly relies on the empirical constitutive equations used. The Eulerian-Lagrangian model, however, involves a small number of empirical equations and is more suitable for providing detailed information of discrete phases. However, this approach requires longer computing time. The Eulerian-Lagrangian approach may be used in the future when computing power is greatly enhanced.
- In this thesis, the investigation of the effect of port spacing was done in model simulations where the inlets/injectors/diffusers are installed at the bottom of the lake in question. It is recommended to study the effect of port/injector spacing while the opening of the inlet is mounted at a certain elevation from the lake bottom.
- The present research has assumed that the lake in question has an axisymmetric configuration. Real-world lakes rarely have such simple geometry. Typically, real lakes in nature have an unstructured geometry and their depth varies irregularly from one point to another. In order to simulate a real-world lake, future studies should consider more realistic lake geometry and varying depth, and investigate the effect of lake configurations on flow behaviour.
- It would be interesting to investigate the influence of a mixture of air bubbles of different diameters on bubbly flow behaviour. In particular, further development is necessary for bubbly flows of higher gas void fraction, which takes into account bubble breakup and coalescence together with bubbles of different sizes. The present research has been limited to the consideration of bubbles of uniform diameter.

References

Ahlgren, I., Frisk, T. and Nielsen, L.K. (1988). "Empirical and theoretical models of phosphorus loading, retention and concentration vs. lake trophic state." *Journal of Hyrobiologia*, 170, 285-303.

American Public Health Association (APHA). (1975). "Standard Methods for the Examination of Water and Wastewater, 14th Edition".

Anagbo, P.E., and Brimacombe, J.K. (1990). "Plume characteristics and liquid circulation in gas injection through a porous plug." *Metallurgical Transactions B*, 21B, 637-648.

Ansari, A.A., Gill, S.S., Lanza G.R., and Rast W. (2011). "Eutrophication: Causes, Consequences and Control." Springer, New York, pp. 262.

Ansari, A. A., and Khan, F. A. (2009). "Remediation of eutrophied water using Spirodela polyrrhiza L. Shleid in controlled environment." *Pan-American Journal of Aquatic Sciences*, 4(1), 52-54.

ANSYS. (2006). "FLUENT 15.0 user's guide."

ANSYS. (2013). "FLUENT 6.3 user's guide."

Antal, S. P., Lahey, R. T., and Flaherty, J. E. (1991). "Analysis of phase distribution in fully developed laminar bubbly two-phase flow." *International Journal of Multiphase Flow*, 17(5), 635-652.

Azzopardi, B., Zhao, D., Yan, Y., Morvan, H., Mudde, R. F., and Lo, S. (2011). "Hydrodynamics of gas-liquid reactors: normal operation and upset Conditions." John Wiley and Sons, pp. 315.

Barbiero, R.P., Ashby, S.L. and Kennedy R.H. (1996). "The effects of artificial circulation on a small northeastern impoundment." *Water Resources Bulletin, American Water Resources Association*, 32(3): 575-584.

Bernhardt, H. (1967). "Aeration of Wahnbach Reservoir without changing the temperature profile." *Journal of American Water Works Association*, 59(8), 943-964.

Brashier C.K., Churchill L., and Leidahl G. (1973). "Effect of silt removal in a Prairie Lake." USEPA Ecological research, 73(37), pp. 201.

Brown, C. A., and Power, J. H. (2011). "Historic and recent patterns of dissolved oxygen in the Yaquina Estuary (Oregon, USA): Importance of anthropogenic activities and oceanic conditions." *Estuarine, Coastal and Shelf Science*, 92(3), 446-455.

Brucato, A., Grisafi, F., and Montante, G. (1998). "Particle drag coefficients in turbulent fluids." *Chemical Engineering Science*, 53(18), 3295-3314.

Canadian Council of Ministers of the Environment (CCME). (2005). "Phosphorous." *Canadian Water Quality Guidelines.*

Canadian Council of Ministers of the Environment. (2004). "Phosphorus: Canadian guidance framework for the management of freshwater systems".

Chen, C. C., Gong, G. C., and Shiah, F. K. (2007). "Hypoxia in the East China Sea: One of the largest coastal low-oxygen areas in the world." *Marine Environmental Research*, 64(4), 399-408.

Chin, D. A. (2006). "Water-Quality Engineering in Natural Systems." John Wiley and Sons, Hoboken, New Jersey, pp. 610.

Chung, T.J. (2002). "Computational Fluid Dynamics." Cambridge University Press, Cambridge, U.K. pp. 1012.

Cloutier, R.G., and Sanchez, M. (2007)."Trophic status evaluation for 154 lakes in quebec, canada: monitoring and recommendations." *Canadian Journal of Water Quality Research*, 42(4), 252-268.

Cokljat, D., Slack, M., Vasquez, S. A., Bakker, A., and Montante, G. (2006). "Reynolds-stress model for Eulerian multiphase." *Progress in Computational Fluid Dynamics, an International Journal*, 6(1-3), 168-178.

Colin, R.B., and Robert, E.D. (2007). "Do changes in seaweed biodiversity influence associated invertebrate epifauna?."*Journal of Experimental Marine Biology and Ecology*, 344(2), 206–214.

Cook, G.D., Welch, E.B., Petersn, S.A. and Newroth, P.R. (1993). "Restoration and management of lakes and reservoirs." 2nd edition, Lewis Publishers, Boca Raton, FL.

Cooke G.D., Welch E.B, Peterson S.A, and Nicholas S.A. (2005). "Restoration and management of lakes and reservoirs."3rd edition.CRC Press, Boca Raton, FL 33487-2742, pp.591.

Cooke, G.D., and Carlson, R.E. (1989). "Reservoir management for water quality and THM precursor control." American Water Works Association Research Foundation,Denver,Co.

Dai, L., and Pan, G. (2014). "The effects of red soil in removing phosphorus from water column and reducing phosphorus release from sediment in Lake Taihu." *Water Science and Technology*, 69(5), 1052-1058.

DeMoyer C.D., Schierholz E.L., Gulliver J.S., and Wilhelms S.C. (2003). "Impact of bubble and free surface oxygen transfer on diffused aeration systems." *Water Research*, 37(8), 1890-1904.

Díaz, M. E., Iranzo, A., Cuadra, D., Barbero, R., Montes, F. J., and Galán, M. A. (2008). "Numerical simulation of the gas–liquid flow in a laboratory scale bubble column: influence of bubble size distribution and non-drag forces." *Chemical Engineering Journal*, 139(2), 363-379.

Diaz, R. J. (2001). "Overview of hypoxia around the world." *Journal of environmental quality*, 30(2), 275-281.

Diaz, R. J., and Rosenberg, R. (2008). "Spreading dead zones and consequences for marine ecosystems." *Science*, 321(5891), 926-929.

Dixit, S., Verma, N., Tiwari, S. and Mishara, D.D. (2007). "An innovative technique for lake management with reference to aeration unit installed at lower lake, Bhopal, India." *Environmental Monitoring and Assessment*, 124(1-3): 33-37.

Dodds, W.K., Bouska, W.W., Eitzmann, J.L., Pilger, T.J., Pitts, K.L., Riley, A.J., Schloesser, J.T., and Thornbrugh, D.J. (2009). "Eutrophication of U.S. freshwaters: analysis of potential economic damages." *Environmental Science and Technology,* 43(1), 12-19.

Drury D. D., Porcella, D. B. and Gearheart, R. A. (1975). "The effects of artificial destrafication on the water quality and microbial populations in Hyrum Reservoir." *Utah Water Research Laboratory*, Utah State University, Logan, Utah, PREJEW011-11.

Ellis, C. R., Stefan, H. G., and Gu, R. (1991). "Water temperature dynamics and heat transfer beneath the ice cover of a lake." *Limnology and oceanography*, 36(2), 324-334.

Environment Canada. (2004). "Canadian guidance framework for the management of phosphorus in freshwater systems." *Ecosystem Health: Science-based Solutions,* 1-8, 1-114.

Fast, A. W. (1968). "Artificial destratification of el capitan reservoir by aeration. Part I: effects on chemical and physical parameters" Fish bulletin, 141, California State Department of Fish and Game, Sacramento, CA.

Fast, A. W., and Lorenzen, M. W. (1976). "Synoptic survey of hypolimnetic aeration." *Journal of the Environmental Engineering Division*, 102(6), 1161-1173.

Ferreira, A., Cardoso, P., Teixeira, J. A., and Rocha, F. (2013). "pH influence on oxygen mass transfer coefficient in a bubble column. Individual characterization of k_L and a." *Chemical Engineering Science*, 100, 145-152.

Fischer, H. B., List, J. E., Koh, C. R., Imberger, J., & Brooks, N. H. (1979). "*Mixing in inland and coastal waters*." Elsevier.

Frank, T., Shi, J., and Burns, A. D. (2004). "Validation of Eulerian multiphase flow models for nuclear safety application." In *Proceeding of the Third International Symposium on Two-Phase Modelling and Experimentation,* Pisa, Italy.

Frank, T., Zwart, P. J., Krepper, E., Prasser, H. M., and Lucas, D. (2008). "Validation of CFD models for mono-and polydisperse air–water two-phase flows in pipes." *Nuclear Engineering and Design*, 238(3), 647-659.

Gachter, R. (1976). "Die tiefnwasserableitung, ein weg zur sanierung von seen."*Schweiz Z.Hydrol*. 38(1), 1-28.

Gafsi, M. and Kettab A. (2012). "Treatment of water supplies by the technique of dynamic aeration." *Journal of Procedia Engineering*, 33: 209–214.

Gao, X., Kong, B., Ramezani, M., Olsen, M. G., and Vigil, R. D. (2015). "An adaptive model for gas–liquid mass transfer in a Taylor vortex reactor." *International Journal of Heat and Mass Transfer*, 91, 433-445.

Garcia-Ochoa, F., and Gomez, E. (2004). "Theoretical prediction of gas–liquid mass transfer coefficient, specific area and hold-up in sparged stirred tanks."*Chemical Engineering Science*, 59(12), 2489-2501.

Garrison P.J., and Ihm, D.M. (1991). "Final annual report of long term evaluation of Wisconsin Clean Lake projects: Part B: lake assessment. "Wisconsin Department of Natural Resources, Madison.

Gawronska, H., Brzozowska, R., Grochowska, J., and Lossow, K. (2003). "Possibilities to reduce internal loading to lake water by artificial aeration." *Journal of Environmental Studies*, 12(2), 171-179.

Gibbons, H.L., and Funk, W.H. (1983). "A few pacific Northwest examples of short-term lake restoration successes and potential problems with some techniques." *Lake Restoration and Management*, Second Annual Conference NALMS. USEPA-440/5-83-001.

Gray, J. S. (1992). "Eutrophication in the sea." In Proceedings of the 25th European Marine Biology Symposium (Colombo, G. C., Ferrari, I., Ceccherelli, V. U. and Rossi, R, eds), Olsen and Olsen, Fredensborg, pp. 3-13.

Gulliver, J. S. (2007). “Introduction to chemical transport in the environment.” Cambridge University Press, New York, pp.288.

Hamilton, S. K., Sippel, S. J., Calheiros, D. F., and Melack, J. M. (1997). “An anoxic event and other biogeochemical effects of the Pantanal wetland on the Paraguay River.” *Limnology and Oceanography*, 42(2), 257-272.

Hanson, D., and Austin, D. (2012). “Multiyear destratification study of an urban, temperate climate, eutrophic lake.” *Lake and Reservoir Management*, 28(2), 107–119.

Hinze, J.O. (1975) “Turbulence”, 2nd edition, McGraw-Hill Publishing Co., New York, pp. 586.

Hjarne, J., Chernoray, V., Larsson, J., and Löfdahl, L. (2007). “Numerical validations of secondary flows and loss development downstream of a highly loaded low pressure turbine outlet guide vane cascade.” In *ASME Turbo Expo 2007: Power for Land, Sea, and Air*. American Society of Mechanical Engineers, 723-733.

Huang, Q., Yang, C., Yu, G., and Mao, Z. S. (2010). “CFD simulation of hydrodynamics and mass transfer in an internal airlift loop reactor using a steady two-fluid model.” *Chemical Engineering Science*, 65(20), 5527-5536.

Huang, W., Wu, C., and Xia, W. (2009). “Oxygen transfer in high-speed surface aeration tank for wastewater treatment: Full-scale test and numerical modeling.” *Journal of Environmental Engineering*, *ASCE*, 135(8), 684-691.

Imteaz, M. A., and Asaeda T. (2000). “Artificial mixing of lake water by bubble plume and effects of bubbling operations on algal bloom.” *Water Research*, 34(6), 1919-1929.

Iriarte, A., Villate, F., Uriarte, I., Alberdi, L., and Intxausti, L. (2015). “Dissolved oxygen in a temperate estuary: the influence of hydro-climatic factors and eutrophication at seasonal and inter-annual time scales.” *Estuaries and Coasts*, 38(3), 1000-1015.

Jakobsen, H. A., Sannes, B. H., Grevskott, S., and Svendsen, H. F. (1997). “Modeling of vertical bubble-driven flows.” *Industrial and Engineering Chemistry Research*, 36(10), 4052-4074.

James, R. T., and Pollman, C. D. (2011). "Sediment and nutrient management solutions to improve the water quality of Lake Okeechobee." *Lake and Reservoir Management*, 27(1), 28-40.

Jensen, J.P., Pedesen, A.R., Jappensen, E. and Sondergaard, M. (2006). "An empirical model describing the seasonal dynamics of phsphorus in 16 shallow eutrophic lakes after external loading reduction." *Journal of American Society of Limnology and Oceanography*, 51(1, part 2): 791-800.

Johnson, G. P., Hornewer, N. J., Robertson, D. M., Olson, D. T., and Gioja, J. (2000). "Methodology, data collection, and data analysis for determination of water-mixing patterns induced by aerators and mixers (No. 2000-4101)." US Dept. of the Interior, US Geological Survey; Branch of Information Services [distributor].

Jurascik, M., Blažej, M., Annus, J., and Markos, J. (2006). "Experimental measurements of volumetric mass transfer coefficient by the dynamic pressure-step method in internal loop airlift reactors of different scale." *Chemical Engineering Journal*, 125(2), 81-87.

Kadic, E., and Heindel, T. J. (2014). "An introduction to bioreactor hydrodynamics and gas-liquid mass transfer." John Wiley and Sons, pp. 314.

Kangura, M., Puuseppa, L., Buhvestovab, O., Haldnab, M., and Kangurb, K. (2013). "Spatio-temporal variability of surface sediment phosphorus fractions and water phosphorus concentration in Lake Peipsi (Estonia/Russia)." *Estonian Journal of Earth Sciences*, 62 (3), 171-180.

Kassim, M. A., Said, M. M., Noor, N. M., Johari, M. A., Ruhani, R., Kamaruddin, A. L.,and Bakar, A. A. (1997). "Preliminary studies on effectiveness of artificial aeration in reducing iron and manganese levels in a tropical reservoir." In *Proc., IAWQ-IWSA Joint Specialist Conf. on an Integrated System of Reservoir Management and Water Supply, Prague, Czech Republic* (pp. 123-130).

Khopkar, A. R., and Ranade, V. V. (2006). "CFD simulation of gas–liquid stirred vessel: VC, S33, and L33 flow regimes." *AIChE Journal*, 52(5), 1654-1672.

Kim S.H., Kim J.Y., Park H., and Park N.S. (2010). "Effects of bubble size and diffusing area on destrafication efficiency in bubble plumes of two-layer stratification." *ASCE Journal of Hydraulic Engineering*, 136 (2), 106-115.

Klapper, H. (1980). "Experience with lakes and reservoir restoration techniques in the German DEnocratic Republic." *Hydrobiologia*, 72(1-2), 31-41.

Knoppert, P. L., Rook, J. J., Hofker, T., and Oskam, G. (1970). "Destratification experiments in Rotterdam." *Journal of American Water Works Association*, 62, 448-454.Madura, K.K., Goldyn, R. (2009). "The internal loading of phosphorus from the sediments of Swarzędzkie Lake (Western Poland)." *Journal of Environmental Study*, 18(4), 635-643.

Kortmann, R.W., Davis, E.R., Frink, C.R., and Henry, D.D. (1983). "Hypolimnetic withdrawal: restoration of Lake Wonoscopomuc, Connecticut." In Lake Restoration Protection and Management, EPA-440/5-83-001, 46-55.

Krishna, R., and Van Baten, J. M. (2003). "Mass transfer in bubble columns." *Catalysis Today*, 79, 67-75.

Kulkarni, A. A. (2008). "Lift force on bubbles in a bubble column reactor: experimental analysis." *Chemical Engineering Science*, 63(6), 1710-1723.

Lane, G. L., Schwarz, M. P., and Evans, G. M. (2005). "Numerical modelling of gas–liquid flow in stirred tanks." *Chemical Engineering Science*, 60(8), 2203-2214.

Launder, B. E., and Spalding, D. B. (1974). "The numerical computation of turbulent flows." *Computer Methods in Applied Mechanics and Engineering*, 3(2), 269-289.

Lee, A.J, and Lee, F. G. (2005). "Eutrophication (Excessive Fertilization), Water Encyclopedia: Surface and Agricultural Water." Wiley, Hoboken, NJ.

Levich V. G. (1962). "Physicochemical Hydrodynamics." Prentice-Hall, Inc, Englewood Cliffs, N. J. pp. 700.

Lima Neto, I. E. (2012). Bubble plume modelling with new functional relationships. *Journal of Hydraulic Research*, 50(1), 134-137.

Lopez de Bertodano, M.A. (1992). "Turbulent bubbly two-phase flow in a triangular duct", Ph.D

Dissertation, Rensselaer Polytechnic Institute.

Macdonald, R. H., Lawrence, G. A., and Murphy, T. P. (2004). "Operation and evaluation of hypolimnetic withdrawal in a shallow eutrophic lake." *Lake and Reservoir Management*, *20*(1), 39-53.

Madura, K.K, and Gołdyn, R. (2009). "The internal loading of phosphorus from the sediments of Swarzędzkie Lake (Western Poland)." *Polish Journal of Environmental Studies*, 18(4), 635-643.

Malueg, K. W., Tilstra, J. R., Schults, D. W., and Powers, C. F. (1973). "Effect of induced aeration on stratification and eutrophication processes in an Oregon farm pond. *Man-Made Lakes: Their Problems and Environmental Effects*, 578-587.

Marchisio, D.L., and Fox, R.O. (2007). "Multiphase reacting flows: modelling and simulation." Springer, 492.

Marsden, M. W. (1989). "Lake restoration by reducing external phosphorus loading: the influence of sediment phosphorus release." *Freshwater Biology*, 21(2), 139-162.

Matsui, S., Ide, S. and Ando, M. (1955). "Lake reservoirs: reflecting waters of sustainable use."*Water Science and Technology*, 32(7), 221-224.

McCord, S. A., Schladow, S. G., and Miller, T. G. (2000). "Modeling artificial aeration kinetics in ice-covered lakes." *Journal of Environmental Engineering*, 126(1), 21-31.

McGinnis, D. F., Lorke, A., Wüest, A., Stöckli, A., and Little, J. C. (2004). "Interaction between a bubble plume and the near field in a stratified lake." *Water Resources Research*, 40(10).

McWhirter, J. R., and Hutter, J. C. (1989). "Improved oxygen mass transfer modeling for diffused/subsurface aeration systems." *AIChE Journal*, 35(9), 1527-1534.

Menter, F. R. (2011). “Turbulence modeling for engineering flows.” *Technical Paper, ANSYS inc*, 1-25.

Menter, F. R. (1994). “Two-equation eddy-viscosity turbulence models for engineering applications.” *AIAA journal*, *32*(8), 1598-1605.

Miller, Theron G., W. C. Mackay, and David T. Walty. (2001). "Under ice water movements induced by mechanical surface aeration and air injection." *Lake and Reservoir Management*, 17(4), 263-287.

Moore, T. S., Nuzzio, D. B., Di Toro, D. M., and Luther, G. W. (2009). “Oxygen dynamics in a well mixed estuary, the lower Delaware Bay, USA.” *Marine Chemistry*, 117(1), 11-20.

Mudde, R. F., and Simonin, O. (1999). “Two-and three-dimensional simulations of a bubble plume using a two-fluid model.” *Chemical Engineering Science*, 54(21), 5061-5069.

Mukherjee, B., Nivedita, M., and Mukherjee, D. (2010). “Plankton diversity and dynamics in a polluted eutrophic lake, ranchi.” *Journal of Environmental Biology*, 31(5), 827-839.

Mulligan, C.N., Fukue, M., and Sato, Y. (2010). “Sediments contamination and sustainable remediation.” CRC, Taylor and Francis, Boca Raton, FL 33487-2742.

Nürnberg, G. K., Hartley, R., and Davis, E. (1987). “Hypolimnetic withdrawal in two North American lakes with anoxic phosphorus release from the sediment.” *Water research*, 21(8), 923-928.

Nürnberg, G.K., Molot, L.A., O’Connor, E., Jarjanazi, H., Winter, J.G., and Young, J.D. (2013). “Evidence for internal phosphorus loading, hypoxia and effects on phytoplankton in partially polymictic Lake Simcoe, Ontario.” *Journal of Great Lakes Research*. 39(2), 259-270.

Olsen, J. E., and Skjetne, P. (2016). “Current understanding of subsea gas release: A review.” *Canadian Journal of Chemical Engineering*, 94, 209-219.

Ozkundakci, D., Hamilton, D.P., McDowell, R., and Hill, S. (2014). "Phosphorus dynamics in sediments of a eutrophic lake derived from p nuclear magnetic resonance spectroscopy" *Marine and Freshwater Research*, 65, 70-80.

Pan, Y., Dudukovic, M. P., and Chang, M. (2000). "Numerical investigation of gas-driven flow in 2-D bubble columns." *AIChE Journal*, 46(3), 434-449.

Penn, M. R., Auer, M. T., Doerr, S. M., Driscoll, C. T., Brooks, C. M., and Effler, S. W. (2000). "Seasonality in phosphorus release rates from the sediments of a hypereutrophic lake under a matrix of pH and redox conditions." *Canadian Journal Fisheries Aquatic Sciences,* 57(5), 1033-104.

Peterson S.A. (1981). "Sediment removal as a lake restoration technique."USEPA-600/3-81-013.

Pettersson, K. (1998). "Mechanisms for internal loading of phosphorus in lakes" *Journal of Hydrobiologia*, 373/374, 21–25.

Phillips, G., A. Bramwell, J. Pitt, J. Stansfield, and M. Perrow. (1999). "Practical Application of 25 Years' Research into the Management of Shallow Lakes". *Hydrobiologia*, 395/396, 61-76.

Potamis, G.C., Papineau, M., Smeltzer, E., and Mimeault, M. (2004). "International Missisquoi Bay task force" *Final report to the International Joint Commission, October 20, 2004. International Joint Commission, Ottawa, Canada, and Washington, DC.*

Prepas, E. E., and Burke, J. M. (1997). "Effects of hypolimnetic oxygenation on water quality in Amisk Lake, Alberta, a deep, eutrophic lake with high internal phosphorus loading rates." *Canadian Journal of Fisheries and Aquatic Sciences*, 54(9), 2111-2120.

Priskin, J. (2008). "Implications of Eutrophication for Lake Tourism in Quebec".Teoros, 27(2), 59-61.

Qunhe, W., Renduo, Z., Shan, H., and Hengjun, Z. (2008). "Effects of bacteria on nitrogen and phosphorus release from river sediment." *Journal of Environmental Sciences*, 20, 404-412.

Rabalais, N. N., Turner, R. E., and Wiseman, W. J. (2001). "Hypoxia in the Gulf of Mexico." *Journal of Environmental Quality*, 30(2), 320-329.

Ranade V.V. (2002). "Computational flow modeling for chemical reactor engineering." Vol.5, Academic Press, St. Louis, MO, USA.

Reddy, K.R., Q'connor, G.A and Schelske, C.L. (1999). "Phosphorus Biogeochemistry of Subtropical Ecosystems." 1 edition, CRC Press, Boca Raton, FL. pp.101.

Reitzel, K., Hansen, J., Andersen, F., Hansen, K., and Jensen, H.(2005). "Lake restoration by dosing aluminum relative to mobile phosphorus in the sediment." *Environmental Science and Technology*, 39(11), 4134–4140.

Rensen J., Roig V. (2001). "Experimental study of the unsteady structure of a confined bubble plume." *International Journal of Multiphase Flow*, 27(8), 1431-1449.

Richardson, K., and Jorgensen, B. B. (1996). "Eutrophication: definition, history and effects." *Eutrophication in Coastal Marine Ecosystems*, 1-19.

Roghair, I., Sint Annaland, V. M. M., and Kuipers, J. A. M. (2009). "Drag force on bubbles in bubble swarms." *Seventh International Conference on CFD in the Minerals and Process Industries*, CSIRO, Melbourne, Australia.

Robinson, E. L., Irwin, W. H., and Symons, J. M. (1969). "Influence of artificial destratification on plankton populations in impoundments." *Ky Acad Sci Trans*.

Ryding S.O., and Rast W. (1989). "The control of eutrophication of lakes and reservoirs."UNESCO,Paris ; Carnforth, Lancs, U.K. ; Park Ridge, N.J., U.S.A. : Parthenon Pub. Group, pp. 314.

Ryding, S. O. (1982). "Lake Trehörningen restoration project. Changes in water quality after sediment dredging." *Journal of Hydrobiologia,* In *Sediment/Freshwater Interaction*, Springer Netherlands, 92, 549-558.

Sahoo G.B., and Luketina D. (2003). "Modeling of bubble plume design and oxygen transfer for reservoir restoration." *Water Research*, 37(2), 393-401

Sahoo, G. B., and Luketina, D. (2006). "Response of a tropical reservoir to bubbler destratification." *Journal of Environmental Engineering*, *132*(7), 736-746.

Sato K., and Sato T. (2001). "A study on bubble plume behavior in stratified water." *Journal of Marine Science and Technology*, 6(2), 59-69.

Sato, Y., and Sekoguchi, K. (1975). "Liquid velocity distribution in two-phase bubble flow." *International Journal of Multiphase Flow*, *2*(1), 79-95.

Schallenberg, M. and Burns C.W. (2004). "The Waipori/Waihola Lake-Wetland Complex: Summary of research programme (1997-2003) and recommendations." Limnology Report No. 10, Department of Zoology, University of Otago.

Schauser, I., and Chorus, I. (2007). "Assessment of internal and external lake restoration measures for two Berlin lakes" *Lake and Reservoir Management*, 23(4), 366-376.

Schierholz, E. L., Gulliver, J. S., Wilhelms, S. C., and Henneman, H. E. (2006). "Gas transfer from air diffusers." *Water Research*, 40(5), 1018-1026.

Schiller L., and Naumann Z. (1935) "A drag coefficient correlation" Z. Ver. Deutsch. Ing. 77-318.

Schladow, S.G. (1993). "Lake destratification by bubble plume systems: A design methodology." *Journal of the Hydraulics Engineering Div., ASCE*, 119(3), 350-368.

Schuler, M., Zehnder, F., Weigand, B., von Wolfersdorf, J., and Neumann, S. O. (2011). "The effect of turning vanes on pressure loss and heat transfer of a ribbed rectangular two-pass internal cooling channel." *ASME Journal of Turbomachinery*, 133 (2), 021017-01-10.

Shaikh, I.R., Shaikh, P.R., Shaikh, R.A. and Shaikh, A.A. (2013). "Investigation on eutrophication of taroda nala at nanded (india) through physico-chemical analyses of water and composition of planktonic community within the aquatic ecosystem." *International Research Journal of Environment Sciences*, 2(6), 39-48.

Sharpley, A.N., Chapra, S.C., Wedepohl, R., Sims, J.T., Daniel, T.C., and Reddy, K.R. (1994). "Managing agricultural phosphorus for protecting of surface waters: issues and options." *Journal of Environmental Quality*, 23(3), 437-451.

Shields, A. (1936), Anwendung der Aehnlichkeitsmechanik und der Turbulenzforschung auf die Geschiebebewegung, Mitt. Preuss. Versuchsanst. Wasserbau Schiffbau, 26, pp 36.

Shih, T. H., Liou, W. W., Shabbir, A., Yang, Z., and Zhu, J. (1995). "A new k-ϵ eddy viscosity model for high reynolds number turbulent flows." *Computers and Fluids*, 24(3), 227-238.

Simonin, O., and Viollet, P. L. (1990). "Predictions of an oxygen droplet pulverization in a compressible subsonic coflowing hydrogen flow." *Numerical Methods for Multiphase Flows*, FED91, 65-82.

Snodgrass, W.J. (1987). "Analysis of models and measurements for sediment oxygen demand in Lake Erie." *Journal of Great Lakes Research*, 13(4):738–756.

Sondergaard, M., Jensen, J.P. and Jappesen, E. (2003). "Role of sediment and internal loading of phosphorus in shallow lakes." *Hydrobiologia,* 506(1-3), 135-145.

Steinman, A.D., and M.E. Ogdahl. (2012). "Macroinvertebrate response and internal phosphorus loading in a Michigan lake following alum treatment." *Journal of Environmental Quality* 41(5), 1540-1248.

Suh, S.W., Kim, J.H., Hwang, I.T. and Lee, H.K. (2004). "Water Quality Simulation on an Artificial Estuarine Lake Shiwhaho, Korea." *Journal of Marine Systems*, 45(3), 143-158.

Tomasko, D., Keenan, E. and Curtis. S. (2013). "Managing Water Quality in Huntsman Lake (Virginia, USA)-Development and Implementation of Restoration strategies." *Journal of Environmental Science and Engineering. A*, *2*(6A), pp. 337.

Tomiyama, A. (1998). "Struggle with computational bubble dynamics." *Multiphase Science and Technology*, 10(4), 369-405.

U.S. EPA. (1990). "The lake and reservoir restoration guidance manual." 2nd edition, EPA-440/4-90-006. United States Environmental Protection Agency, Office of Water, Washington, DC, 5-88.

Van Der Molen, D.T. and Boers, P.C.M. (1999). "Eutrophication control in the Netherlands." *Hydrobiologia*, In *the Ecological Bases for Lake and Reservoir Management*, Springer Netherlands. 136, 403-409.

Wang X., Naji H., and Mezrhab A. (2008). "Computational investigation of different models when predicting airflow in an enclosure." *ASME 2008 Pressure Vessels and Piping Division Conference*, 4,179-188.

Wei et al. (2013). "Numerical Simulation of the Three-Component Force Coefficient of a Bridge Section." *Journal of Highway and Transportation Research and Development*, 7(2), 46-49.

Welch, E. B., Michaud, J. P., and Perkins, M. A. (1982). "Alum control of internal phosphorus loading in a shallow lake." JAWRA *Journal of the American Water Resources Association*, 18(6), 929-936.

Welch, E.B. and G.D. Cooke. (1999). "Effectiveness and longevity of phosphorus inactivation with alum." *Lake and Reservoir Mangement*. 15(1), 5-27.

Wetzel, R.G. (2001). "Limnology: Lake and River Ecosystems", 3rd Edition, Academic Press, San Diego, CA 92101, USA, pp. 1006.

With, J. S., and D.I. Wright. (1984). "Lake restoration by biomanipulation: Round Lake, Minnesota, the First Two Years." *Freshwater Biology*, 14(4), 371-383.

Wilcox, D. C. (2006). "Turbulence Modeling for CFD." 3rd edition, DCW Industries, Inc., La Canada, CA, pp. 515.

Wongsuchoto, P., Charinpanitkul, T., and Pavasant, P. (2003). "Bubble size distribution and gas–liquid mass transfer in airlift contactors." *Chemical Engineering Journal*, 92(1), 81-90.

Wu, R. S., Zhou, B. S., Randall, D. J., Woo, N. Y., and Lam, P. K. (2003). "Aquatic hypoxia is an endocrine disruptor and impairs fish reproduction." *Environmental Science and Technology*, 37(6), 1137-1141.

Yakhot, V., Orszag, S. A., Thangam, S., Gatski, T. B., and Speziale, C. G. (1992). "Development of turbulence models for shear flows by a double expansion technique." *Physics of Fluids A: Fluid Dynamics (1989-1993)*, 4(7), 1510-1520.

Yang, S. L., Tiew, K. N., & Char, C. T. (1993). "Artificial destratification through aeration in Upper Peirce Reservoir—its effects on water quality and chemical costs in treatment." *Public Utility Board R&D J*, *5*, 32-49.

Yeoh, G.H. and Tu, J., (2009). "Computational techniques for multiphase flows." Elsevier, Oxford, UK. pp. 643.

Yuan W., and Liu S. (2010). "Three-dimensional numerical modeling of two-phase flow in water-filling pipelines." *ASCE Water Distribution Systems Analysis*, 12-15:122-136.

Yum K., Kim S.H., and Park H. (2008). "Effects of plume spacing and flowrate on destrafication efficiency of air diffusers." *Water Research*, 42(13), 3249-3262.

Yum, K., Ahn, J., Park, H. and Ko, H. (2005). "Two-phase computational fluid dynamics assessment of bubble plume in air-diffuser destratification." *Environmental Technology*, 26 (9): 1043-1054.

Zic, K., Stefan, H.G. and Ellis, C. (1992). "Laboratory study of water destratification by a bubble plume." *Journal of Hydraulic Research*, 30(1), 7-27.

Appendices

A. Laser scattering particle size distribution at Station 1

2015.10.27 15:41:28

HORIBA Laser Scattering Particle Size Distribution Analyzer LA-950

Sample Name	: Lac Caron Sed	Median Size	: 126.44438(μm)
ID#	: 201510271539039	Mean Size	: 248.03333(μm)
Data Name	: 201510271539039	Variance	: 71628(μm²)
Transmittance(R)	: 93.2(%)	Std.Dev.	: 267.6340(μm)
Transmittance(B)	: 93.7(%)	Mode Size	: 809.2311(μm)
Circulation Speed	: 5	Span	: OFF
Agitation Speed	: 3	Geo.Mean Size	: 131.1305(μm)
Ultra Sonic	: OFF	Geo.Variance	: 1.8644(μm²)
Form of Distribution	: Manual	Skewness	: 1.2590
Distribution Base	: Volume	Kurtosis	: 3.2574
Material	: sediment	Diameter on Cumulative %	: (1)5.000 (%)- 16.9310(μm)
Source	: Stn 1-1		: (9)90.00 (%)- 748.2104(μm)
Sample Number	: 1		
Test or Assay. Number	: 1		
Refractive Index (R)	: Lake sediment[Quartz(1.450 - 0.000i),Water(1.333)]		
Refractive Index (B)	: Lake sediment[Quartz(1.450 - 0.000i),Water(1.333)]		

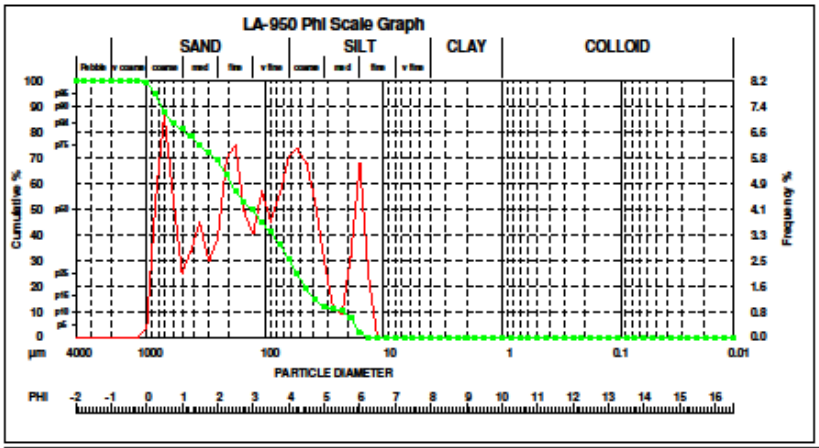

	Diameter	PHI	MILS	Microns	Frequency	Frequency	CUMULATIVE
V PEBBLE	5	-2.00	157.48	4000.00	0.00	0.00	100.00
	6	-1.75	138.42	3360.59	0.00		100.00
	7	-1.50	111.36	2828.43	0.00		100.00
	8	-1.25	93.64	2378.41	0.00		100.00
FINE PEBBLE	10	-1.00	78.74	2000.00	0.00	0.00	100.00
	12	-0.75	66.21	1681.79	0.00		100.00
	14	-0.50	55.68	1414.21	0.00		100.00
	16	-0.25	46.82	1189.21	0.00		100.00
V CRS SAND	18	0.00	39.37	1000.00	0.27	0.27	99.73
	20	0.25	33.11	840.90	4.46		95.27
	25	0.50	27.94	707.11	7.25		88.02
	30	0.75	23.41	594.60	4.56		83.47
CRS SAND	35	1.00	19.69	500.00	2.08	19.34	81.39
	40	1.25	16.55	420.45	2.79		78.60
	45	1.50	13.92	353.55	3.74		74.86
	50	1.75	11.70	297.30	2.48		72.38
MED SAND	60	2.00	9.84	250.00	3.14	12.16	69.23
	70	2.25	8.28	210.22	5.17		63.46
	80	2.50	6.96	176.78	6.25		57.22
	100	2.75	5.85	148.65	4.09		53.13
FINE SAND	120	3.00	4.92	125.00	3.38	19.48	49.75
	140	3.25	4.14	105.11	4.76		44.99
	170	3.50	3.48	88.39	3.76		41.23
	200	3.75	2.93	74.33	4.62		36.61
V FINE SAND	230	4.00	2.46	62.50	5.82	18.96	30.79
	270	4.25	2.07	52.56	6.13		24.66
	325	4.50	1.74	44.19	5.68		18.98
	400	4.75	1.46	37.16	4.38		14.60
CRS SILT	450	5.00	1.23	31.25	2.51	19.71	12.08
	500	5.25	1.03	26.29	1.00		11.09
	625	5.50	0.87	22.10	0.74		10.35
		5.75	0.73	18.59	2.62		7.72
MED SILT		6.00	0.62	15.63	5.68	10.04	2.05
		6.25	0.52	13.14	2.05		0.00
		6.50	0.43	11.05	0.00		0.00
		6.75	0.37	9.29	0.00		0.00
FINE SILT		7.00	0.31	7.81	0.00	2.05	0.00
		7.25	0.26	6.57	0.00		0.00
		7.50	0.22	5.52	0.00		0.00
		7.75	0.18	4.65	0.00		0.00

	Diameter	PHI	MILS	Microns	Frequency	Frequency	CUMULATIVE
V FINE SILT	8.00		0.13	3.28	0.00	0.00	0.00
	8.25		0.13	3.28	0.00		0.00
	8.50		0.11	2.76	0.00		0.00
	8.75		0.09	2.32	0.00		0.00
	9.00		0.08	1.95	0.00		0.00
	9.25		0.06	1.64	0.00		0.00
	9.50		0.05	1.38	0.00		0.00
	9.75		0.05	1.16	0.00		0.00
CLAY	10.00		0.04	0.98	0.00	0.00	0.00
	10.25		0.03	0.82	0.00		0.00
	10.50		0.03	0.69	0.00		0.00
	10.75		0.02	0.58	0.00		0.00
	11.00		0.02	0.49	0.00		0.00
	11.25		0.02	0.41	0.00		0.00
	11.50		0.01	0.35	0.00		0.00
	11.75		0.01	0.29	0.00		0.00
	12.00		0.01	0.24	0.00		0.00
	12.25		0.01	0.21	0.00		0.00
	12.50		0.01	0.17	0.00		0.00
	12.75		0.01	0.15	0.00		0.00
	13.00		0.00	0.12	0.00		0.00
	13.25		0.00	0.10	0.00		0.00
	13.50		0.00	0.09	0.00		0.00
	13.75		0.00	0.07	0.00		0.00
	14.00		0.00	0.06	0.00		0.00
	14.25		0.00	0.05	0.00		0.00
	14.50		0.00	0.04	0.00		0.00
	14.75		0.00	0.04	0.00		0.00
	15.00		0.00	0.03	0.00		0.00
	15.25		0.00	0.03	0.00		0.00
	15.50		0.00	0.02	0.00		0.00
	15.75		0.00	0.02	0.00		0.00
	16.00		0.00	0.02	0.00		0.00
	16.25		0.00	0.01	0.00		0.00
COLLOID	16.50		0.00	0.01	0.00	0.00	0.00

1/1

B. Laser scattering particle size distribution at Station 16

2015.10.27 15:22:00

HORIBA Laser Scattering Particle Size Distribution Analyzer LA-950

Sample Name	: Lac Caron Sed	Median Size	: 201.80527(µm)
ID#	: 20151027 1518035	Mean Size	: 296.67999(µm)
Data Name	: 20151027 1518035	Variance	: 74486(µm²)
Transmittance(R)	: 94.4(%)	Std.Dev.	: 272.9221(µm)
Transmittance(B)	: 95.2(%)	Mode Size	: 215.1540(µm)
Circulation Speed	: 5	Span	: OFF
Agitation Speed	: 3	Geo.Mean Size	: 177.1324(µm)
Ultra Sonic	: OFF	Geo.Variance	: 1.7192(µm²)
Form of Distribution	: Manual	Skewness	: 1.0427
Distribution Base	: Volume	Kurtosis	: 3.0042
Material	: sediment	Diameter on Cumulative %	: (1)5.000 (%)- 19.3932(µm)
Source	: Stn 1-1		: (9)90.00 (%)- 751.1306(µm)
Sample Number	: 1		
Test or Assay. Number	: 1		
Refractive Index (R)	: Lake sediment[Quartz(1.450 - 0.000i),Water(1.333)]		
Refractive Index (B)	: Lake sediment[Quartz(1.450 - 0.000i),Water(1.333)]		

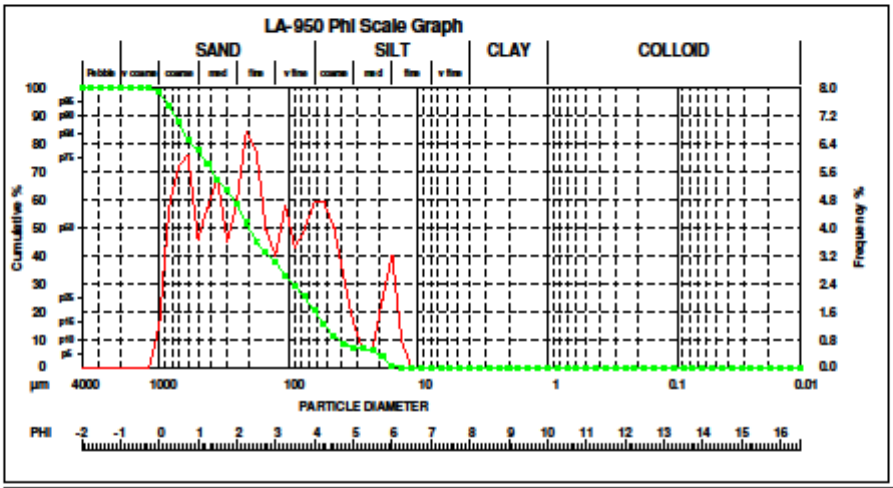

	Diameter	PHI	MILS	Microns	Diameter Frequency	Diameter Frequency	CUMULATIVE
F PEBBLE	5	-2.00	157.48	4000.00	0.00	0.00	100.00
	6	-1.75	129.42	3363.59	0.00		100.00
	7	-1.50	111.36	2828.43	0.00		100.00
	8	-1.25	93.64	2378.41	0.00		100.00
FINE PEBBLE	10	-1.00	78.74	2000.00	0.00	0.00	100.00
	12	-0.75	66.21	1681.79	0.00		100.00
	14	-0.50	55.68	1414.21	0.00		100.00
	16	-0.25	46.82	1189.21	0.00		100.00
V CRS SAND	18	0.00	39.37	1000.00	1.24	1.24	98.76
	20	0.25	33.11	840.90	4.76		94.01
	25	0.50	27.84	707.11	5.99		88.02
	30	0.75	23.41	594.60	6.32		81.70
CRS SAND	35	1.00	19.69	500.00	3.79	20.85	77.91
	40	1.25	16.55	420.45	4.78		73.13
	45	1.50	13.92	353.55	5.65		67.48
	50	1.75	11.70	297.30	3.76		63.72
MED SAND	60	2.00	9.84	250.00	4.90	19.09	58.82
	70	2.25	8.28	210.22	7.05		51.77
	80	2.50	6.96	176.79	6.45		45.32
	100	2.75	5.85	148.65	4.12		41.20
FINE SAND	120	3.00	4.92	125.00	3.25	20.98	37.94
	140	3.25	4.14	105.11	4.65		33.30
	170	3.50	3.48	88.39	3.85		29.44
	200	3.75	2.92	74.33	4.09		25.35
V FINE SAND	230	4.00	2.46	62.50	4.94	17.43	20.41
	270	4.25	2.07	52.56	4.92		15.48
	325	4.50	1.74	44.19	4.17		11.32
	400	4.75	1.46	37.16	2.74		8.58
CRS SILT	450	5.00	1.23	31.25	1.34	13.17	7.24
	500	5.25	1.05	26.39	0.82		6.41
	635	5.50	0.87	22.10	0.64		6.18
		5.75	0.73	18.59	2.02		4.15
MED SILT		6.00	0.62	15.63	3.34	6.42	0.82
		6.25	0.52	13.14	0.82		0.00
		6.50	0.43	11.05	0.00		0.00
		6.75	0.37	9.29	0.00		0.00
FINE SILT		7.00	0.31	7.81	0.00	0.82	0.00
		7.25	0.26	6.57	0.00		0.00
		7.50	0.22	5.52	0.00		0.00
		7.75	0.18	4.65	0.00		0.00

	Diameter	PHI	MILS	Microns	Diameter Frequency	Diameter Frequency	CUMULATIVE
V FINE SILT	8.00		0.15	3.91	0.00	0.00	0.00
	8.25		0.13	3.28	0.00		0.00
	8.50		0.11	2.76	0.00		0.00
	8.75		0.09	2.32	0.00		0.00
	9.00		0.08	1.95	0.00		0.00
	9.25		0.06	1.64	0.00		0.00
	9.50		0.05	1.38	0.00		0.00
	9.75		0.05	1.16	0.00		0.00
CLAY	10.00		0.04	0.98	0.00	0.00	0.00
	10.25		0.03	0.82	0.00		0.00
	10.50		0.03	0.69	0.00		0.00
	10.75		0.02	0.58	0.00		0.00
	11.00		0.02	0.49	0.00		0.00
	11.25		0.02	0.41	0.00		0.00
	11.50		0.01	0.35	0.00		0.00
	11.75		0.01	0.29	0.00		0.00
	12.00		0.01	0.24	0.00		0.00
	12.25		0.01	0.21	0.00		0.00
	12.50		0.01	0.17	0.00		0.00
	12.75		0.01	0.15	0.00		0.00
	13.00		0.00	0.12	0.00		0.00
	13.25		0.00	0.10	0.00		0.00
	13.50		0.00	0.09	0.00		0.00
	13.75		0.00	0.07	0.00		0.00
	14.00		0.00	0.06	0.00		0.00
	14.25		0.00	0.05	0.00		0.00
	14.50		0.00	0.04	0.00		0.00
	14.75		0.00	0.04	0.00		0.00
	15.00		0.00	0.03	0.00		0.00
	15.25		0.00	0.03	0.00		0.00
	15.50		0.00	0.02	0.00		0.00
	15.75		0.00	0.02	0.00		0.00
	16.00		0.00	0.02	0.00		0.00
	16.25		0.00	0.01	0.00		0.00
COLLOID	16.50		0.00	0.01	0.00	0.00	0.00

1/1